INVESTIGATION AND MODELING OF THE MECHANISMS INVOLVED IN BATCH COOLING CRYSTALLIZATION AND POLYMORPHISM THROUGH EFFICIENT USE OF THE FBRM

A Thesis
Presented to
The Academic Faculty

by

Stéphanie C. Barthe

In Partial Fulfillment
of the Requirements for the Degree
Doctor of Philosophy
in the School of Chemical and Biomolecular Engineering

Georgia Institute of Technology
August 2008

INVESTIGATION AND MODELING OF THE MECHANISMS INVOLVED IN BATCH COOLING CRYSTALLIZATION AND POLYMORPHISM THROUGH EFFICIENT USE OF THE FBRM

Approved by:

Dr. Ronald W. Rousseau, Advisor
School of Chemical and Biomolecular Engineering
Georgia Institute of Technology

Dr. Athanassios Nenes
School of Chemical and Biomolecular Engineering
Georgia Institute of Technology

Dr. Martha Grover Gallivan, co-Advisor
School of Chemical and Biomolecular Engineering
Georgia Institute of Technology

Dr. Hamid Garmestani
School of Material and Science Engineering
Georgia Institute of Technology

Dr. Matthew Realff
School of Chemical and Biomolecular Engineering
Georgia Institute of Technology

Date Approved: May 31st 2008

ACKNOWLEDGEMENTS

I first would like to acknowledge the importance of the funds provided through the Silas that allowed the completion of this research. I wish also to give my sincere thanks to my thesis advisor, Dr Ronald W. Rousseau, and my co-advisor, Dr Martha Grover Gallivan, for their knowledge, their helpful advices and time they offered throughout this project. I am grateful to the committee members for all the useful suggestions and remarks made: Dr Athanassios Nenes, Dr. Matthew Realff and Dr. Hamid Garmestani.

I also want to thank past and present members of this research group for their precious help, friendship and support: Karsten Bartling, Jose Mendez del Rio, Cosmas Bayuadri, PJ Dumont, Laurent Nassif, Krystle Chavez, Quinta Nwanosike and Apichit Svang-Ariyaskul.

I give my thanks to all the professors and staff I met at Georgia Tech for being so willingly helpful and sharing part of their knowledge with me.

And last but not least, I would like to express my thankfulness to all my friends and my family for their kindness and support. They shaped the person I am today, without their guidance and support I would not be here.

TABLE OF CONTENTS

LIST OF TABLES

LIST OF FIGURES

NOMENCLATURE

$A_{c,tot}$	Surface area of the crystals
$\boldsymbol{A}$	Symmetric matrix
$\overline{A}_{i,\text{one crystal}}$	Surface area of one crystal of size $\overline{L}_i$
a_0, b_0, c_0	Lengths of the unit cell
a	Parameter
a_i	edge of the octahedral crystal
$\boldsymbol{b}$	Vector
B_p	Particle birth function
c_n	n^{th} coefficient
C	Concentration
C^*	Concentration at saturation
ΔC	Supersaturation
C_s	Concentration of solute in the solid phase
D_i	Diameter of the impeller
D_p	Particle death function
e_{max}	Maximum estimation error on $\boldsymbol{n}_1$
g	Order of the growth kinetic
G	Growth rate
j_n	Number of moments
k_g	Growth kinetic coefficient
k	Boltzman constant (1.38×10^{-23}J.K^{-1})
$\boldsymbol{k}$	Number of chord length in bin $[s_{i-1},s_i]$ (histogram)

k_s	Shape coefficient
k_a	Surface shape factor
k_b	Nucleation kinetic constant
L	Characteristic crystal length
$\overline{L}$	Mean crystal length
$l_n^{(\lambda)}$	nth order Laguerre polynomial
M	Molar mass
$\boldsymbol{M}$	Rotation matrix
m	Number of eigenvectors
m'	Number of vector defining the unobservable subspace
$m_{c,crystallized}$	Mass of the crystals in the slurry
$m_{c,initial}$	Mass of the crystals introduced in the slurry
$m_{solute\ in\ solution}$	Mass of the crystals dissolved in solution
$M_{solvent}$	Mass of the solvent
$\overline{m}_{i,one\,crystal}$	Mass of a crystal of size $\overline{L}_i$
m_j	j^{th} moment of the distribution
ΔN	Number size population density
N_b	Number of bins (N_b = 90)
N_{Re}	Reynolds number
$N_{s,i}$	Speed of impeller
n	Normalized population density, volume weighted
$\boldsymbol{n}_{1,est}$	Estimated length-weighted population density
$\boldsymbol{n}_{1,obs}$	Projection of $\boldsymbol{n}_1$ onto the observable subspace
$\boldsymbol{n}_{1,unobs}$	Projection of $\boldsymbol{n}_1$ onto the unobservable subspace
$n(t_i,L_j)$	Normalized population density a time t_i and for L_j

n_1	Normalized population density, length weighted
n^0	Nuclei density
n_k	Population density for the k^{th} stream
N_A	Avogadro's number
N_b	Number of bins ($N_b = 90$)
N_s	Total number of chord counts
N_T	Total number of crystals
q_p	Normalized single particle chord length density for a crystal of size L
q	Normalized chord length density
$\boldsymbol{q}_{est}$	Estimated chord-length density
$\boldsymbol{q}_{obs}$	Component of $\boldsymbol{q}$ from the observable subspace
$\boldsymbol{q}_{unobs}$	Component of $\boldsymbol{q}$ from the unobservable subspace
Q_k	Volumetric flow rate for the k^{th} stream
R_b	Nucleation rate
R, R'	Frames of reference
r	Cooling rate
s	Chord length
$\overline{s}$	Mean chord length
t	Time
Δt	Acquisition time frame
T	Temperature
$\boldsymbol{U}$	Orthonormal eigenvector of $\boldsymbol{A}$
$\boldsymbol{u}_i$	Eigenvectors of $\boldsymbol{A}$, basis vectors of $\boldsymbol{U}$
V_S	Scanned volume
V_T	Total volume of the slurry

V	Volume
$\bar{V}_{i,\text{one crystal}}$	Volume of one crystal of size $\bar{L}_i$
x, y, z	Cartesian Coordinates , frame of reference R
x', y', z'	Cartesian Coordinates, frame of reference R'
x_i	Input signal, exponential filter
y_i	Ouput signal, exponential filter

Greek symbols:

α	Weighting function
α_i	Projection coefficient for the population density
β	Shape factor for the gamma function
γ	Interfacial tension
γ_2	Normalizing coefficient for the gamma function
δ	Depth scanned by the laser
ε_{tol}	Tolerance on project error for $\boldsymbol{n}_1$
ε	Width scanned by the laser
θ_1	Degree of smoothing, exponential filter
θ_2	Scale parameter for the gamma function
λ_i	Eigenvalues of $\boldsymbol{A}$
λ_a	Parameter
μ	Viscosity
ρ	Density
$\sigma_{\max}$	Maximum noise level on $\boldsymbol{q}$
$\boldsymbol{\sigma}$	Standard deviation vector for the measurement noise on $\boldsymbol{q}$
$\dot{v}_S$	Scanning speed

$\mathbf{\Psi}$	Conversion matrix (octahedral crystals)
φ,ψ,θ	Euler angles

Abbreviations:

CLD	Chord-length density
CSD	Crystal size density
DSC	Differential scanning calorimetry
FBRM	Focused beam reflectance measurement
FDA	Food and Drug Administration
NMR	Nucleic Magnetic Resonance
PAT	Process analytical technology
PVM	Particle Vision Measurement
IR	Infra-red spectroscopy
XRD	X-Ray diffraction
ATR-FTIR	Attenuated total reflection Fourier transform infrared spectroscopy

SUMMARY

In the pharmaceutical and specialty chemical industries, batch crystallization is used widely in the production of high-value added species. It is widely recognized that product properties, some of which may be related directly to the utility of the drug, and downstream processes, such as tableting, are influenced by crystal morphology, size, and shape. The ability to observe on-line the evolution of the population density and detect a polymorphic transformation would constitute a major asset in understanding crystallizer operation and the phenomena that influence product quality.

Focused-beam reflectance measurement (FBRM) is among the process analytical technologies (PAT) that hold promise for enhanced monitoring of pharmaceutical crystallization. It is based on scattering of laser light and provides a methodology for on-line monitoring of a representation of the crystal population in either batch or continuous crystallization systems. Properly installed, the FBRM allows on-line determination of the chord-length density, which is a complex function of crystal geometry and is statistically related to the population density. A model based on the geometry of the crystal was therefore established to relate both densities and thus enable computation of the population density from a measured chord length density. The evolution of the population density as a function of time leads to the estimation of the supersaturation and therefore allows the determination of the systems kinetics. From there, the population balance can be solved.

Paracetamol is a common substance which exhibit polymorphism and is mainly used as an analgesic and antipyretic drug. The developed model was here applied to batch

cooling crystallization of paracetamol from ethanol solutions; this system was also used to explore the utility of FBRM data in detection of the polymorphic transformations. As different shapes generate different chord length densities, a transition from one polymorphic form with one specific crystal habit to another can be tracked through an efficient use of the FBRM.

The purpose of the present study is to use the FBRM to monitor the evolution of the crystallization process, develop a predictive model describing the evolution of the process, and monitor polymorphic transformation. The end results would be the possibility to implement a better control of the crystallization process that would ensure that downstream processing and product quality meet expectations.

CHAPTER 1

INTRODUCTION

1.1 Introduction

Batch crystallization is widely used in the chemical industry to produce high value added specialty compounds usually in small quantities or when the crystallization step is complex, for example high density systems or use of toxic chemicals. The most important industrial application lies in the pharmaceutical industry, as the majority of their production is constituted of solid compounds. The crystallization process defines the purity of the solid as well as its physical properties such as particle size and habit (Fachaux et al. 1995). Those two factors have a large impact on the physical properties and on the manufacturing processability of the final crystalline product (Table 1 - Shekunov & York 2000). Consequently, gaining in-depth knowledge of the phenomena of particle formation and crystallization is essential. Empirical methods have, thus far, provided a better understanding of those phenomena. Unfortunately, testing the purity and physical properties of the product via sampling and laboratory analysis, leads to an unfortunate waste of the precious material, as well as time and money. Therefore, an in-depth knowledge of the process is fundamental in order to implement an efficient control of crystallization.

It is essential to note that the pharmaceutical industry is highly regulated so as to ensure the safety of the end product. Thus, the possibilities of manipulation of the already approved process are strongly limited. Research efforts must therefore be oriented towards the development of reliable new methods that are based on the physical form of the solid to take into account the presence of highly non-spherical particle shapes. These

methodologies should require limited to no sampling so as to limit waste, be able to detect any physical change occurring through the process and also meet regulatory requirements. The Process Analytical Technology (PAT) initiative was derived from this challenge as a joint effort between the Food and Drug Administration (FDA) and the pharmaceutical industries to design reliable on-line measurement technology (Vanderhallen et al., 2002; Wood-Kaczmar, 2002 and Yu et al., 2004). The goal is to offer accurate and repeatable methods, with short analytical time and high resolution, for a wide range of particle sizes and shapes that do not require any pretreatment, such as dilution of the system studied. The main motives for the adoption of such a technique by the industry are mainly dependent upon factors such as: speed, cost and automated analysis of the crystal population. The development of the Focused Bean Reflectance Measurement (FBRM) follows the PAT initiative and offers a real-time analysis of the evolution of the crystal population.

A new methodology to study and analyze the crystallization process, through the use of the FBRM, will be presented here. The batch cooling crystallization of paracetamol in ethanol solutions will be used as a model system. A methodology based on the FBRM measurements will thus be developed to determine the kinetics of the system and establish a predictive model to describe the system through the use of population balance. Polymorphic transition was also investigated as a complementary study as this phenomenon is a key issue in the pharmaceutical industry.

Table 1. Solid-state properties defined by crystallization process and their relationship with specific characteristics of drug substances and drug products

Solid-state properties	Effect on drug
Structural	
Crystallinity (existence of amorphous and semi-crystalline forms)	Physical and chemical stability
Polymorphs	%RH profile (hygroscopicity)
Solvates (hydrates)	Solubility profile and dissolution rate
	All aspects of processing
Salts	
Crystal defects	
Dimensional	Processing behavior: bulk density,
Particle size distribution	agglomeration, flow/rheology, compaction,
Particle morphology	Particle permeability (i.e. particle
Particle surface structure	adsorption),
	Bioavailability (drug absorption),
	Consistency and uniformity of the dosage form
Chemical	
Organic and inorganic impurities, residual solvent and decomposition products	Toxicity
Chiral forms and chiral separation	
Sterility (microbial limits)	Chemical, physical and enantiomeric stability
Mechanical	
Brittle/ductile transitions, fracture stress, indentation hardness, stress/strain relaxation, yield pressure, Young's modulus	Milling and tableting behavior
Electrical	
Electrostatic charge distribution	Agglomeration and flow properties

1.2 Goal of the study

The purpose of this research is to propose a new methodology that provides real-time information on the evolution of the crystallization process based on on-line FBRM measurements. In order to collect in-depth knowledge on the crystallization, the behavior of the system has to be described as extensively as possible. Information on kinetics, solubility, and polymorphism is therefore necessary knowledge that needs to be derived from the proposed methodology. To obtain this information from the FBRM raw data, a mathematical model needs to be developed. In a previous study (Barthe 2006) the relationship between chord length and population densities was established for octahedral crystals. Thus, the evolution of a crystalline population can be followed through FBRM measurements (Barthe 2006).

Considering the fact that the pharmaceutical industry is highly regulated, any process adjustment or improvements of an already approved process is difficult, and optimization is therefore limited. The FBRM is an FDA approved device and can be used to efficiently monitor variations of the number and the geometry of the particles in the considered system. This study aims to provide a better understanding of the FBRM data, which will lead to the development of a predictive model through the use of population balances in order to design a more efficient process.

The study uses the crystallization of acetaminophen from ethanolic solution as a model system and is organized as follows. First, an overview of the basic concepts will be given. In Chapter 4, a model relating the chord length measurements to the population density is developed. This model allows us to have crucial information on the evolution of the crystallization. Next, a study describing how sensitive is the method to noise in

data, to inherent confounding measurements, or to shape variations is realized in order to better our analysis of the data by providing more insight on the method itself.

Then, we show how the FBRM measurements were used to determine the nucleation and growth kinetics.. The knowledge of the evolution of the population density versus time leads to the estimation of the supersaturation, which in turn leads to the estimation of the system's kinetics. So as to compute the growth kinetics, seeded experiments were designed in order to isolate this phenomenon and a model was developed to extract the kinetics from the data collected during those runs. Once the system is fully defined, a population balance model was used in order to establish a predictive model.

Finally, as Paracetamol is known to exhibit polymorphism and in the purpose of obtaining a better insight on the process, the FBRM was used to investigate polymorphic transitions.

CHAPTER 2

BACKGROUND

Crystallization of pharmaceutical compounds is a critical process in the pharmaceutical industry. Reliable in-depth information on the process is not easily accessed. The properties of the end product are highly dependant on the particle size density and the polymorphic form under which the considered drug crystallizes. In order to monitor different aspects, and further our understanding of the evolution of this manufacturing process, several tools and methods have been previously developed and are currently employed.

Most of the current measurement devices available to monitor crystallization processes need to be correlated with specific models. This range of techniques is referred to as chemometrics and includes, among many others, methods such as calibration, basic statistics, curve fitting and / or pattern recognition. Chemometrics models are often based on an assumed spherical shape of the considered crystals, assumption that can lead to a large deviation from reality as many pharmaceutical compounds often display a highly non-spherical geometry (Shekunov et al. 2007).

The main concern is that inconsistencies have been noticed between the results of these methods. This is most likely due to different assumptions, different treatments of the raw data and / or different pre-treatments of the solids. The main difficulty therefore lies in selecting, adopting and sometimes identifying the more suitable technique. The Process Analytical Technology (PAT) initiative was derived as a joined effort between

the FDA and the pharmaceutical companies to design reliable in-situ analytical technologies (Yu et al. 2004, Greenberg 2002) and thus address this issue.

2.1 Measurement of population density and kinetics

Efficiently monitoring the crystallization process to obtain information on kinetics, on the evolution of the solid population and / or to implement a control loop is a decisive step. Selecting one method from the wide assortment of measurement techniques and chemometrics methods available can be delicate (Shekunov & York 2000, Yu et al. 2004).

Usually a value related to the concentration of the solution is measured; chemometrics techniques are then used to estimate the supersaturation, the kinetics of the system and to obtain information on the crystal population. Sources of inaccuracies are mainly related to the chemometric method used such as calibration techniques (most of the models are based on spherical shape), sampling (leading to statistical error and loss of product) and sometimes pretreatment of the sample (dilution for example). Thus, for the purpose of lowering the sources of inaccuracies, it is preferable to select a tool that's adapted to the process (Shekunov et al. 2007).

There are different options to implement measurements of the particle's population throughout the process (Yu et al. 2004):

- In / off –situ laboratory analysis
- A sample stream for analysis (can be fed back into the system)
- Integration of sensors in the process, measurements realized in real-time (flow can be disturbed due to the insertion of a probe)

The main concern linked to the off line analysis is due to the delay induced by the laboratory analysis and the errors introduced by unreliable sampling processes and pre-treatment of the samples. Therefore, another option might be preferred.

Several analytical devices are available to monitor the evolution of the process; the most popular techniques are presented here.

- Microscopy and image analysis are commons techniques. They are the only ones to allow the observation of individual particles. The main limitation of these methods is linked to the sampling process, the sample has to be representative of the whole system, and the accuracy of the analysis has to be confirmed through other techniques (Russ 1990, Pons & Vivier 1990, Kaye et al.1997).

- Laser diffraction and static scattering techniques are becoming standards. They offer a short analytical time, a flexibility of operation and a high precision. Even though, these techniques present many advantages, they cannot be applied to a wide range of system (high concentration, high refractive index, needles-like crystals…) and often require a dilution of the sample (Van Antwerpen & Van Krevelen 1993, Malkin & McPherson1994 and Brown 1993).

- ATR-FTIR (Attenuated Total Reflectance combined with Fourier Transform Spectroscopy) is widely used. The main limitation of this technique is the fact that a strong calibration method is needed (Togkalidou et al. 2001).

- Dynamic light scattering (photon correlation spectroscopy) is primarily used to measure nanoparticulate systems due to the precision of the measurements for

the smaller sizes (Schrof et al. 1998). The offered measurement fails to provide information on the composition and optical properties of the system. Moreover, an important dilution of the sample is often required.

- Coulter counter is a proficient technique for the analysis of non-agglomerated and stable suspensions as it provides a fast and reproducible measurement over a wide size range (Kaye et al. 1999, Allen 1997). The downsides of these techniques are due to the fact that calibration is a critical step and that it cannot be applied to all systems (particles with extreme shapes or a hydrophobic system for example).

Other usual techniques include DSC, turbidimetry, densitometry, and ultrasonic attenuation. A wide variety of methodologies are thus available, the key limitations results from the chemometrics associated with the considered apparatus and used to exploit the raw data. The fact that inconsistencies have been observed in between the results given by different methodology constitute the main issue. Those errors are due to diversity of particle method of population analysis, interpretation of data and different process application. A major problem is to select and adopt which technique is the most relevant to the considered process.

A research challenge resides therefore in the development of a method based on the physical form of the solid, which can be highly non-spherical, that requires limited or no sampling. This technique should also allow the monitoring of major physical changes during the process and meets the FDA regulatory requirements as pharmaceutical processes are highly regulated.

2.2 Focused Beam Reflectance Measurement (FBRM)

PAT are measurement techniques that are spreading in laboratory and industrial applications where they provide reliable, in-situ, on-line information about the evolution of a process.

Among them, the FBRM offers a possibility to implement on-line monitoring of the evolution of a crystalline population by tracking changes in the number as well as in the geometry of the particles in the considered system.

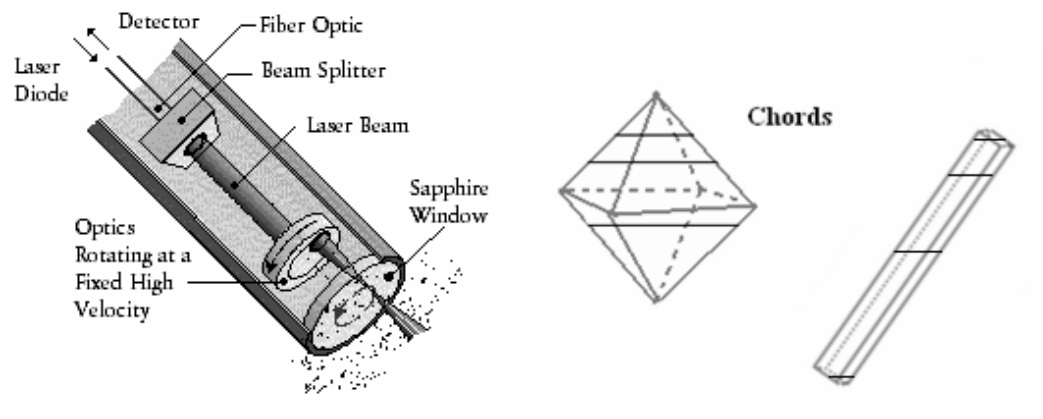

Figure 1. Tip of the Lasentec probe and schematic drawing of the chords scanned.

The FBRM consists of a focused laser beam rotating at a constant velocity that scans the particles located in front of the probe's sapphire window. When the light emitted by the laser hits a crystal, the sensors included in the probe record and analyze the backscattered signal. The collected data can be defined, as shown in Figure 1, as the distance between two edges of the particle; the FBRM calculates this distance by multiplying the rotating speed of the laser by the time of the corresponding backscattering signal. The instrument can acquire thousands of chord lengths per second and the range of detection is relatively wide, from 1 to 1000 μm. The counts of the chords

are organized in channels and expressed as a chord length histogram (chord counts / bins). The data collected by the Lasentec® software are available for direct observation on the computer screen and can be saved for further exploitation, the software is designed such as allowing the transfer of the data to an Excel™ file for future exploitation.

The histogram obtained through FBRM measurement gives an indication of the real population. The chord length density q can be calculated from this histogram and is statistically related to the population density n, which allows meaningful characterization of a crystal product. The relationship between the two densities has been the subject of various publications such as Worlitschek et al. 2005, Wynn 2003, Ruf et al. 2000 and Li & Wilkinson 2005. A model linking the two densities and based on the geometry of the particle was explored and will be detailed in a subsequent section (Chapter 3-4).

The FBRM present several advantages, it provides an on-line, real time analysis of the crystalline population. Errors due to pretreatment of the system such as sampling or dilution, which are frequently implemented with other measurement tools, is eliminated as the probe is directly inserted in the slurry. It is a robust instrument which presents a short analytical time, a high resolution for a wide range of particle size (1-1000 μm), that can be used in high concentrated solutions, and within hash conditions which is often the case in pharmaceutical processes. Chemometrics related to the use of this device are heavily based on the particle shape (Wynn 2003 and Ruf et al.2000).

Considering the fact that Pharma processes are heavily regulated, implementing any modification or control of an approved pharmaceutical process is tricky. The development of this apparatus followed the PAT initiative and is FDA approved. It can

thus be included without major issue into any pharmaceutical process as it is a rather non-invasive technology; the flow being already turbulent is only slightly influenced.

To summarize, the FBRM provides in-situ and real time information on the system evolution and efficiently tracks qualitative changes in particle population. Chemometrics are nonetheless essential to link the chord length density to the population density.

2.3 Observation of polymorphs

Polymorphism is an important aspect of the crystallization processes in pharmaceutical industry as many solids exhibit polymorphism (Brittain 1999). Polymorphism is defined as the ability of a substance to exist as two or more crystalline phases that have different arrangements and/or conformations of the molecules in the lattice. Those various crystalline forms exhibit the same chemical properties but differ in their physical, thermodynamic, spectroscopic, interfacial and mechanical properties (Table 2 - Brittain 1999). Thus properties such as solubility and morphology are affected. It is interesting to note that for pharmaceutical compounds, compression and filtration properties, as well as dissolution rate and bioavailability of the drug are altered.

Table 2. Physical properties that differ among various polymorphs (Brittain 1999)

Packing properties	Molar volume and density; Refractive index; Electrical/thermal conductivity; Hygroscopicity
Thermodynamic properties	Melting and sublimation temperatures; Internal energy (Structural energy); Enthalpy (Heat content); Heat capacity; Entropy; Free energy and chemical potential; Thermodynamic activity; Vapor pressure; Solubility
Spectroscopic properties	Electronic transitions (ultraviolet-visible absorption spectra); Vibrational transitions (infrared absorption spectra and Raman spectra); Rotational transitions (far infrared or microwave absorption spectra); Nuclear spin transitions (nuclear magnetic resonance spectra)
Kinetic properties	Dissolution rate; Rates of solid state reactions; Stability
Surface properties	Surface free energy; Interfacial tensions; Crystal habit (shape)
Mechanical properties	Hardness; Tensile strength; Compactibility, tableting; Handling, flow, and blending

Such diversity in crystal properties can be seen as an advantage but can also lead to major issues when uncalled for. The case of the HIV drug Ritonavir© in 1998 illustrate the large impact of polymorphism in the pharmaceutical industry, and how an unwanted and unforeseen change in the polymorphic form can lead to unfortunate consequences (Chemburkar et al. 2000). Stable and metastable forms can be identified. The stable form is the form with the lower solubility for the considered temperature range; several metastable forms can exist for the same substance. It is therefore preferred to base the formulation of a pharmaceutical drug on the thermodynamically stable form in order to limit the risk of phase transition. In some cases, the metastable form is preferred due to performance or regulatory issues (Morris 1999). For example, when the adsorption of the drug depends on the dissolution rate, as it is often the case for capsules or tablets, the metastable form may be preferred. In contrast, considering that the stable form is less likely to undergo transformation, it is preferentially used as a basis for suspensions (Guillory, 1999). This illustrates the fact that obtaining the adequate polymorph is crucial.

It is interesting to note that, a slight modification in the crystallization process, such as a variation of the cooling rate or of the solvent, will produce different polymorph. Thus the process needs to be proficiently controlled to ensure the quality, conformity and safety of the end product. Pharmaceutical industry is heavily controlled, the end product has to be fully specified and an unpredicted and unwanted change in properties can lead to safety issues as well as large loss of time and money. Therefore investigating the polymorphic aspect of the crystallization process is an essential step.

It is important to note that beside direct observation there is no real technique to observe the shape of the crystals. To date, most of the knowledge acquired has been empirical and was established mainly through off-line techniques. There are four main off-line methodologies: crystallographic (Powder X-Ray diffraction: XRD), spectroscopic (IR, Raman, NMR), microscopic (Electron Microscopy: EM) and thermal (Differential Scanning Calorimetry: DSC). Those techniques provide useful knowledge on the solid but require sampling and often pretreatment of the sample (KBr pills for IR), which can catalyze a polymorphic transformation of the compound. Subsequent to the introduction of PAT, an increase in the use of on-line methods was noticed (Reutzel-Edens 2006).

In this work, Paracetamol is used as a model system, also known as acetaminophen, it exists under three known polymorphic forms: monoclinic (Form I, stable, space group P21/n), orthorhombic (Form II, metastable, space group Pbca) and Form III (unstable, not characterized) (Beyer et al. 2001). A comparison between the lattices of Form I and II can be seen in Figure 2. According to Ostwald rule of stage, the first form to crystallize is the kinetically stable one (lower energy) and from there a transformation can occur leading to a thermodynamically stable form. The formation of another polymorphic form can either be realized through solution-mediated transformation or through solid-state transition. In the case of paracetamol, it was established that Form II leads to Form I through a solvent mediated transformation (Al-Zoubi et al. 2002).

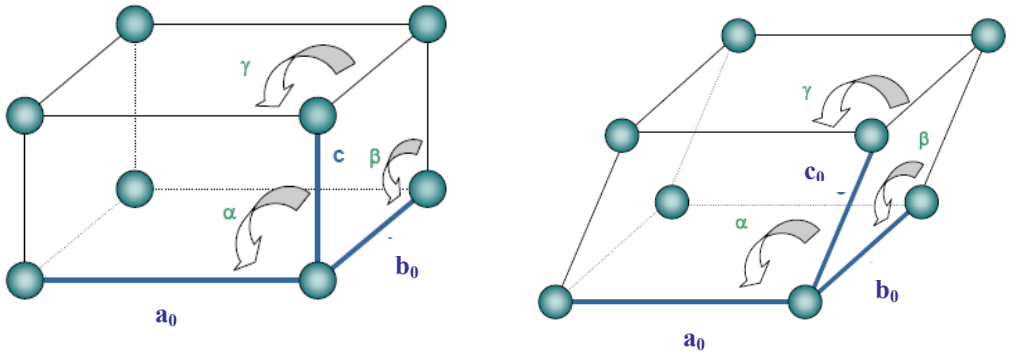

Figure 2. On the left, orthorhombic lattice ($a_0 \neq b_0 \neq c_0$ and $\alpha = \beta = \gamma = 90°$) - On the right, monoclinic lattice ($a_0 \neq b_0 \neq c_0$ and $\gamma = \beta = 90° \neq \alpha$)

Due to the ease of compression of Form II into tablets (Sun & Grant 2000), studies have been realized in order to synthesize and retain this particular polymorph (DiMartino et al., 1996 and Nichols & Frampton, 1998). It has been shown that under given experimental conditions, Form II can be produced at a lab scale, unfortunately, the crystals have to be harvested relatively early after nucleation to prevent any solvent mediated transformation, thus strongly limiting their growth (Al-Zoubi et al., 2002; DiMartino et al., 1996 and Nichols & Frampton, 1998).

Form I and Form II have been observed and characterized through techniques such as XRD, DSC and IR spectroscopy (Moynihan & O'Hare 2002; DiMartino et al., 1996 and Nichols & Frampton, 1998). Considering the extensive knowledge acquired on these polymorphs, Acetaminophen constitute a good system to investigate and monitor polymorphic transformation via FBRM, as this tool is highly sensitive to physical changes in the system (see Section 2.3). The FBRM can therefore, successfully and in a timely manner, provide accurate on-line information on such a transformation (O'Sullivan et al. 2003, O'Sullivan & Glennon 2005).

Being able to monitor polymorphic transformations on-line through FBRM measurements will provide useful insight on the crystallization process and also constitute a key point of this study.

CHAPTER 3

MODELING THE CHORD LENGTH DENSITY

As was previously stated, the FBRM allows on-line determination of the chord length density (CLD), which is statistically related to the crystal size density (CSD) and depends on the geometry of the crystal. In this chapter, we focus on establishing a model to describe the relationship between CLD and CSD. The purpose of the present chapter is to be able to use the FBRM to monitor the evolution of CLD, then restore the CSD and to obtain CSD characteristics.

3.1 Relating FBRM raw data to population density

Estimation of the length-weighted population density, n_1, from FBRM measurements requires relating n_1 to the quantity actually measured, which is a histogram (chord length counts / bin) that will be referred to as $\boldsymbol{k}(\bar{s}_i)$, where $\bar{s}_i$ is the mean chord length of the i^{th} bin as defined by Equation (1).

$$\bar{s}_i = \sqrt{s_i s_{i+1}} \tag{1}$$

The discretized chord length density, $q(s)$ can then be computed as

$$\boldsymbol{q}(\bar{s}_i) = \frac{\boldsymbol{k}(\bar{s}_i)}{\sum_{j=1}^{N_b} \left(\boldsymbol{k}(\bar{s}_j)\right)\left(s_{i+1} - s_i\right)} \tag{2}$$

where N_b is the number of bins in which counts are stored. The bins limits are fixed by the FBRM; for the present work, 90 channels or bins are used. $\boldsymbol{q}(s)$ is normalized as

$$\int_{0}^{\infty} q(s)ds \cong \sum_{i=1}^{N_b} \boldsymbol{q}\left(\overline{s_i}\right)\left(s_{i+1} - s_i\right) = \sum_{i=1}^{N_b} \frac{\boldsymbol{k}\left(\overline{s_i}\right)}{\sum_{j=1}^{N_b} \boldsymbol{k}\left(\overline{s_j}\right)} \frac{\left(s_{i+1} - s_i\right)}{\left(s_{i+1} - s_i\right)} = 1 \tag{3}$$

The chord-length density $\boldsymbol{q}(s)$ is then related to the length-weighted population density $\boldsymbol{n}_1(L)$ by:

$$\boldsymbol{q} = \boldsymbol{\Psi}\boldsymbol{n}_1 \tag{4}$$

where $\boldsymbol{\Psi}$ is a conversion matrix relating the two density vectors. The length weighted population $n_1(L)$ is related to the number size population density $\Delta N(L)$ according:

$$n_1(L) = \frac{\Delta N(L)\, L}{\int_{0}^{\infty} \Delta N(L)\, L\, dL} \tag{5}$$

The discretized form is given by:

$$\boldsymbol{n}_1(\overline{L}_i) = \frac{\Delta \boldsymbol{N}(\overline{L}_i)\, \overline{L}_i}{\sum_{j=1}^{N_b} \Delta \boldsymbol{N}(\overline{L}_j)\, \overline{L}_j\, \Delta L_j} \tag{6}$$

As shown in the next section, the evaluation of $\boldsymbol{\Psi}$ requires a detailed knowledge of the shape of the crystal or particle in the system and recognition that size influences the probability of a specific crystal or particle being "observed" by the FBRM. This complex relationship has been explored by numerous researchers: e.g., Ruf et al., 2000; Wynn, 2003; Worlitschek and Mazzotti, 2004; Li and Wilkinson, 2005; Li et al., 2005; and Barthe, 2006. Li based his model on a two-dimensional description of the particles, while Wynn proposed the use of moments to compute the conversion matrix and base his work on non-normalized functions. Ruf and Worlitschek worked with a more complex but

more realistic three-dimensional description of the particle, the logarithmic densities are normalized and the computation of the conversion matrix goes through the computation of individual chord length densities. In this work, the presented model will be based on a three dimensional representation of the crystals in agreement with Ruf and Worlitschek published work and on a logarithmic binning repartition.

3.1.1 Computation of Ψ

The FBRM utilizes reflections of a laser that is rotating at a fixed known velocity. The laser moves across an object in its path and, if the object has reflective properties, the sensor registers the time during which a reflection is measured. Based on the product of the rotating velocity and time of measurement, a chord length, *s,* between two edges of the object is calculated. Figure 3 illustrates how three-dimensional objects on the left of the figure are viewed in a two-dimensional form by the FBRM. Note in particular how possible chord lengths depend upon the orientation in space of the object and upon the path of the laser impinging on the object.

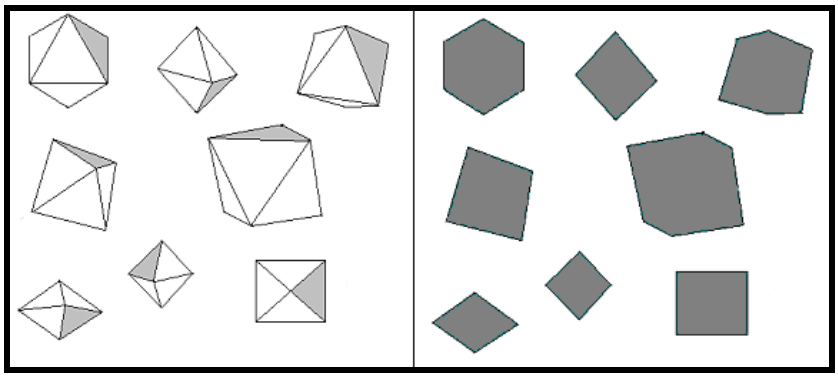

Figure 3. On the left are several possible orientations of a crystal or particle, while on the right is presented the distribution actually seen and measured by the FBRM (orthogonal 2D-projection of the particles located on the left). The laser beam is normal to the plane of the paper.

The first crucial step is to provide an accurate representation of the geometry of the particle. A mathematical description of the crystal shape was formulated according to:

$$\left|\frac{x}{a_0}\right|^{k_s} + \left|\frac{y}{b_0}\right|^{k_s} + \left|\frac{z}{c_0}\right|^{k_s} = 1 \tag{7}$$

where the parameters a_0, b_0, c_0 are a function of the dimensions of the crystal and k_s is determined by the crystal shape. For example, in the present study paracetamol is the crystal of interest. Because it crystallizes in an octahedral form, $a_0 = b_0 = c_0 = \sqrt[3]{\frac{\pi}{2\sqrt{2}}}L$ and k_s = 1 as displayed in Figure 4 (x, y, z are the cartesian coordinates in the frame of reference R). Where L is the characteristic size of the crystal, which is defined as the equivalent diameter.

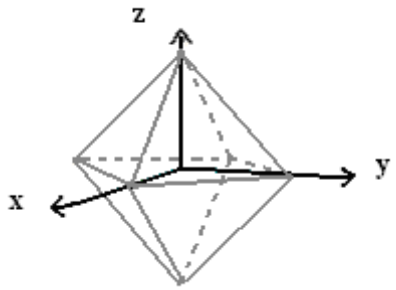

Figure 4. Representation of the octahedron in 3-dimensional space

A Monte Carlo simulation was implemented to take into account the numerous possible orientations of a crystal in a slurry. Equation (7) provided a description of the crystal with a specific orientation as displayed in Figure 4. This crystal move freely in the slurry and thus later present the orientation shown in Figure 5. According to Euler's rotation theorem, any rotation in space can be described using three angles. Consider the "x-convention" (Figure 6) which is defined such as the first rotation is by an angle φ

around the z-axis, the second is by an angle θ around the x-axis, and the third is by an angle ψ around the z-axis. Thus the frame of reference R becomes R′, where x', y', z' are the cartesian coordinates in the new frame of reference R′.

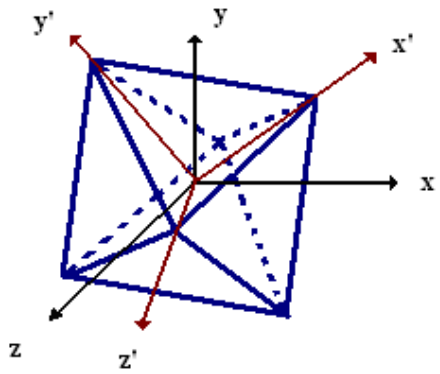

Figure 5. Random orientation of the crystal in a 3-dimensional space

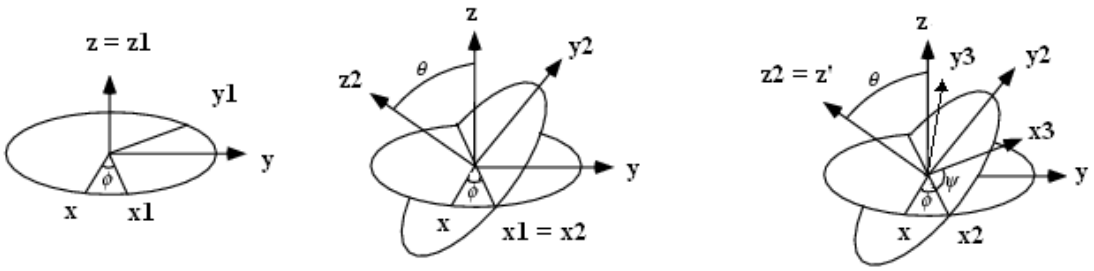

Figure 6. Euler Angles (Margenau, 1956)

The next step is thus to include this random orientation of the crystal into the model. This was accomplished through the use of Euler's Angles and Euler's Theorem (Margenau & Murphy, 1956 and 1964) by using the rotation matrix:

$$M = \begin{bmatrix} \cos\theta\cos\psi - \cos\theta\sin\varphi\sin\psi & \cos\psi\sin\varphi + \cos\theta\cos\varphi\sin\psi & \sin\theta\sin\psi \\ -\cos\psi\cos\theta\sin\varphi - \sin\psi\cos\varphi & \cos\psi\cos\theta\cos\varphi - \sin\psi\sin\varphi & \sin\theta\cos\psi \\ \sin\theta\sin\varphi & -\sin\theta\cos\varphi & \cos\theta \end{bmatrix} \quad (8)$$

The crystals geometry is thus defined in the frame of reference *R'* by:

$$|x'|+|y'|+|z'|=\left|\sqrt[3]{\frac{\pi}{2\sqrt{2}}}L\right| \tag{9}$$

To provide an accurate description of the particle geometry into a three-dimensional Euclidian space in the frame of reference *R*, the coordinates in both frames of reference are linked through the rotation matrix *M*, as:

$$\begin{bmatrix} x' \\ y' \\ z' \end{bmatrix} = \boldsymbol{M} \begin{bmatrix} x \\ y \\ z \end{bmatrix} \tag{10}$$

The equation describing the crystal's shape thus becomes:

$$\left|\left(M_{11}x+M_{12}y+M_{13}z\right)\right|+\left|\left(M_{21}x+M_{22}y+M_{23}z\right)\right|+\left|\left(M_{31}x+M_{32}y+M_{33}z\right)\right|=\left|\sqrt[3]{\frac{\pi}{2\sqrt{2}}}L\right| \tag{11}$$

The generation of random values for the three angles φ, θ and ψ modeling a random orientation was the starting point of the Monte Carlo simulation. For each randomly selected orientation of a crystal of a given size *L* and shape, an orthogonal projection of the shape was generated as shown in Figure 7. This projection models what is actually viewed by the FBRM (Figure 3).

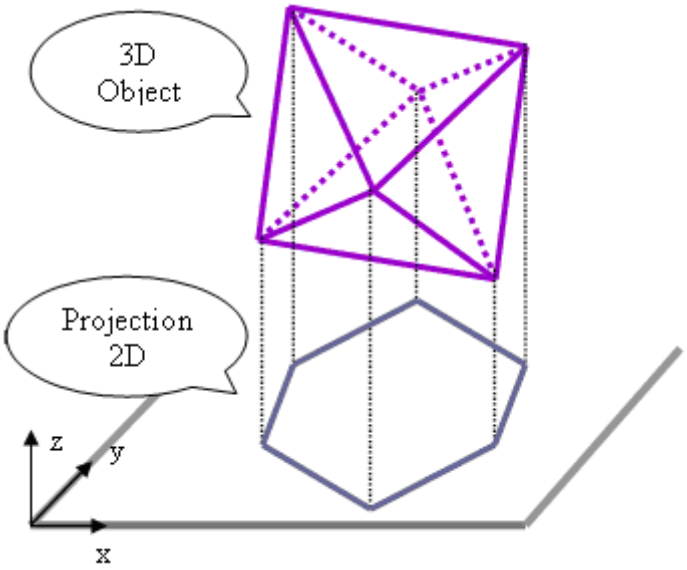

Figure 7. Representation of the shape viewed by the FBRM

From this projection onto the $z = 0$ plane, a histogram was computed as shown in Figure 8.

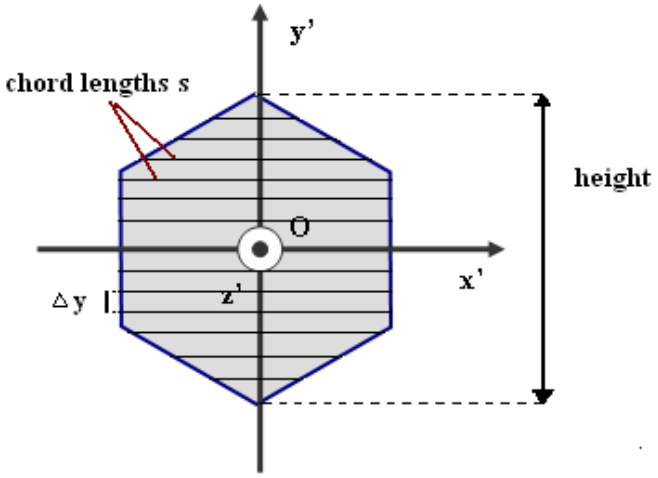

Figure 8. Computation of the chord length histogram (counts / bins)

In order to properly define the projected shape and be able to accurately compute the histogram, for each y_i defined by equations (12) and (13), the corresponding i^{th} slice of the crystal along the x,z-plane is considered (Figure 9). A search for the longest

distance s_i projected on the x-axis is then realized over the z_j, defined by equations (14) and (15). The chord length s_i, corresponding to the y_i considered was therefore obtained. The step size Δy is fixed.

$$y_i = i\Delta y \tag{12}$$

$$\forall i \quad -\sqrt[3]{\frac{\pi}{2\sqrt{2}}}L \geq y_i \geq \sqrt[3]{\frac{\pi}{2\sqrt{2}}}L \tag{13}$$

Similar definitions are applied to the z-axis, the step size Δz is fixed.

$$z_j = j\Delta z \tag{14}$$

$$\forall j \quad -\sqrt[3]{\frac{\pi}{2\sqrt{2}}}L \geq z_j \geq \sqrt[3]{\frac{\pi}{2\sqrt{2}}}L \tag{15}$$

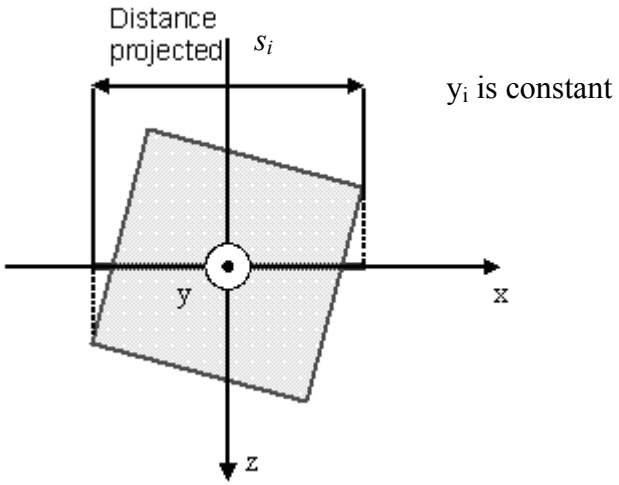

Figure 9. Representation of the i[th] slice of the crystal along the x,z-plane - Calculation of the projected chord length

For each orientation, the chords s_i were classified into a histogram (chord length counts / bin). This histogram, established for a given orientation, was then normalized and weighted by the projected height of the particle to reflect the higher influence of larger

particles to obtain $q_p(s, L)$. The weighted histograms resulting from all the randomly generated orientations were assembled to approximate the individual chord length density $q_p(s, L)$ of the considered crystal of characteristic size L. This density was then normalized according to the equation:

$$\int_0^{\infty} q_p(s,L)ds = 1 \tag{16}$$

This equation can be normalized to obtain a discretized version:

$$\sum_{i=1}^{N_b} \boldsymbol{q}_p\left(\overline{s_i}, \overline{L_j}\right)\left(s_{i+1} - s_i\right) = 1 \tag{17}$$

To provide an illustration, the calculated length-weighted chord length density and the corresponding specified length weighted population density are shown in Figure 10 for a population constituted of octahedrons of characteristic size L = 100 μm. A peak is observed for the chord length $s = \sqrt[3]{\frac{\pi}{2\sqrt{2}}}L$, which was expected due to a ratio of $\sqrt[3]{\frac{\pi}{2\sqrt{2}}} \sim 1.3$ between the characteristic length and the length of the edge of the particle. This shows that the chord length density is highly dependant on the geometry of the crystal. In this example, we use N_b = 90 bins with logarithmic distribution, which corresponds to the setting used with the FBRM.

The displayed chord length density was estimated through the computation of 5,000 random orientations to provide a reliable statistical analysis. Similar simulations were run for 3,000, 5,000 and 10,000 random orientations; the result obtained for 5,000 and 10,000 were comparable while the results obtained for 3,000 orientations were

irregular. Thus, 5,000 random orientations were determined to be sufficient for the octahedral shape here considered.

The individual chord length density $\boldsymbol{q}_{\mathrm{p}}(s, L)$ for a crystal of a given characteristic size L is thus computed. The same procedure was repeated for a representation of sizes defined by the FBRM for a span of 90 bins within the range of 1 to 1000 μm. The same bins are used for s and L.

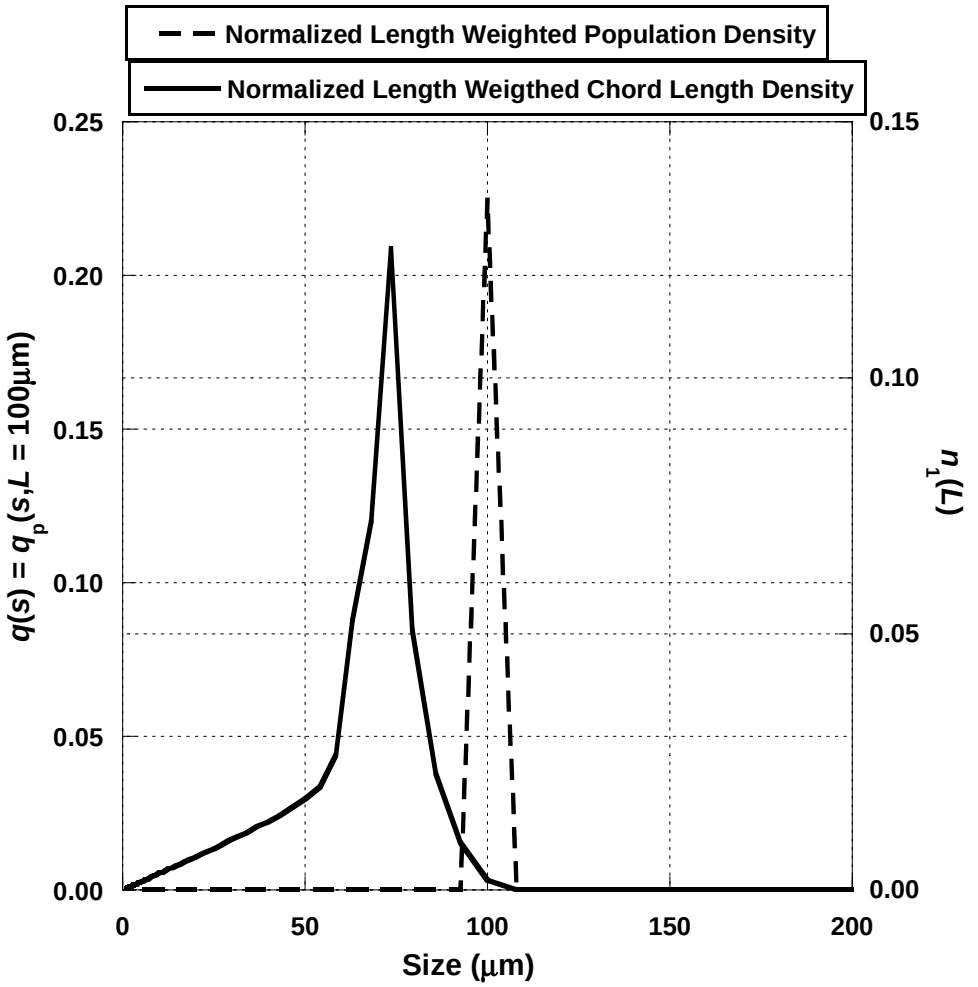

Figure 10. Simulated, normalized length-weighted chord length density for an octahedron of characteristic size L = 100 μm versus normalized population density

The individual simulated chord length densities $\boldsymbol{q}_{\mathrm{p}}(s, L)$ were used to build, in a step-by-step manner, the conversion matrix $\boldsymbol{\Psi}$, as illustrated by equations (18) to (21). The relationship between the normalized length weighted population density $n_1(L)$ and the normalized chord length density $q(s)$ is defined by :

$$q(s) = \int_0^{\infty} q_{\mathrm{p}}(s, L) n_1(L)\, dL \tag{18}$$

where $n_1(L)$ is related to the number size population density $\Delta N(L)$ according to Equation (5). This equation can then be discretized to form:

$$\boldsymbol{n}_1(\overline{L_i}) = \frac{\Delta \boldsymbol{N}(\overline{L_i})\,\overline{L_i}}{\sum_{j=1}^{N_{\mathrm{b}}} \Delta \boldsymbol{N}(\overline{L_j})\,\overline{L_j}\,\left(L_{j+1} - L_j\right)} \tag{19}$$

Equation (18) is then discretized, thus defining the matrix $\boldsymbol{\Psi}$ as a function of $\boldsymbol{q}_{\mathrm{p}}(s, L)$ as shown below:

$$\boldsymbol{q}\left(\overline{s_i}\right) = \sum_{j=1}^{N_{\mathrm{b}}} \boldsymbol{q}_{\mathrm{p}}\left(\overline{s_i}, \overline{L_j}\right)\left(L_{j+1} - L_j\right) \boldsymbol{n}_1\left(\overline{L_j}\right) = \sum_{j=1}^{N_{\mathrm{b}}} \boldsymbol{\Psi}(i, j) \boldsymbol{n}_1\left(\overline{L_j}\right) \tag{20}$$

$\boldsymbol{q}_{\mathrm{p}}(s,L)$ was computed for all s and L as previously described thus fully defining the real matrix $\boldsymbol{\Psi}$:

$$\boldsymbol{\Psi} \in \mathbb{R}^{90*90} \qquad \boldsymbol{\Psi}(i, j) = \boldsymbol{q}_{\mathrm{p}}\left(\overline{s_i}, \overline{L_j}\right)\left(L_{j+1} - L_j\right) \tag{21}$$

3.1.2 Linking the chord length density $q(s)$ to the population density $n(L)$

The population density $\boldsymbol{n}$ obtained from a sieve analysis is volume-weighted, while FBRM data leads to a length-weighted population density $\boldsymbol{n}_1(L)$. A weighting function $\alpha(L)$ is needed to account for this difference and enable a comparison between

restored (i.e. values from FBRM data) and true population densities (equations (25) and (26)).

$$n_1(L) = \alpha(L)\ n(L) \tag{22}$$

$n_1(L)$ and $n(L)$ are both linked to the number size population density $\Delta N(L)$ according to equations (5) and (23).

$$n(L) = \frac{\Delta N(L)\, L^3}{\int_0^{\infty} \Delta N(L)\, L^3\, dL} \tag{23}$$

This equation can then be discretized to form:

$$\boldsymbol{n}(\overline{L_i}) = \frac{\Delta \boldsymbol{N}(\overline{L_i})\, \overline{L_i}^3}{\sum_{j=1}^{N_b} \Delta \boldsymbol{N}(\overline{L_j})\, \overline{L_j}^3 \left(L_{j+1} - L_j\right)} \tag{24}$$

Thus the weighting function $\alpha(L)$ can be expressed through the following equation:

$$\alpha(L) = \frac{1}{L^2}\, \frac{\int_0^{\infty} \Delta N(L)\, L^3\, dL}{\int_0^{\infty} \Delta N(L)\, L\, dL} \tag{25}$$

It can be discretized to form:

$$\boldsymbol{\alpha}(\overline{L_j}) = \frac{1}{\overline{L_j}^2}\, \frac{\sum_{i=1}^{N_b} \Delta \boldsymbol{N}(\overline{L_i})\, \overline{L_i}^3 \left(L_{i+1} - L_i\right)}{\sum_{k=1}^{N_b} \Delta \boldsymbol{N}(\overline{L_k})\, \overline{L_k} \left(L_{k+1} - L_k\right)} \tag{26}$$

The following example illustrates the previous methodology. Consider a population consisting of equal numbers of 10 μm and 100 μm octahedral crystals. The length-weighted population density $\boldsymbol{n}_1(L)$ can be calculated by Equation (19), with the

results shown by the dashed lines in Figure 11. Using the conversion matrix evaluated by Equation (21), the chord-length density $\boldsymbol{q}(s)$ can be calculated by Equation (20) to give the solid curve in Figure 11. As expected, the larger crystals have a larger influence on the overall density, sustaining that the probability of the FBRM laser impinging on a crystal is a function of its size.

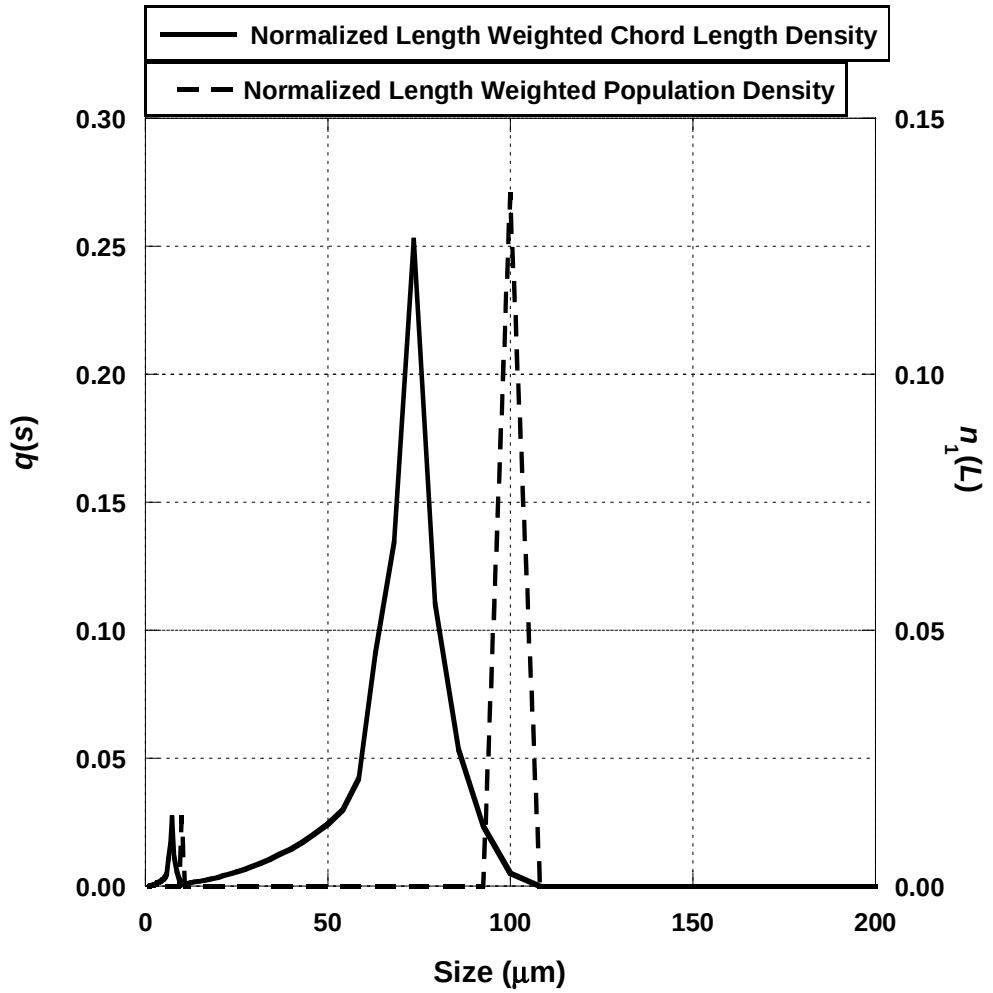

Figure 11. Overall normalized length-weighted chord length density $q(s)$ versus normalized population density $n_1(L)$ for the considered population of octahedron

Computing the chord length density from the population density is a relatively straightforward procedure. The next step is to invert the process in order to obtain the population density $\boldsymbol{n}$ from the actual FBRM measurements $\boldsymbol{k}$.

3.2 Restoration of the population density from the FBRM raw data

The experimental measurements can be linked to the length-weighted chord length density $\boldsymbol{q}(\overline{s_i})$ according to Equation (2) through the conversion matrix $\boldsymbol{\Psi}$. It is essential to note that the matrix $\boldsymbol{\Psi}$ cannot be accurately inverted for crystals whose shapes are non-spherical, this inversion process is the focus of the next chapter.

CHAPTER 4

ANALYSIS OF THE RESTORATION METHOD

To review, the relationship between crystal population density and CLD obtained from FBRM is complicated and depends on the size and shape of the crystals. While estimation of chord-length density from the population density is relatively straightforward, the inversion of this procedure is problematic because the problem may be ill-conditioned for non-spherical particles. Since the relationship is a function of the crystal geometry, this chapter considers various non-spherical shapes, including highly challenging needles. In the present chapter, we examine how measurements from an instrument that has gained significant use can be converted to an accurate estimation of the population density.

There have been several research groups that have made progress in dealing with this problem; e.g. there are several publications that analyze the relationship between population and chord-length densities and the recovery of the population density from the CLD (Barthe et al. 2006, Li et al.2005, Ruf et al. 2000, Worlitschek et al. 2003, and Wynn 2003). In all of these, crystal shape is the main factor influencing the relationship. For example, Li and Wilkinson developed a model based on a 2-D elliptical representation of the crystal and used an iterative non-negative least-squares method to estimate the size distribution (Li et al. 2005). Wynn used a method that can present difficulties with instability and is also based on a 2-D silhouette of the particles (Wynn 2003). Mazzotti and co-workers used a 3-D representation of the particle and defined a relationship between CLD and population density that goes through the computation of a conversion matrix (Ruf et al. 2000). Constraints were also implemented to enable the

estimation of population density and were found necessary to overcome the issue of ill-conditioning of the matrix that prevented the pure inversion of the matrix (Ruf et al. 2000, Worlitschek et al. 2003, 2005).

A goal of the present work is to develop a new, accurate and constraint-free methodology for estimation of the population density from CLD measurements for various crystal shapes. The results are expected to lead to a better understanding of the fundamental limits inherent to the restoration of the population density for a non-spherical crystalline population, and to provide an analysis tool for determining the best settings on the FBRM. The first step in the methodology is computation of the conversion matrix, which is based on Monte Carlo sampling of random crystal orientations and is a function of the crystal geometry (Barthe et al. 2006). This step is similar to the approach proposed by Mazzotti and co-workers (Ruf et al. 2000). Unfortunately, the inversion problem — i.e. computation of population density from the CLD — is inherently ill-conditioned, and constraints on the restored population density must be imposed in order to obtain a unique solution for the population density. The constraints used by Mazzotti and co-workers typically have a physical basis: for example, non-negativity and normalization of the densities (Ruf et al. 2000, Worlitschek et al. 2003). However, additional constraints may still be needed. Approaches employed include regularization to enforce smoothness of the solution, and upper bounds on the residual between the measured CLD and the model-predicted value (Ruf et al. 2000, Worlitschek et al. 2003, 2005). Such constraints enable the computation of a unique solution. However, it is not clear that this unique solution for the population density is accurate. For example, some features of the population density might be overlooked due to the smoothness constraint imposed

through regularization. In a previous study, we used this approach to estimate the population density from a measured CLD for paracetamol crystallized from an ethanol solution (Barthe et al. 2006). Good agreement was shown in comparing estimates recovered from FBRM measurements with those from ex-situ sieving measurements.

The existing approaches do not give a full understanding of which features in the population density can be accurately estimated. Moreover, the limits and robustness of the restoration process are not well-understood or documented, and as a result there has been little industrial implementation of the direct inversion method. In this chapter, a comprehensive comparison of the inversion process is given for octahedral crystals, elongated slabs, and needles. For each shape, several cases involving different types of population density functions (gamma, exponential and bimodal) are analyzed, and the influence of noise in the CLD on the restoration process, as well as the performance of the method compared to the Constrained Least Square Method (CLSM), is examined.

The method proposed here is based on a principal component analysis and the spectral method that is used to generate a basis for the population density; the basis elements are then divided into observable and unobservable subspaces. Population densities lying only in the observable subspace can be accurately reconstructed, while those lying in the unobservable subspace cannot. Additionally, we note that a combined approach is also possible for the inversion in which regularization and other constraints can be applied, as suggested by Mazzotti and co-workers (Ruf et al. 2000, Worlitschek et al. 2003, 2005).

4.1 Methodology

As seen in Chapter 3, the relationship between the length-weighted population density $\boldsymbol{n}_1$ and the chord-length density $\boldsymbol{q}$ is defined by

$$\boldsymbol{q} = \boldsymbol{\Psi} \boldsymbol{n}_1 \tag{27}$$

where $\boldsymbol{\Psi}$ is a square conversion matrix relating the two vectors, $\boldsymbol{n}_1$ and $\boldsymbol{q}$, which describe the densities. The matrix $\boldsymbol{\Psi}$ is computed using Monte Carlo simulations and strongly depends on the geometry of the crystals [Barthe et al. 2006, Ruf at al. 2000].

As part of our inversion process, we apply the spectral method, which can only be applied to symmetric matrices. Therefore, both sides of Equation (27) are multiplied by $\boldsymbol{\Psi}^T$, where the matrix $\boldsymbol{\Psi}^T\boldsymbol{\Psi}$ is symmetric:

$$\boldsymbol{\Psi}^T \boldsymbol{q} = \boldsymbol{\Psi}^T \boldsymbol{\Psi} \boldsymbol{n}_1 \tag{28}$$

Defining $$\boldsymbol{A} = \boldsymbol{\Psi}^T \boldsymbol{\Psi} \tag{29}$$

and $$\boldsymbol{b} = \boldsymbol{\Psi}^T \boldsymbol{q} \tag{30}$$

Equation (28) becomes $$\boldsymbol{b} = \boldsymbol{A} \boldsymbol{n}_1 \tag{31}$$

where $\boldsymbol{A}$ is a real symmetric matrix and $\boldsymbol{b}$ is a real vector.

The goal here is to determine when the population density $\boldsymbol{n}_1$ can be accurately estimated. Therefore, the measurement of the chord-length density $\boldsymbol{q}$ will be used as a starting point, and the spectral method will be used to estimate the population density. A basis $\boldsymbol{U}$ for the space of $\boldsymbol{n}_1$ is computed using principal component analysis of $\boldsymbol{\Psi}$, which is equivalent to computing the eigenvectors $\boldsymbol{u}_i$ of matrix $\boldsymbol{A}$. An advantage of computing this orthonormal basis is that the inversion of the relationship between both densities, as shown in Equation (27), can be accomplished using scalar computations only without requiring a matrix inversion. In the new coordinate system defined by this basis, some coordinates may be ill-conditioned, which will be indicated by their near-zero eigenvalues λ_i. We

refer to these coordinates as "unobservable" in the FBRM measurement. This approach allows us to analyze the inversion process and to compute reconstructions of $\boldsymbol{n}_1$ in the observable subspace. The accuracy of the recovery and the sensitivity to noise are also investigated and quantified.

4.1.1 Spectral method

Assume that $\boldsymbol{A}$ is a real symmetric matrix and its eigenvalues λ_i and eigenvectors $\boldsymbol{u}_i$ have been computed. An orthonormal basis $\boldsymbol{U}$ can be defined using the eigenvectors, and all eigenvalues satisfy $\lambda_i \geq 0$ (Beers 2007). Therefore, it is possible to describe any real vector $\boldsymbol{b}$ by its projection onto this basis according to the following equation:

$$\boldsymbol{b} = \sum_{i=1}^{m} \frac{(\boldsymbol{u}_i \bullet \boldsymbol{b})}{(\boldsymbol{u}_i \bullet \boldsymbol{u}_i)} \boldsymbol{u}_i = \sum_{i=1}^{m} (\boldsymbol{u}_i \bullet \boldsymbol{b}) \boldsymbol{u}_i \tag{32}$$

Because the basis is normal, $\boldsymbol{u}_i \bullet \boldsymbol{u}_i = 1$. To solve Equation (31), we express $\boldsymbol{n}_1$ in terms of the basis $\boldsymbol{U}$, with the α_i defined as real but unknown scalar coefficients.

$$\boldsymbol{n}_1 = \sum_{i=1}^{m} \alpha_i \boldsymbol{u}_i \tag{33}$$

Therefore, Equation (31) becomes

$$\boldsymbol{A}\left(\sum_{i=1}^{m} \alpha_i \boldsymbol{u}_i \right) = \sum_{i=1}^{m} (\boldsymbol{u}_i \bullet \boldsymbol{b}) \boldsymbol{u}_i \tag{34}$$

Since $\boldsymbol{A}$ is a linear operator,

$$\sum_{i=1}^{m} \alpha_i \boldsymbol{A} \boldsymbol{u}_i = \sum_{i=1}^{m} (\boldsymbol{u}_i \bullet \boldsymbol{b}) \boldsymbol{u}_i \tag{35}$$

and λ_i and $\boldsymbol{u}_i$ are, respectively, the eigenvalues and eigenvectors associated with $\boldsymbol{A}$, such that

$$\boldsymbol{A}\boldsymbol{u}_i = \lambda_i \boldsymbol{u}_i \tag{36}$$

Equation (35) can be simplified to

$$\sum_{i=1}^{m} \alpha_i \lambda_i \boldsymbol{u}_i = \sum_{i=1}^{m} (\boldsymbol{u}_i \bullet \boldsymbol{b}) \boldsymbol{u}_i \tag{37}$$

Therefore,
$$\alpha_i = \frac{(\boldsymbol{u}_i \bullet \boldsymbol{b})}{\lambda_i}, \; i = 1,..m \tag{38}$$

Equation (31) can now be solved for $\boldsymbol{n}_1$,

$$\boldsymbol{n}_1 = \sum_{i=1}^{m} \left(\frac{(\boldsymbol{u}_i \bullet \boldsymbol{b})}{\lambda_i} \right) \boldsymbol{u}_i \tag{39}$$

We use Equation (17) to compute $\boldsymbol{n}_1$ from the chord-length density $\boldsymbol{q}$, which is the foundation for our estimation of population densities from chord-length measurements. Considering that λ_i is the denominator in Equation (39), this method can only be applied if all eigenvalues are non-zero. However, any eigenvectors that have zero eigenvalues should not be inverted anyway, since they represent features in $\boldsymbol{n}_1$ that have no influence on $\boldsymbol{q}$. The eigenvectors are thus divided into two subsets and corresponding subspaces: an observable set that corresponds to non-zero eigenvalues, and an unobservable set corresponding to zero eigenvalues. Eigenvalues that are approximately zero correspond to ill-conditioned coordinates and they are also included in the unobservable subspace. They represent features in $\boldsymbol{n}_1$ that have a negligible effect on $\boldsymbol{q}$. We arrange the eigenvalues in ascending order, and m' is defined to delineate the two subspaces. Thus:

$$\boldsymbol{n}_{1,\text{obs}} = \sum_{i=m'+1}^{m} \alpha_i \boldsymbol{u}_i \tag{40}$$

$$\boldsymbol{n}_{1,\text{unobs}} = \sum_{i=1}^{m'} \alpha_i \boldsymbol{u}_i \tag{41}$$

Only the observable portion of $\boldsymbol{n}_1$ can be estimated from $\boldsymbol{q}$, so Equation (39) is replaced with the modified version:

$$\boldsymbol{n}_{1,\text{est}} = \sum_{i=m'+1}^{m} \left(\frac{(\boldsymbol{u}_i \bullet \boldsymbol{b})}{\lambda_i} \right) \boldsymbol{u}_i \tag{42}$$

In the absence of noise in the chord-length measurement, $\boldsymbol{n}_{1,\text{obs}} = \boldsymbol{n}_{1,\text{est}}$. Ideally, $\boldsymbol{n}_{1,\text{obs}} \cong \boldsymbol{n}_1$ and $\boldsymbol{n}_{1,\text{unobs}} \cong \boldsymbol{0}$, but if this is not the case, then an accurate estimate of $\boldsymbol{n}_1$ cannot be obtained from the FBRM measurements, at least not without additional information on the characteristics of $\boldsymbol{n}_1$.

The spectral method can be used to analyze the estimation process for a pre-specified population density $\boldsymbol{n}_1$ (Analysis), or it can be used to estimate an unknown $\boldsymbol{n}_1$ from FBRM measurements (Estimation). In practice, the analysis should be performed for expected values of $\boldsymbol{n}_1$, prior to the use of the method to estimate the unknown $\boldsymbol{n}_1$. We provide stepwise procedures of the two applications in the following summaries:

4.1.2 Analysis

1. Determine the shape of the crystals, the accuracy ε_{tol} desired in the estimated $\boldsymbol{n}_1$, and the standard deviation σ of the measurement noise for each bin in $\boldsymbol{q}$.
2. Compute the conversion matrix $\boldsymbol{\Psi}$ for the desired shape and then the corresponding symmetric matrix $\boldsymbol{A}$, as defined by Equation (29).

3. Compute the eigenvalues and eigenvectors of $\boldsymbol{A}$. Plot the eigenvalues λ_i.

4. Determine the cutoff (m') to achieve the desired accuracy in $\boldsymbol{n}_1$

$$\sqrt{\frac{\sum_{i=1}^{N_b} e_i^2}{\sum_{i=1}^{N_b} n_{1,i}^2}} \leq \varepsilon_{tol} \tag{43}$$

$$e_i = n_{1,i} - n_{1,est,i} \tag{44}$$

where e_i is the error in $\boldsymbol{n}_1$ in the i^{th} bin. The value of m' is determined by projecting $\boldsymbol{n}_1$ onto different subspaces via Equation (42) (i.e. varying m'), until the error in Equation (21) is less than ε_{tol}. m' should be as large as possible while still achieving ε_{tol}, since small λ_i will tend to amplify FBRM noise in $\boldsymbol{q}$ during the inversion process, which is due to the eigenvalue term in the denominator of Equation (42).

5. Add a zero-mean noise vector $\boldsymbol{v}$ with standard deviation vector $\boldsymbol{\sigma}$ to $\boldsymbol{q}$, such that $\boldsymbol{q} = \boldsymbol{\Psi n}_1 + \boldsymbol{v}$. The cut-off m' may need to be adjusted depending on this noise level. If $\lambda_{m'+1} < 1$, noise in $\boldsymbol{q}$ will be amplified in $\boldsymbol{n}_{1,\text{est}}$. However, if $\boldsymbol{\sigma}$ is small, some amplification may still be acceptable. Our guideline for the choice of m' is that $\frac{\sigma_{max}}{\lambda_{m'+1}} < \varepsilon_{\text{tol}} \sqrt{\sum_{i=1}^{N_b} n_i^2}$. The left-hand side is the noise expected in $\boldsymbol{n}_1$, due to the sensor noise being amplified through the conversion matrix. The right side is the typical error allowed in the noise-free estimate $\boldsymbol{n}_{1,\text{obs}}$ as in Equation (21). If this criterion is not met, noise will cause significant error in the estimate, and it will be necessary either to increase ε_{tol} or to decrease the noise level by, for example,

increasing the integration time of the FBRM, in order to achieve a final estimate with ε_{tol}.

6. Compute $\boldsymbol{n}_{1,est}$ using Equation (42), for several realizations of the sensor noise, and verify that $\boldsymbol{n}_1 \cong \boldsymbol{n}_{1,est}$ within accuracy ε_{tol}.

A more detailed error propagation analysis could be performed in Step 5, using the conversion matrix $\boldsymbol{\Psi}$ and the linearity of the equations. However, since $\boldsymbol{\Psi}$ is of order 1, due to the normalized nature of $\boldsymbol{q}$ and $\boldsymbol{n}_1$, our guideline stated above also provides reasonable predictions.

4.1.3 Estimation

When the goal is to estimate an unknown $\boldsymbol{n}_1$ from a measured noisy $\boldsymbol{q}$, the following procedure can be used:

1. Determine the shape of the crystals, the accuracy ε_{tol} desired in the estimated $\boldsymbol{n}_1$, and the standard deviation σ of the measurement noise for each bin in $\boldsymbol{q}$. In general the noise level will not be known exactly, but can be estimated from repeated experiments, steady-state experiments, or even a stochastic model of the crystallization process.

2. Compute the conversion matrix $\boldsymbol{\Psi}$ for the desired shape, and then the corresponding symmetric matrix $\boldsymbol{A}$ as defined by Equation (29).

3. Compute the eigenvalues and eigenvectors of $\boldsymbol{A}$. Plot the eigenvalues λ_i.

4. Select m' based on the FBRM noise level, using $\frac{\sigma_{max}}{\lambda_{m'+1}} < \varepsilon_{\text{tol}} \sqrt{\sum_{i=1}^{N_b} n_i^2}$. This criterion is used to set m' so that the effect of measurement noise of $\boldsymbol{n}_1$ does not exceed ε_{tol}. (Note that this does not guarantee a good reconstruction of $\boldsymbol{n}_1$ in the observable subspace.)

5. Use Equation (42) to compute $\boldsymbol{n}_{1,\text{est}}$.

There is no guarantee on the accuracy of the reconstruction in the observable subspace, since $\boldsymbol{n}_1 = \boldsymbol{n}_{1,\text{obs}} + \boldsymbol{n}_{1,\text{unobs}}$, and $\boldsymbol{n}_{1,\text{unobs}}$ cannot be recovered by definition since $\boldsymbol{q}$ is not sensitive to this portion of $\boldsymbol{n}_1$. If $\boldsymbol{n}_{1,\text{unobs}}$ is not approximately zero, then there will be significant error in the reconstruction. This is why it is important to perform the analysis procedure for typical expected $\boldsymbol{n}_1$ vectors, and to examine the eigenvalue spectrum. In the Results and Discussion section, we observe that the basis vectors for low values of m' tend to be at high frequency and may not be needed to reconstruct typical $\boldsymbol{n}_1$ distributions. To summarize, it is clearly not possible to reconstruct every possible $\boldsymbol{n}_1$ vector for a conversion matrix that is not full rank. However, we show that for many population densities of practical interest in crystallization, accurate estimation should be possible as long as the noise level is not too high.

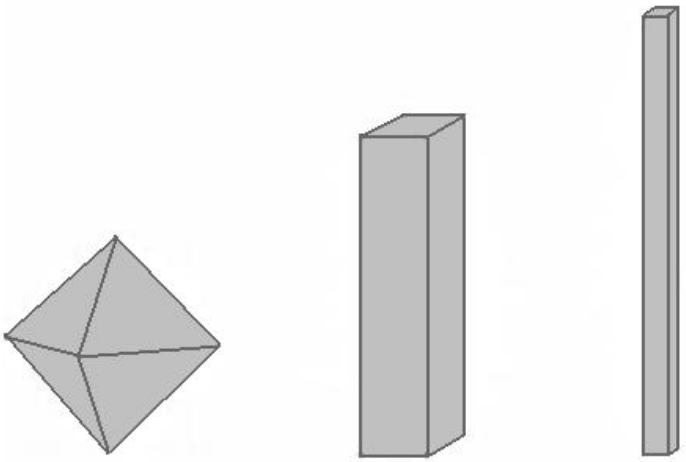

Figure 12. Crystal shapes studied: Octahedral, slab (aspect ratio 1:1:5) and needle (aspect ratio 1:1:20).

4.2 Results

The previously detailed method is tested on several realistic examples in order to evaluate the accuracy of the estimated $\boldsymbol{n}_1$; three crystal morphologies and three distributions representing typical crystallization operations are investigated. Since the relationship defined by Equation (27) is a function of the shape of the crystals, we consider the three non-spherical shapes shown in Figure 12 as being representative of broad classes of crystal categories: bulky, elongated and needle-like. To characterize the size L of each crystal, we use the equivalent spherical diameter, based on the volume of the crystal.

The conversion matrix $\boldsymbol{\Psi}$ was computed for each of the three geometries considered, and the corresponding matrix $\boldsymbol{A}$ was computed according to Equation (29). $\boldsymbol{A}$ is a real symmetric 90 × 90 conversion matrix (m = 90), since our FBRM is set to classify the chord length in 90 channels or bins. The bins are defined by the log scale used by the FBRM, and they are the same for both $\boldsymbol{q}$ and $\boldsymbol{n}_1$. Since $\boldsymbol{\Psi}$ depends on the crystal shape, $\boldsymbol{A}$

is also different for each shape. First, we determine which vectors in the basis have an influence on the chord-length density. The goal is to reduce the space defined by the 90 basis vectors to a smaller invertible subspace. Consequently, the space is divided into two subspaces: an observable one and an unobservable one. The eigenvalues of the matrix $\boldsymbol{A}$ are computed for each of the three geometries, and are plotted in Figure 13.

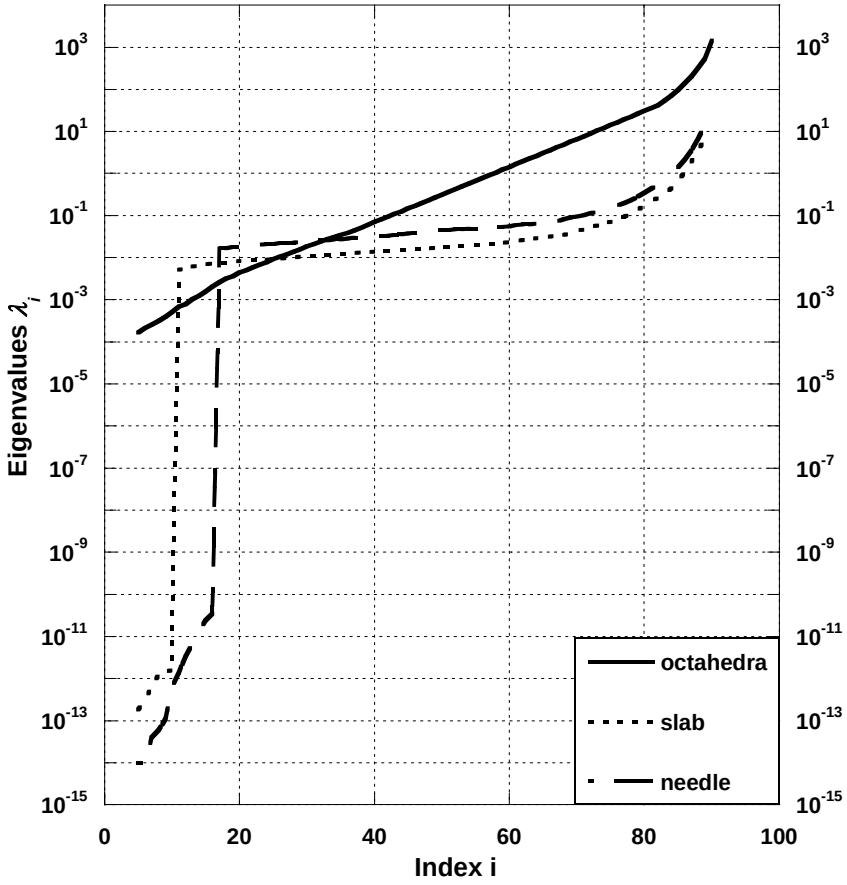

Figure 13. Eigenvalues of *A* for octahedral, slab and needle-like crystals.

For the octahedral crystals, the non-zero eigenvalues (solid curve) span seven orders of magnitude. The first five eigenvalues are identically zero and therefore must be in the unobservable subspace. The challenge, in this case, is to determine a value of $m' > 5$ that enables accurate estimation, especially in the presence of noise. From Equation (15), we can see that features in $\boldsymbol{n}_1$ associated with eigenvalues of $\lambda > 1$ will be amplified in $\boldsymbol{q}$, while eigenvalues of $\lambda < 1$ will attenuate the corresponding features in $\boldsymbol{q}$. For the octahedral crystal, this transition occurs around $m' = 55$.

The eigenvalues of the slab-like geometry are shown by the dotted curve in Figure 2. Most of the eigenvalues range over three orders of magnitude. However, a sharp drop-off exists in which the first 11 eigenvalues are extremely small. Therefore, the cutoff m' should not be set lower than 11 (or else the inversion may amplify noise by a factor of 10^{12}). The needle-like geometry exhibits qualitative behavior that is similar to that of the slab. Most λ's extend over 3 orders of magnitude. The cutoff value m' is limited by the 17 extremely small eigenvalues (dashed curve). For both the slab and the needles, we notice a different distribution of the eigenvalues, compared with the octahedral shape, due to their highly non-spherical geometry.

Although these three shapes exhibit different qualitative features, it is not clear at this point which will be more difficult to invert. The slab and needle have few eigenvalues that are greater than 1, so they may be more likely to amplify noise in the inversion. However, all three shapes have a large number of eigenvalues that are greater than 10^{-2}, so if the original noise level in $\boldsymbol{q}$ is low, then an amplification of 100 may still be acceptable.

In order to evaluate the inversion process, we must also consider the particular crystal size distribution. The population density distributions examined here were chosen because each represents a particular mode of crystallizer operation and resulting product size distribution, i.e.

- Gamma distribution − representative of crystals produced in batch crystallization
- Exponential distribution − representative of crystals produced in continuous crystallization in which anomalous growth, agglomeration, and breakage can be neglected
- Bimodal distribution − representative of complex batch crystallization in which seeding or other phenomena lead to the crystal size distribution having two modes.

We first discuss in detail the results of our analysis of systems in which the crystal population density follows a gamma distribution function. Using the outcome as a point of departure, we then contrast that behavior with results obtained from exponential and bimodal distribution functions. Finally, we impose noise on a hypothetical signal from an FBRM instrument to explore how the interpretation of that signal is affected by the noise. The plots omitted in this chapter for brevity concerns can be found in Appendix A.

4.2.1 Gamma distribution

Gamma distribution functions are defined by:

$$\boldsymbol{n}_1\left(\bar{L}_i\right) = \gamma_2\, \bar{L}_i^{\beta\text{-}1} \frac{e^{-\bar{L}_i/\theta_2}}{(\beta\text{-}1)!\,\theta_2^{\beta}} \tag{45}$$

where β is a shape factor, θ_2 is a scale parameter and γ_2 is a normalizing coefficient. In the present work, the parameters are selected so that L_{mode} = 400 μm (β = 9, θ_2 = 0.5 and γ_2 = 0.01).

4.2.1.1 Octahedral crystals

We first consider octahedral crystals whose length-weighted population density follows a gamma distribution in the limit of no FBRM noise. Following the recommended Analysis and setting ε_{tol} = 0.01, so that the reconstructed $\boldsymbol{n}_1$ will be accurate within 1 %. Therefore, we compute that the cutoff value m' is 65, which lead to λ's ranging over 3 orders of magnitude in the observable subspace. Figure 14 illustrates the good reconstruction of $\boldsymbol{n}_1$ in the observable subspace, according to Equations (40) and (41), such that

$$\boldsymbol{n}_1 = \boldsymbol{n}_{1,obs} + \boldsymbol{n}_{1,unobs} \cong \boldsymbol{n}_{1,obs} \tag{46}$$

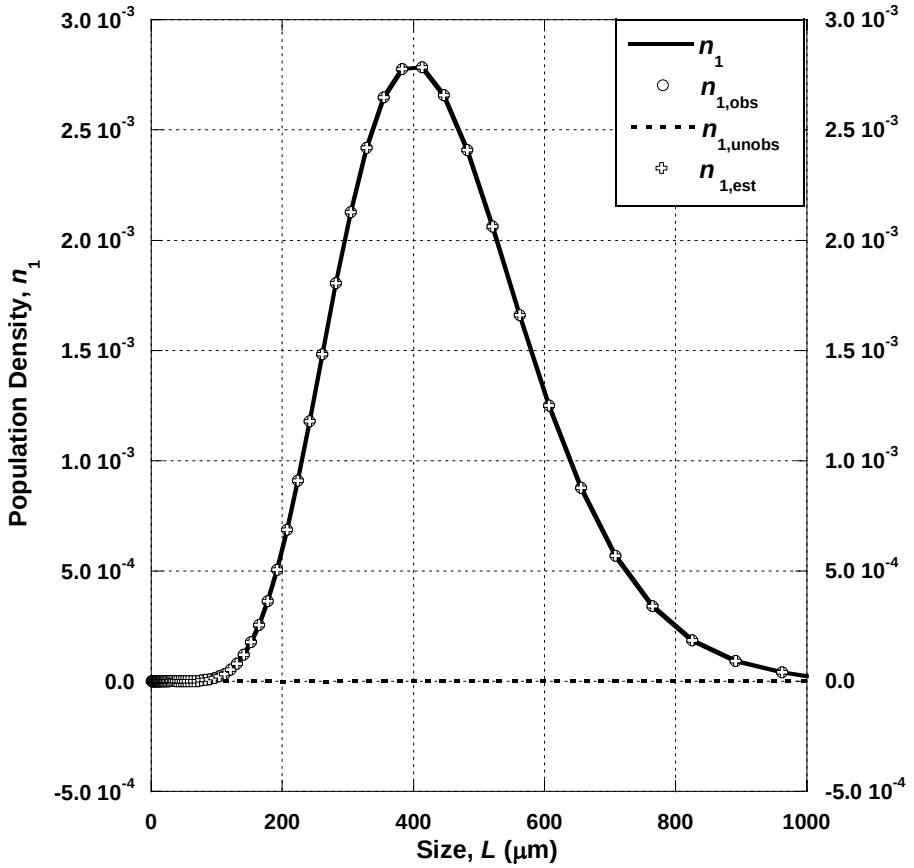

Figure 14. Projection of n_1 onto observable and unobservable subspaces, and recovered population density through the spectral method for an octahedral shape, using $m' = 65$. Similar plots are obtained for slab and needle-like crystals.

Having established a good projection using $m' = 65$, we now focus on the estimation of $\boldsymbol{n}_1$ from a measured chord-length density $\boldsymbol{q}$. Using the gamma distribution in Figure 14 and using Equation (27), we obtain the "measured" $\boldsymbol{q}$. Equation (42) is then used to estimate $\boldsymbol{n}_1$, using only the last 25 (90 – 65) eigenvectors of $\boldsymbol{A}$. An accurate reconstruction of $\boldsymbol{n}_1$ is obtained, as both the initial density $\boldsymbol{n}_1$ (solid curve) and the restored density $\boldsymbol{n}_{1,\text{est}}$ (cross symbols) are in agreement, as shown in Figure 14. As mentioned previously, in the noise-free limit, $\boldsymbol{n}_{1,\text{obs}} = \boldsymbol{n}_{1,\text{est}}$ by definition, which is confirmed by Figure 3. Figure 4 provides further confirmation of the successful inversion. The original chord-length density $\boldsymbol{q}$ (solid curve) coincides with the recovered population density $\boldsymbol{q}_{\text{est}} = \boldsymbol{\Psi}\, \boldsymbol{n}_{1,\text{est}}$ (cross symbols) and with $\boldsymbol{q}_{\text{obs}} = \boldsymbol{\Psi}\, \boldsymbol{n}_{1,\text{obs}}$ (circle symbols). Similarly, $\boldsymbol{q}_{\text{unobs}} = \boldsymbol{\Psi}\, \boldsymbol{n}_{1,\text{unobs}}$ (dashed line) is approximately zero. A slight waviness in $\boldsymbol{q}_{\text{est}}$ can be seen at the smallest sizes — this trend will be seen across the all shapes and distributions we analyze in this paper.

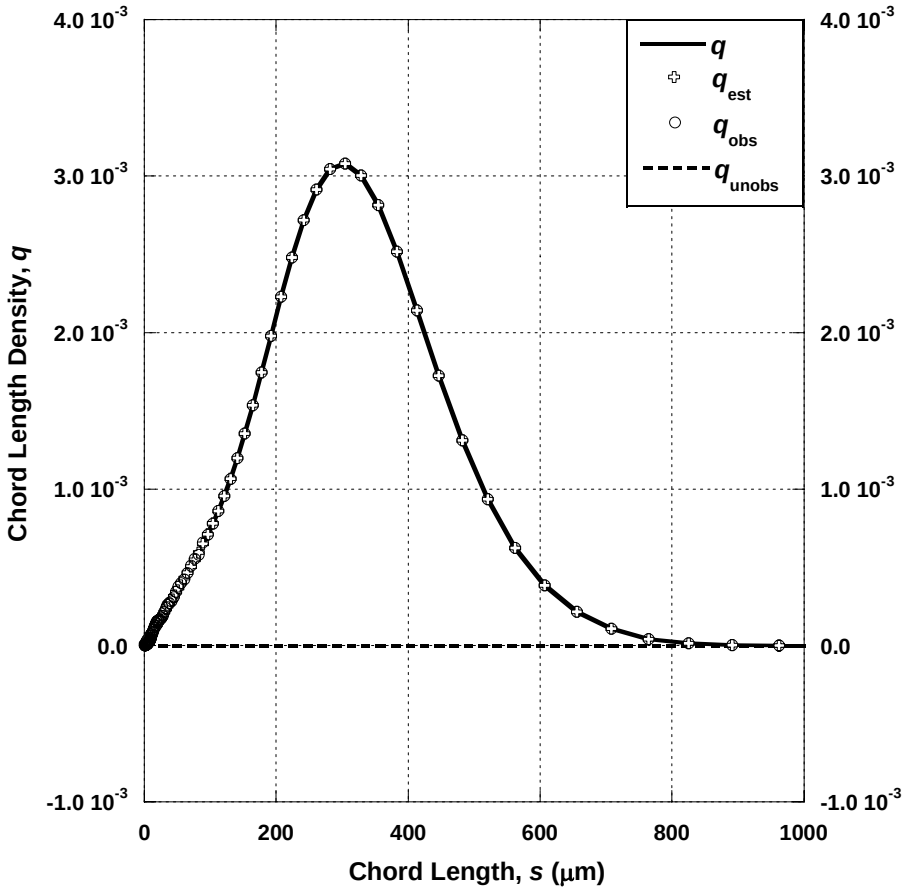

Figure 15. Projection of q onto observable and unobservable subspaces and recovered chord-length density for an octahedral shape, using $m' = 65$. Similar plots are obtained for slab and needle-like crystals.

4.2.1.2 Slab-like crystals (Aspect ratio 1:1:5)

We now consider slab-like crystals with the gamma distribution. As with the octahedral crystals, we set $\varepsilon_{tol} = 0.01$, which results in an eigenvalue cutoff of $m' = 54$. Thus, 36 basis vectors will now be used, compared to 25 for the octahedral crystals. From Figure 2, we see that for the octahedral crystals, $\lambda_{m'+1}$ was slightly greater than 1, while now $\lambda_{m'+1}$ is less than 0.1. Thus, the inversion of the gamma distribution may be slightly more noise-sensitive for the slab. Similar agreement is achieved among the recovered $\boldsymbol{n}_{1,est}$, the projected $\boldsymbol{n}_{1,obs}$, and the initial length-weighted population density $\boldsymbol{n}_1$, as in the octahedral case of Figure 3. Again the projection onto the unobservable subspace is negligible due to our setting of ε_{tol}. Good agreement was also achieved in chord-length density, similar to that plotted in Figure 4 for the octahedral case.

4.2.1.3 Needle-like crystals (Aspect ratio 1:1:20)

For needle-like crystals, the cutoff is again determined by the 1 % precision imposed on the reconstructed $\boldsymbol{n}_1$ by ε_{tol}, resulting in $m' = 37$. Thus, a larger number of eigenvectors is needed for the needle, compared to the slab, although the value of $\lambda_{m'+1}$ is slightly greater than for the slab. Due to the similar characteristics of their eigenvalue spectrum, we expect similar inversion properties for the needle and slab, and this should be true with and without noise. The projections of $\boldsymbol{n}_1$ and their corresponding $\boldsymbol{q}$ all lead to good reconstructions, with results again similar to those pictured in Figures 3 and 4. Additional figures showing the evolution for slab and needle like crystals are available in Appendix A. The results for the gamma distribution for all three shapes are summarized in Table 1.

4.2.2 Exponential distribution

A key difference between exponential and gamma distributions, is that the former has larger number of small crystals. A nucleation event is indicated by an increase in the number of small crystals, which is a common disturbance in crystallization, and thus it is important to be able to estimate accurately the population of small crystals.

4.2.2.1 Octahedral crystals

As with the gamma distribution, we specify $\varepsilon_{tol} = 0.01$. However, with the exponential distribution, $m' = 32$ is now required to achieve an accurate reconstruction, compared to $m' = 65$ for the gamma distribution. This comparison can also be seen in Table 1. The eigenvalues required for this value of $m' = 32$ now span almost 5 orders of magnitude, which can be seen in Figure 2 and also in Table 1. Figure 5 illustrates the projection of $\boldsymbol{n}_1$ onto the observable and unobservable subspaces. A 1 % error was allowed in the projection, and it is visible in Figure 5 at the smallest sizes, suggesting that the recovery may be most challenging there.

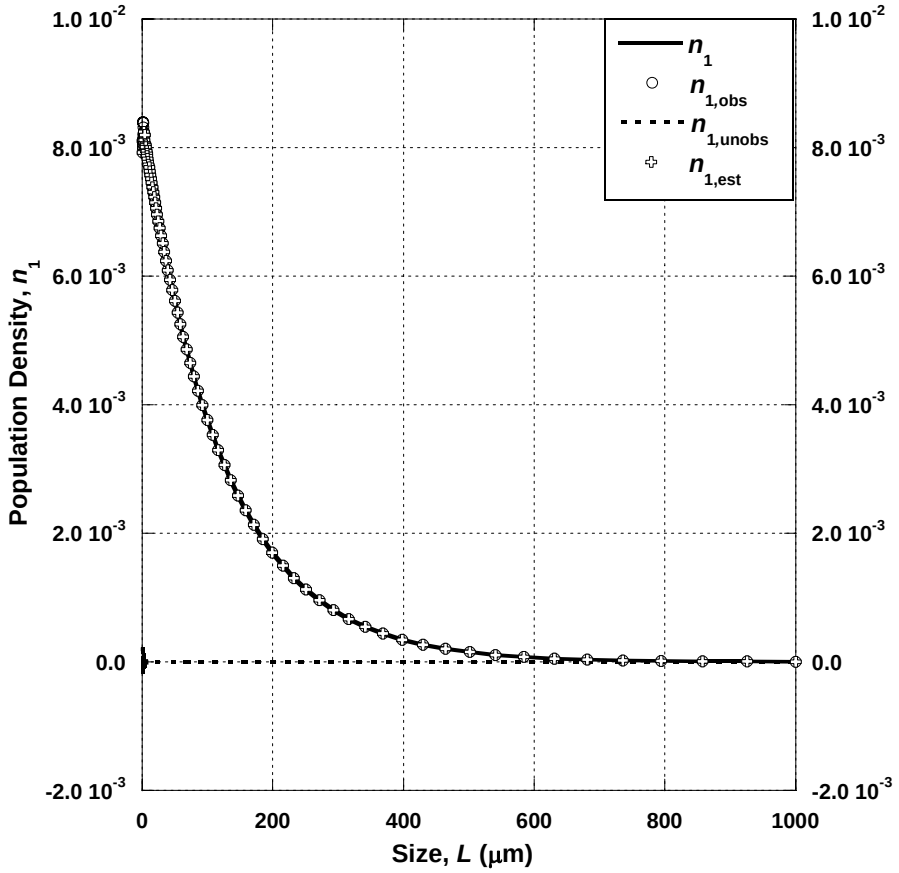

Figure 16. Projection of n_1 from an exponential distribution onto the observable and unobservable subspaces, and recovered population density through the spectral method for an octahedral shape, using , using $m' = 32$.

4.2.2.2 Slab-like crystals (Aspect ratio 1:1:5)

Figure 6 shows the exponential distribution for the slab-like crystals. Recall that the minimum value of m' is 11 for this crystal shape, due to the 11 near-zero eigenvalues in Figure 2. With this constraint, we are now not able to achieve $\varepsilon_{tol} = 0.01$, and by setting $m' = 11$ we achieve an error of 14.2 % ($\varepsilon_{tol} = 0.142$). Figure 6 illustrates the resulting error when $\boldsymbol{n}_1$ is projected onto the observable subspace. In fact, the error is concentrated at the lowest sizes, and the reconstruction is quite accurate over the majority of the sizes. Note that the error defined by Equation (21) does not take into account the width of each bin, and that the bins are logarithmically distributed such that the bins at the smallest sizes have the smallest width. This causes the small crystals to dominate our error calculation. In any case, we use this measure of error in part because it may be desirable to estimate these smallest bins accurately so as to monitor nucleation events. Of the eigenvectors that are retained for the observable space, the range of eigenvalues is only 3 orders of magnitude. Thus, these are easily invertible in the noise-free case considered here, and Figure 6 shows that $\boldsymbol{n}_{1,obs}$ and $\boldsymbol{n}_{1,est}$ are virtually identical.

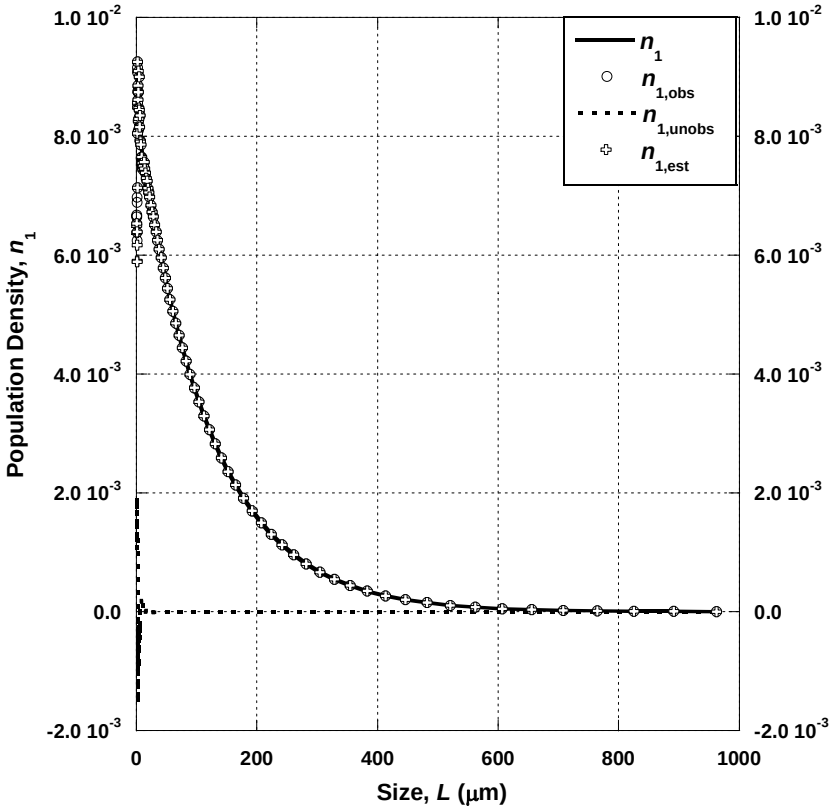

Figure 17. Projection of exponential distribution n_1 onto the observable and unobservable subspaces, and recovered population density through the spectral method for a slab shape, using $m' = 11$.

4.2.2.3 Needle-like crystals (Aspect ratio 1:1:20):

The results for the needle-like crystals are similar to those of the slab. Due to the near-zero eigenvalues, the minimum value of m' is 17, and this cutoff yields a projection error of 30.8 %. Oscillations for the lower sizes are, as shown in Figure 7, even more noticeable due to the highly non-spherical shape of the crystals, and the accuracy of the restoration of the fines population (below 50 μm) is poor. However, the reconstruction for crystals larger than 50 μm is good.

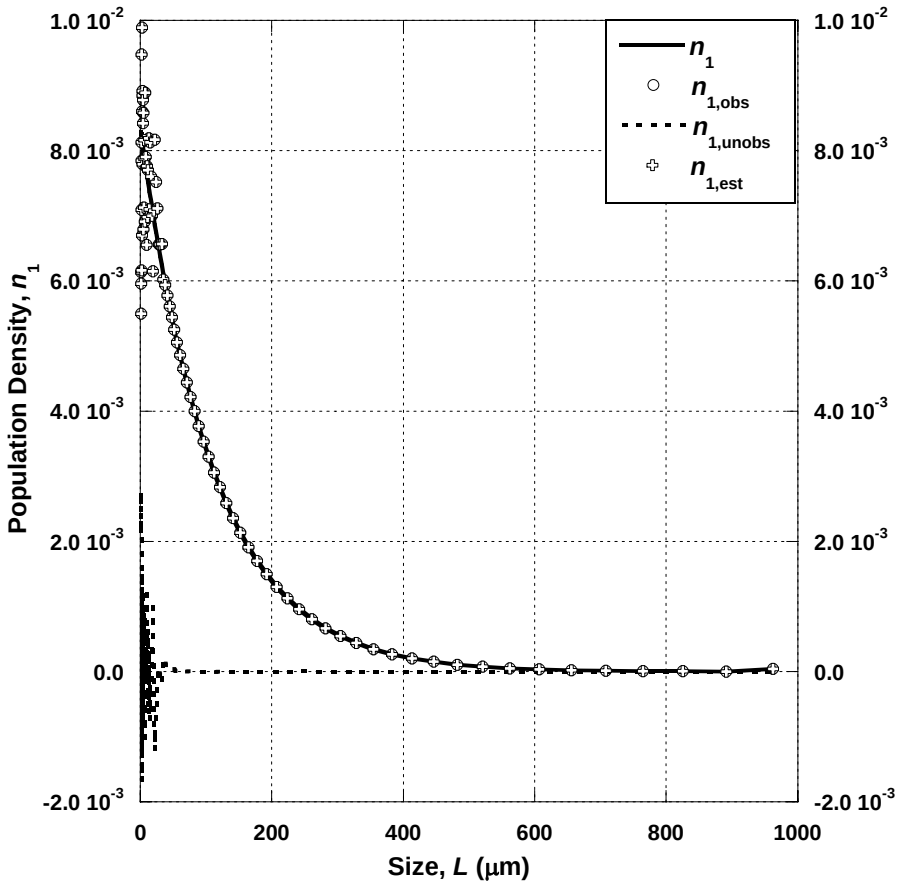

Figure 18. Projection of exponential distribution n_1 onto the observable and unobservable subspaces, and the recovered population density through the spectral method for a needle shape, using $m' = 17$.

Compared to the gamma distribution, the inversion of the exponential distribution is more challenging. Due to the large number of crystals at the smallest sizes, and the small bin sizes at the smallest crystal sizes, it is difficult to estimate the fines distribution accurately, particularly for the slab-like and needle-like crystals.

4.2.3 Bimodal distribution

Bimodal distributions can present significant challenges in analysis and modeling, and so we examine how our methodology handles such systems. The same crystal shapes are considered, and the same estimation procedure is employed. The bimodal distribution is constructed from two gamma distributions, and estimates are achieved at 1 % error for all crystal shapes. This comparison can be seen in Table 1. Figures showing the evolution for slab and needle like crystals are available in Appendix A.

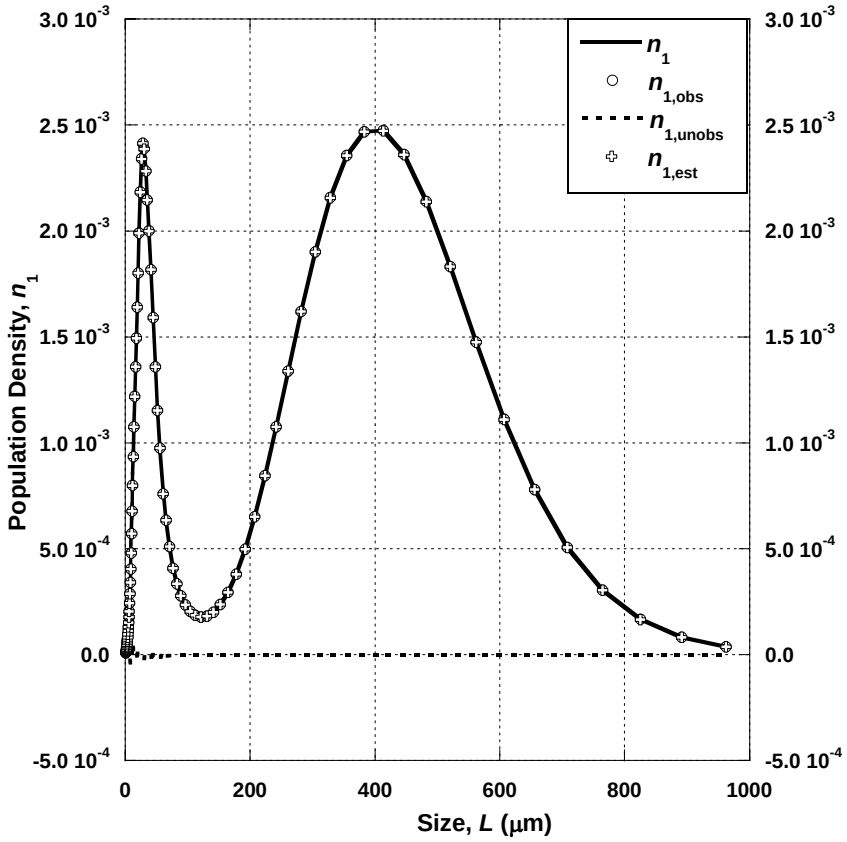

Figure 19. Projection of bimodal n_1 onto the observable and unobservable subspaces, and the recovered population density through the spectral method for an octahedral shape, using $m' = 57$. Similar plots are obtained for the slab and needle-like crystals.

Figure 19 shows the projection and reconstruction for the octahedral crystals. Good reconstruction is seen, although there is a slight but visible component in the unobservable subspace at the smallest sizes. Results similar to those with the gamma distribution are seen for the slab-like and needle-like crystals. The plots are not shown here, but the results are summarized in Table 1. Compared to the gamma distribution, more eigenvectors are required to achieve the 1 % accuracy in the projection, but the corresponding ranges of the eigenvalue magnitudes in the observable subspace have not increased significantly (compared to gamma), indicating that the estimation of $\boldsymbol{n}_1$ in the observable subspace will not be particularly difficult or sensitive to noise.

Table 3. Partition of the space and estimation error for the nine different cases.

		Gamma	Exponential	Bimodal
Octahedral	m'	65	32	57
	$\lambda_{max}/\lambda_{m'}$	473.4	69279	1185.4
	Error	1 %	1 %	1 %
Slab	m'	54	11	21
	$\lambda_{max}/\lambda_{m'}$	528.0	1997.5	1233.0
	Error	1 %	14.2 %	1 %
Needle	m'	37	17	18
	$\lambda_{max}/\lambda_{m'}$	589.5	1354.7	1345.3
	Error	1 %	30.8 %	1 %

4.2.4 Influence of noise

In the noise-free case, the spectral method provides good estimates of $\boldsymbol{n}_1$ for the gamma and bimodal distributions for all three crystal shapes considered. When the exponential distribution is analyzed, the estimation is good except at the smallest crystal sizes, in which case the estimates are highly oscillatory around the actual mean. However, real

CLD measurements are noisy, making estimation of the population density more difficult, and this will be especially true for the basis vectors with small λ.

To investigate the role of noise, we measure the steady-state noise in each channel, using our FBRM measurements obtained for paracetamol crystallization from ethanol [1]. We estimate the standard deviation vector $\boldsymbol{\sigma}$ of the FBRM signal for each bin of $\boldsymbol{q}$, and then add this noise to the noise-free $\boldsymbol{q}$ computed for each of our three distributions. Because the experiments and associated noise are for octahedral crystals, we analyze that shape only. In general, the noise may also depend on the crystallization time and other details of the process, and our steady-state noise levels are only intended to explore the effect of noise in the FBRM measurements. The noise level also depends on the integration time of the FBRM measurement, and we consider measurement time increments of 10 s, 20 s and 30 s. Increasing this time step increases the number of counts in each bin and therefore decreases the noise level.

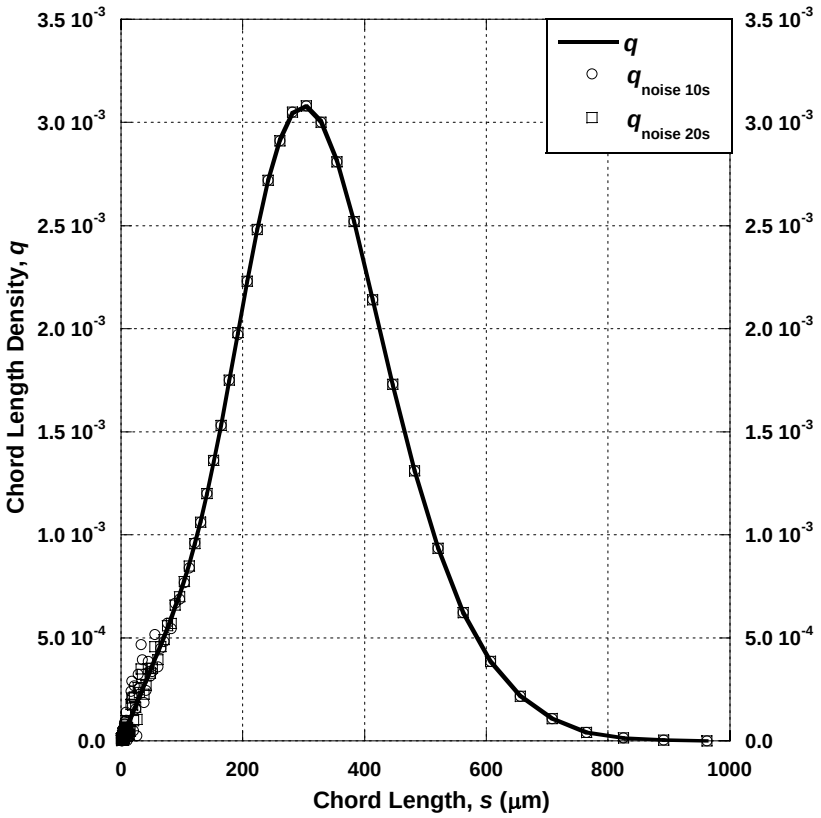

Figure 20. Addition of noise to the *q* computed for the gamma distribution.

To obtain insight on the influence of noise on the recovery process, a zero-mean Gaussian-distributed noise vector $\boldsymbol{v}$ is added to the initial $\boldsymbol{q}$ (Figure 20). Notice that the highest noise appears in the smallest bins, further complicating the estimation. The recovery of the population through the spectral method gives mixed results, shown in Figure 21. The recovered population density displays oscillations up to 200 μm for a sampling time of 10 s (circle symbols), but the estimation is greatly improved when the sampling time is increased to 20 s. The results are shown in Table 4., with the definition

$$e_{\max}\left(\boldsymbol{n}_1\right) = \max_i \left(\boldsymbol{n}_{1,est,i} - \boldsymbol{n}_{1,i}\right) \tag{47}$$

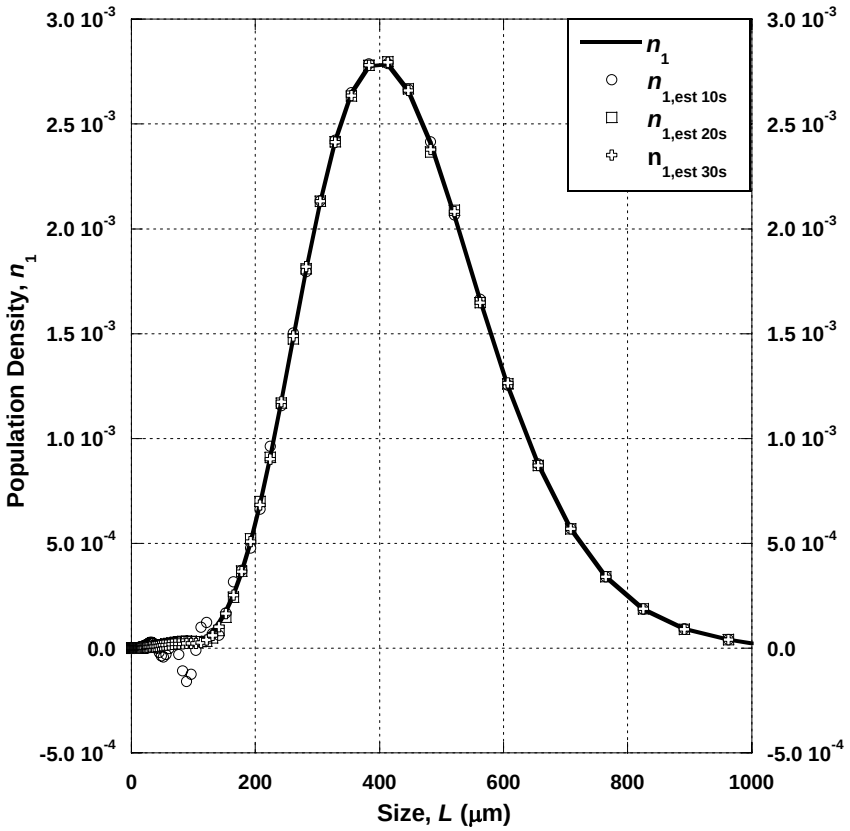

Figure 21. Restoration of the gamma population density from a noisy chord-length density, using $m' = 65$.

Note that the same value of m′ = 65 from the noise-free study is used here. Earlier in the paper we suggested the guideline of $\lambda_{max}/\lambda_{m'+1}$ to predict the error in n1 due to noise. We see in Table 2 that our guideline is consistent with these results. If we consider even longer sampling times than 30 s for the gamma distribution, the error in $\boldsymbol{n}_1$ will flatten out and be dominated by the 1 % reconstruction error from the unobservable subspace, while $\sigma_{max}/\lambda_{m'+1}$ will continue to decrease as the sampling time increases. Thus no benefit will be achieved with longer sampling times.

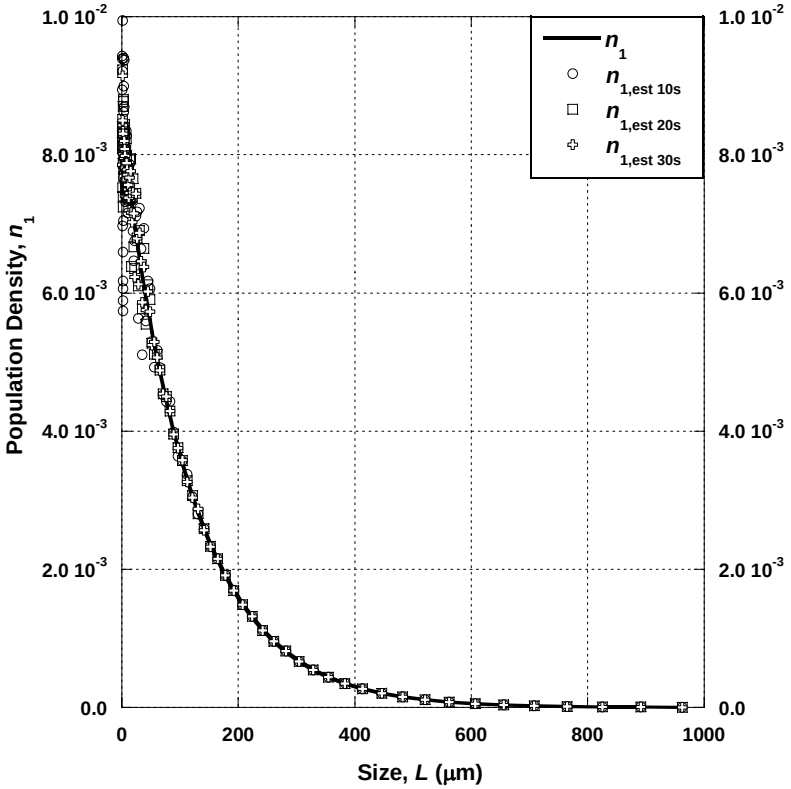

Figure 22. Restoration of the exponential population density from a noisy chord-length density, using $m' = 32$.

When the exponential distribution is considered, an average acquisition time of 20 s is no longer sufficient to reduce the noise level to an acceptable one (Figure 22). A sampling time of 30 s (cross symbol) is now required for good estimation. Once again, the error is mainly due to the inaccuracy of the estimation of the fines population. As in the noise-free case, the bimodal distribution is more difficult to estimate than gamma, but is easier than exponential.

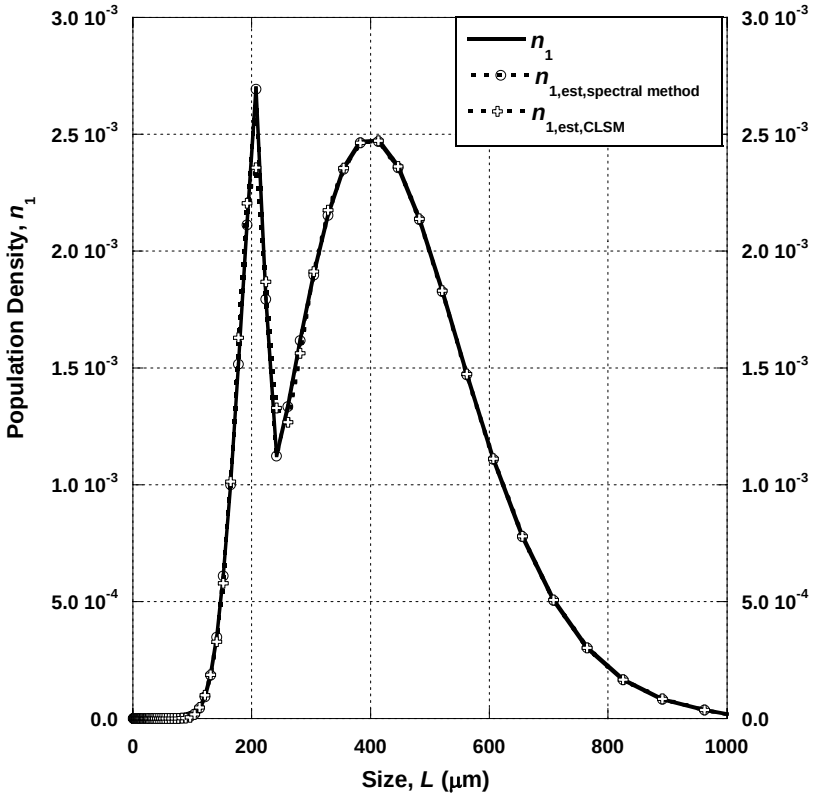

Figure 23. Comparison of the spectral method to CLSM, for a noise based on a measurement every 20s, for the bimodal distribution.

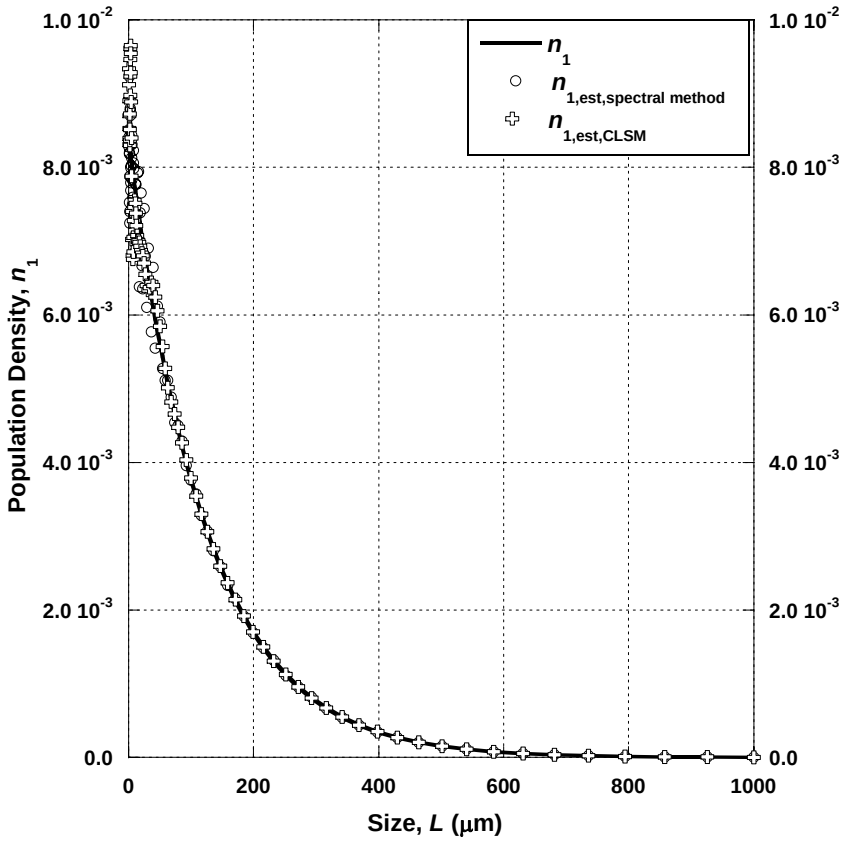

Figure 24. Comparison of the spectral method to CLSM, for a noise based on a measurement every 20s, for the exponential distribution.

A comparison between the previously detailed method and the CLSM method described by Ruf et al. (Ruf et al. 2000) is shown for the bimodal distribution in Figure 23 and for the exponential one in Figure 24. The CLSM method provides better results for the exponential distribution as it imposes smoothing of the distribution, whereas our method performs better at restoring sharp features of the population density, which are smoothed out by the CLSM. In practice, the best approach may be to combine our approach with additional smoothing, when deemed appropriate (i.e. exponential distributions).

Table 4.Estimation errors for octahedral crystals when measurement noise is added (averaged over 100 runs).

		Gamma	Exponential	Bimodal
10 s	$\sigma_{max}(\boldsymbol{q})$	3.59×10^{-4}	3.59×10^{-4}	3.59×10^{-4}
	$\lambda_{m'}$	3.57	0.28	1.05
	$\sigma_{max}(\boldsymbol{q})/\lambda_{m'}$	1.00×10^{-4}	1.30×10^{-3}	3.42×10^{-4}
	$e_{max}(\boldsymbol{n}_1)$	1.16×10^{-4}	1.54×10^{-3}	3.23×10^{-4}
	Error	2.52 %	10.32 %	6.42 %
20 s	$\sigma_{max}(\boldsymbol{q})$	1.80×10^{-4}	1.80×10^{-4}	1.80×10^{-4}
	$\lambda_{m'}$	3.57	0.28	1.05
	$\sigma_{max}(\boldsymbol{q})/\lambda_{m'}$	5.04×10^{-5}	6.52×10^{-4}	1.71×10^{-4}
	$e_{max}(\boldsymbol{n}_1)$	4.89×10^{-5}	6.71×10^{-4}	1.87×10^{-4}
	Error	1.21%	4.82 %	2.71 %
30 s	$\sigma_{max}(\boldsymbol{q})$	8.98×10^{-5}	8.98×10^{-5}	8.98×10^{-5}
	$\lambda_{m'}$	3.57	0.28	1.05
	$\sigma_{max}(\boldsymbol{q})/\lambda_{m'}$	2.52×10^{-5}	3.26×10^{-4}	8.55×10^{-5}
	$e_{max}(\boldsymbol{n}_1)$	2.81×10^{-5}	3.56×10^{-4}	8.69×10^{-5}
	Error	0.81 %	1.05 %	0.91 %

To summarize the main points of this chapter, the FBRM is a useful tool in monitoring the progression of chord-length densities in batch crystallization. The methodology demonstrated here offers an accurate, constraint-free restoration of the population density, which can be obtained from FBRM measurements. The spectral method can be

efficiently applied to a wide range of non-spherical particle shapes, as well as multimodal and sharp population density functions.

The principal component analysis offers a straightforward, constraint-free and timely alternative to restore the population density accurately from chord-length density data. It also provides an analysis of which aspects of the population density can accurately be restored. The size of the observable subspace is a function of the crystal geometry and the precision desired. Note that as the geometry becomes more elongated, a drop in the eigenvalues is seen which defines the limits of the accuracy of the recovery process, as it sets a limit to the size of both observable and non-observable subspace and the accuracy of the recovery. As the needles get thinner, the size of the unobservable subspace increases and the restoration of the population density for the lower size ranges are more challenging. The accuracy of the proposed method is therefore limited by the geometry of the considered population. The projections onto the observable and unobservable subspaces tend to be highly oscillatory in small sizes range. Those features are more difficult to estimate because all crystal sizes contribute to small chords while only larger ones create large chords. Note that extreme oscillations can occur in the smaller bins sizes during the restoration and also that the smaller bins are more sensitive to noise, thus making it harder to effectively estimate those populations. A smoothing can still be applied later to the restored density if needed.

Estimation is limited by the noise in measurements of the chord-length density, which can be reduced by increasing the data acquisition time frame. The data presented here shows that any time frame above 30 s will suffice to reduce the noise to an acceptable level for the octahedral crystal shape. Also, it was shown that, when compared to CLSM,

the spectral method provides a better restoration of population densities with sharp features. Although our method provides an alternative method for estimating population density, its greater contribution may be for the analysis; specifically, the analysis can help tailor the FBRM settings of number of bins, size distribution of bins, and integration time, for the particular crystal shape and distribution function appropriate to a particular process. Furthermore, the presented methodology has great potential to be the basis for a control scheme that manipulates the population density produced from FBRM raw data.

CHAPTER 5

ESTIMATING SUPERSATURATION, NUCLEATION AND GROWTH KINETICS

Being able to observe on-line and in real-time the evolution of the population density constitutes a major asset in understanding crystallizer operation as well as the phenomena that influence product quality. This observation leads to another important advantage, namely the ability to compute the supersaturation and derive the kinetics of the system. Considering that a critical step towards better control of a crystallization process is the estimation of the system nucleation and growth kinetics (Hornedo 1999, Liu 2004), the ability to derive such valuable information from FBRM data is useful. Moreover, the nucleation and growth kinetics are involved in the resolution of the population balance and thus influence the final crystal size distribution (Mullin 2001, Randolph 1971). Such abilities provide the user with the necessary tools for developing a predictive model and implementing efficient control.

Empirical methods have, thus far, helped gain qualitative information on growth and nucleation phenomena. A number of analytical techniques, combined with an appropriate model, are available to monitor the evolution of the crystallization process. Typically, nucleation kinetics are estimated from measurements of either transient or steady state crystal size distributions, induction times, or metastable zone width. Estimates are then correlated with process variables such as supersaturation (Kashiev 2003). A wider range of methods are available for estimates of growth kinetics. These

measure the supersaturation of the solution and relate it to the growth rate, as described in Chapter 2.

In this chapter, we will explore the possibility of estimating in-situ, and in real time the solute concentration from FBRM data. The method links the measured CLD to the supersaturation, thus enabling its estimation. This in turn enables the estimation of the kinetics of the system, namely growth and primary nucleation kinetics. The batch cooling crystallization of paracetamol in ethanol solutions will continue to be used as a model system.

The chapter is organized as follows: in the first section the monitoring of the supersaturation is considered. Then, the monitoring of the evolution of the driving force is used to determine the system kinetics for both growth and primary nucleation. Finally, this procedure is applied to experimental data, and the kinetics of the paracetamol-ethanol system are determined. Once the growth kinetics are known, they can be used in solving the population balance model to compute the crystal size distribution, which is the subject of Chapter 6.

5.1 Methodology

There are two key phenomena in crystallization, nucleation and growth, both of which are functions of supersaturation and temperature. First, we develop a model that enables us to estimate the supersaturation as a function of time via the use of the CLD data. Then this knowledge is used to establish the growth and the nucleation kinetics of the system.

5.1.1 Estimation of number size population

As seen in Chapter 3, the relationship between the length-weighted population density, $\boldsymbol{n}_1$, and the chord-length density, $\boldsymbol{q}$, is defined by

$$\boldsymbol{q} = \boldsymbol{\Psi}\boldsymbol{n}_1, \tag{48}$$

where $\boldsymbol{\Psi}$ is a conversion matrix relating the two vectors, $\boldsymbol{n}_1$ and $\boldsymbol{q}$, which describe the densities. The methodology described in the previous chapters is used here to calculate $\boldsymbol{n}_1$ through FBRM measurements. The density $\boldsymbol{n}_1$ is normalized and therefore in order to also compute $\Delta\boldsymbol{N}$, which is the number of crystals in a defined size range. A scaling factor has to be taken into consideration, which is the total number of counts, N_T. This is also measured by the FBRM.

It is assumed that the total number of chord counts, N_S, is related to the total number of crystals, N_T, through the ratio between the scanned volume, V_S, and the total volume of the slurry, V_T, according to the following equations:

$$V_S = \dot{v}_S \, \delta \, \varepsilon \, \Delta t \tag{49}$$

$$N_T = \frac{N_S}{V_S} V_T \tag{50}$$

where δ is the depth scanned by the laser (estimated to be 1.50×10^{-3} m), ε is the width scanned by the laser (estimated to be 5.80×10^{-6} m), $\dot{v}_s$ is the scanning speed (2 m/s) and Δt is the acquisition time frame. We made the assumptions of no shadowing or masking effect (Barthe 2006, Mendez 2004).

Therefore $\Delta\boldsymbol{N}$ can be computed from FBRM measurements.

$$\Delta \boldsymbol{N}\left(\bar{L}_i\right)=\frac{\boldsymbol{n}_1\left(\bar{L}_i\right)\left(L_{i+1}-L_i\right)}{\bar{L}_i\left(\sum_{j=1}^{N_b}\frac{\boldsymbol{n}_1\left(\bar{L}_j\right)\left(L_{j+1}-L_j\right)}{\bar{L}_j}\right)}N_T \tag{51}$$

5.1.2 Estimation of supersaturation

Supersaturation is the driving force upon which nucleation and growth kinetics depend. It is therefore a crucial variable to estimate. It is defined by:

$$\Delta C = C - C^* \tag{52}$$

where C is the concentration (kg solute/kg solvent) and C^* is the solubility (kg solute/kg solvent). The solubility, C^*, of paracetamol in ethanol solution has previously been determined (Gracin 2002), and its dependence on temperature T (K) is given by

$$C^*\left(T\right)=2.955\times10^{-4}\ \exp\left(2.179\times10^{-2}\,T\right) \tag{53}$$

Since the solution temperature is a function of time, the evolution of the solubility is also a function of time. When the temperature is ramped down, the time-dependence of the temperature is given by the dimensionally consistent equation:

$$T\left(t\right)=T_0-r\,t \tag{54}$$

where r is the cooling rate , T_0 is the initial temperature.

The concentration of the solute in solution, C, in mass of solute/ mass of solvent is defined as:

$$C=\frac{m_{\text{solute in solution}}}{M_{\text{solvent}}}=\frac{m_{\text{initial}}-m_{\text{c,crystallized}}}{M_{\text{solvent}}} \tag{55}$$

$$m_{\text{c,crystallized}}=\sum_{i=1}^{N_b}\Delta \boldsymbol{N_i}\left(\bar{L}_i\right)\bar{m}_{i,\text{one crystal}}=\rho\sum_{i=1}^{N_b}\Delta \boldsymbol{N_i}\left(\bar{L}_i\right)\bar{V}_{i,\text{one crystal}} \tag{56}$$

where N_b is the number of bins, ρ is the density (e.g. for paracetamol $\rho = 1.293\times10^3$ kg/m^3, Granberg 2005) , $M_{solvent}$ the mass of solvent in kg, $m_{initial}$ the mass of solute introduced in the system in kg, $m_{c,crystallized}$ the mass of solute crystallized in kg and $\Delta \boldsymbol{N_i}$ is the total number of crystals of characteristic size $\bar{L}_i$ in the crystallizer. The characteristic size is here defined as the equivalent diameter: that is, the diameter of a sphere having the same volume as the crystal. The number size population, $\Delta \boldsymbol{N}$, is related to the population density, $\boldsymbol{n}_1$, via Equation (51).

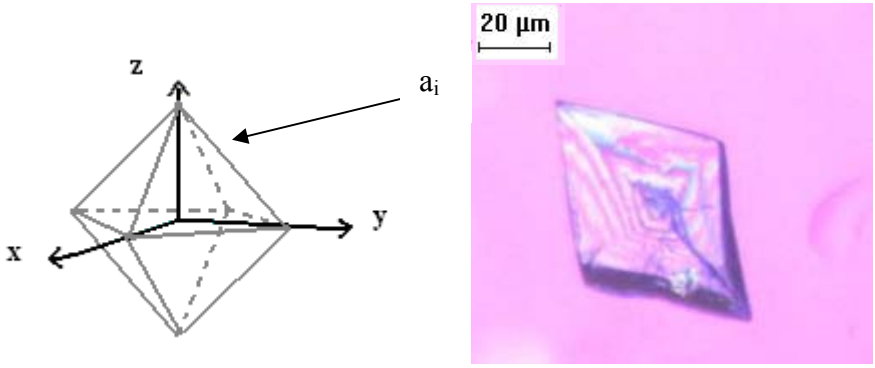

Figure 25. Octahedral crystal (left: scheme – right: micrograph of actual crystal)

The relationships between the measured crystal dimension and area and volume of the crystals are required for this analysis. For example, paracetamol crystals are assumed to be octahedral as shown in Figure 25, so that the characteristic length $\bar{L}_i$, which is the equivalent diameter, is related to the edge a_i according to the relationship

$$a_i = \sqrt[3]{\frac{\pi}{2\sqrt{2}}}\bar{L}_i = \frac{\sqrt[3]{\pi}}{\sqrt{2}}\bar{L}_i \qquad (57)$$

Therefore the area and the volume of the octahedral can be expressed in term of $\overline{L}_i$, and the result substituted into an expression that can be used to estimate solute concentration:

Area of one octahedron crystal of size $\overline{L}_i$:

$$\overline{A}_{i,\text{one crystal}} = 2\sqrt{3}\, a_i^{\,2} = \sqrt{3}\left(\sqrt[3]{\pi}\,\overline{L}_i\right)^2 \tag{58}$$

Volume of one octahedron crystal of size $\overline{L}_i$:

$$\overline{V}_{i,\text{one crystal}} = \frac{\sqrt{2}}{3} a_i^{\,3} = \frac{4\pi}{3}\left(\frac{\overline{L}_i}{2}\right)^3 = \frac{\pi}{6}\overline{L}_i^{\,3} \tag{59}$$

Therefore,

$$m_{\text{c,crystallized}} = \rho \sum_{i=1}^{90} \Delta \boldsymbol{N}_i\left(\overline{L}_i\right)\overline{V}_{i,\text{one crystal}} = \frac{\pi}{6}\rho \sum_{i=1}^{90} \Delta \boldsymbol{N}_i\left(\overline{L}_i\right)\overline{L}_i^{\,3} \tag{60}$$

The concentration, C, is thus expressed as a function of $\Delta \boldsymbol{N}$.

$$C = \frac{m_{\text{solute in solution}}}{M_{\text{solvent}}} = \frac{m_{\text{initial}} - \rho\dfrac{\pi}{6}\displaystyle\sum_{i=1}^{90} \Delta \boldsymbol{N}_i\left(\overline{L}_i\right)\overline{L}_i^{\,3}}{M_{\text{solvent}}} \tag{61}$$

The initial mass, m_{initial}, and the mass of the solvent, M_{solvent}, are known.

5.1.3 Estimation of growth kinetics:

The supersaturation is related to the kinetics of the system, and its determination enables us to estimate the growth kinetics. A solute mass balance (Mullin 2001, Randolph 1971) gives:

$$-\frac{dC}{dt} = \frac{A_{\text{c,tot}}}{M_{\text{solvent}}} G + \frac{R_{\text{b}}}{M_{\text{solvent}}} \tag{62}$$

where $A_{c,tot}$ is the total surface area, R_b the nucleation rate, G the growth kinetics.

The experiment was designed to provide a period during which only growth occurred with cooling (see Section 6.2). Accordingly, during that period Equation (62) can be simplified by assuming that nucleation is negligible

$$A_{c,tot}\, G \gg R_b \tag{63}$$

A model commonly found in the literature to define G is:

$$G = k_g\, \Delta C^{\,g} \tag{64}$$

so that

$$-\frac{dC}{dt} = k_g\, \frac{A_{c,tot}}{M_{solvent}}\, \Delta C^{\,g} \tag{65}$$

This assumption of negligible nucleation is assessed in the experiments using N_T. As the number of counts does not increase, which means there are no new crystals being formed, and we witness only the growth of the present crystals.

In order to evaluate k_g and g, and to establish an expression for the growth kinetics, the evolution of C vs. time and the crystal surface area must be known. The total surface area, $A_{c,tot}$, which is a function of $\Delta \boldsymbol{N}$ and $\overline{L}_i$, is determined according to the following equation:

$$A_{c,tot} = \sum_{i=1}^{90} \Delta \boldsymbol{N}_i \left(\overline{L}_i\right) \overline{A}_{i,\text{one crystal}} = \sqrt{3}\left(\sqrt[3]{\pi}\right)^2 \sum_{i=1}^{90} \Delta \boldsymbol{N}_i \left(\overline{L}_i\right) \overline{L}_i^2 \tag{66}$$

Therefore, the evolution of the concentration, C, can be estimated from measurements of the chord-length density. The data time frame acquisition was set here such that measurements were taken every 10 s. Since such measurements have significant

noise, the distributions generated are noisy and need to be smoothed. Exponential filters are commonly used for noise reduction in the field of process control and are defined by (Lyons 2004)

$$y_i = \theta_1 x_i + (1-\theta_1) y_{i-1} \tag{67}$$

where y is the filtered signal, x is the input signal and θ_1 relates to the degree of smoothing. Usually $0 < \theta_1 < 1$; the smaller θ_1, the greater the smoothing. Here, a value of $\theta_1 = 0.5$ was adopted as it provides accurate smoothing without influencing the main features. The estimated concentration is therefore smoothed according to that filter in order to reduce the noise level. The supersaturation can thus be monitored through CLD measurements.

By taking the logarithm of Equation (65), we obtain a linear equation involving g and k_g

$$\ln\left(-\frac{dC}{dt}\right) = \ln\left(k_g\right) + \ln\left(\frac{A_{c,tot}}{M_{solvent}}\right) + g\ln\left(\Delta C\right) \tag{68}$$

The values of g and k_g can be obtained from a plot of $\ln\left(-\frac{dC}{dt}\frac{M_{solvent}}{A_{c,tot}}\right)$ vs. $\ln\left(\Delta C\right)$.

The slope is g and the intercept is k_g. Thus, the full growth kinetic expression can be estimated. Here we assume that k_g is independent of T over the range of temperature used in the experiments.

5.1.4 Estimation of nucleation kinetics

The nucleation rate, R_b (kg·s^{-1}), is modeled as follows (Granberg 1999):

$$R_b = k_b \exp\left(\frac{-16\pi\gamma^3\left(M/\rho\right)^2}{3k^3T^3\ln^2\left(C/C^*\right)}\right) \tag{69}$$

where γ is the surface energy, M the molecular mass (e.g. for paracetamol, 151.16 $\times 10^{-3}$ kg·mol^{-1}), ρ the density, k the boltzman constant (1.38×10^{-23} J·K^{-1}), T the temperature (K), C the concentration (kg solute/ kg solvent), $C^*(T)$ the solubility (kg solute/ kg solvent) and k_b is a nucleation constant.

The interfacial tension is expressed through (Mersmann 1990)

$$\gamma = 0.414kT\left(\frac{\rho}{M}N_A\right)^{2/3}\ln\left(\frac{C_s}{C^*}\right) \tag{70}$$

where N_A is Avogadro's constant (6.02×10^{23} mol^{-1}), M is the molecular mass, and C_s is concentration of solute in the solid phase. The evolution of the mass can be evaluated as seen in the previous section (Equation (60)). Thus, the only parameter to fit in Equation (62), when R_b is replaced by its expression, is k_b. The system kinetics can then be fully determined by the values of k_b, k_g and g. The procedure is summarized in Figure 26.

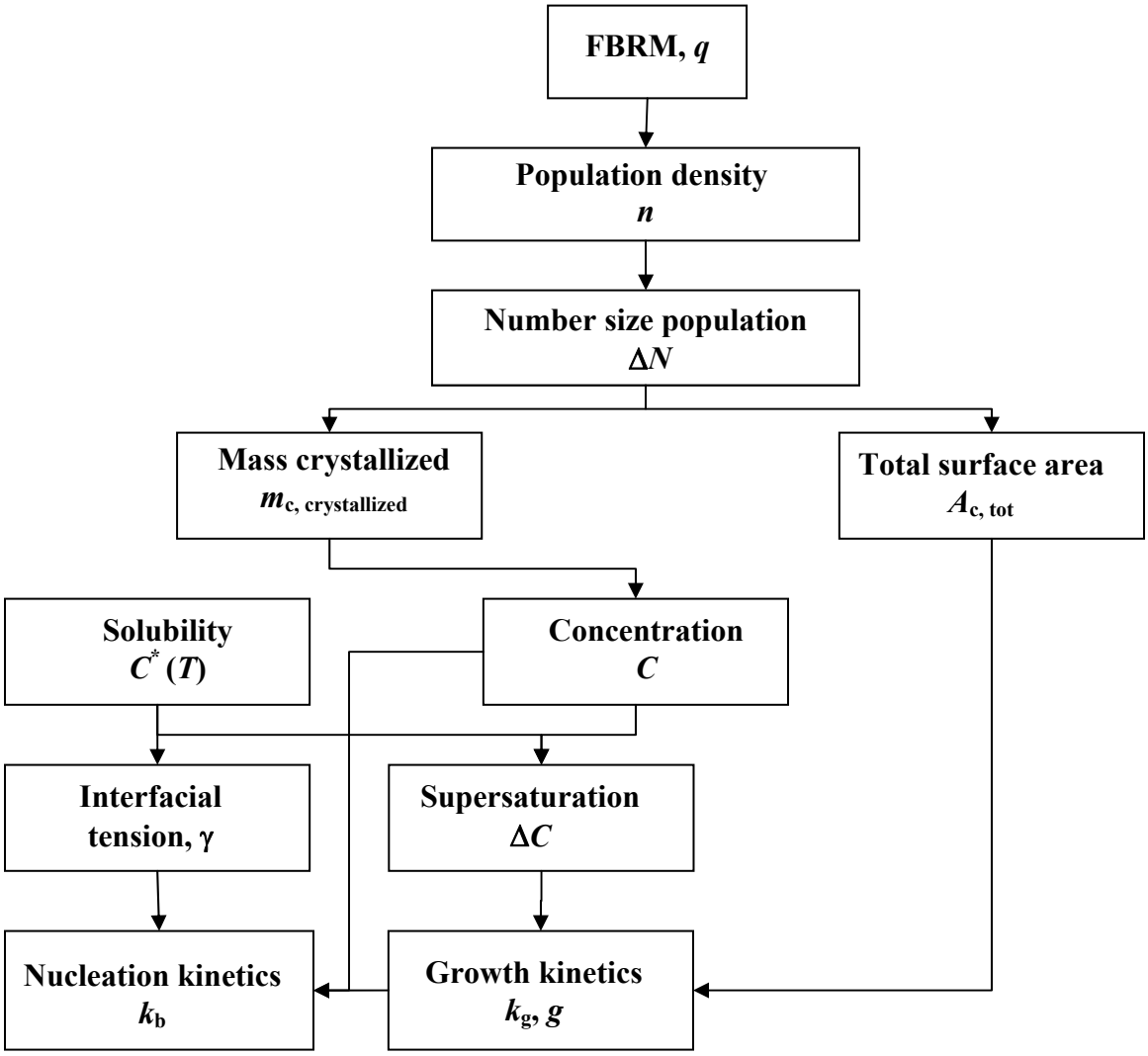

Figure 26. Methodology

5.2 Experimental set-up

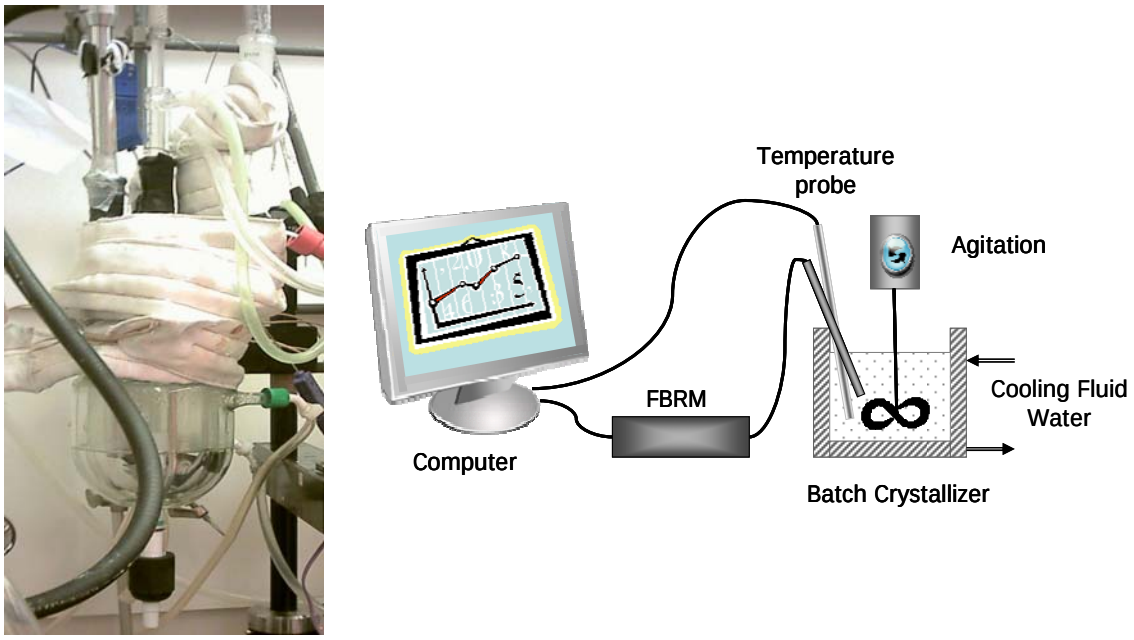

Figure 27. Experimental apparatus

The experimental set up is shown in Figure 27. A 500 mL jacketed batch crystallizer was used. The mixing was realized through a 4-blade impeller rotating at a speed of 400 rpm; the crystallizer had 3 baffles and the FBRM probe, which served to enhance the mixing. The Reynolds number was estimated to be 8,900, and visual observations indicated good mixing. The batch reactor was linked to a programmable water bath. The temperature was measured and recorded through the use of a thermocouple inserted into the slurry, and linked to an Omega Daq 56 data acquisition system which offers a precision between 0.10 and 0.20 °C. Solvent loss was eliminated through the addition of a condenser on top of the crystallizer that condensed vapors of ethanol generated. A Lasentec Focused Beam Reflectance Measurement D600 was used to provide in-line monitoring of the evolution of the crystal population.

A “seeded” crystallization procedure was designed and implemented in order to isolate growth of the crystals in the batch cooling crystallization of paracetamol from an ethanol solution. The experimental conditions were designed to render nucleation negligible during a defined growth period. In a typical run, solute and solvent were added to the crystallizer, and the resulting solution was heated to 70 ºC, which insured complete dissolution of the crystals. A run began when the system cooling and the data acquisition were started. The initial cooling was at a pre-determined linear rate from 70 ºC to 48 ºC, during which time nucleation occurred to form the population of seed crystals. After allowing the system to stabilize at 48 ºC for 1 hour, a second cooling period, with a reduced cooling rate, was initiated with the intention of growing the existing crystalline population without nucleation of additional crystals. Once the system reached 10 ºC, the temperature was held constant.

The goal of this procedure was to isolate growth of the crystals by rendering nucleation negligible during the second cooling step as illustrated in Figure 28. In other words, this cooling profile was designed to separate nucleation from growth, thus allowing the estimation of both kinetics.

5.3 Experimental results

5.3.1 Estimation of supersaturation

Figure 28 shows how temperature and total chord counts were tracked in a typical run, which will be the focus of the discussion. After nucleation and a corresponding rapid increase in total chord counts, the temperature was maintained constant until steady state was achieved, which is indicated by a constant total number of chord counts. As the

cooling was resumed, the total number of chord counts remained constant, meaning there was no further significant nucleation and growth of the previously formed crystals could be followed.

The solubility of paracetamol was estimated as a function of time using Equation (53). The FBRM raw data were used to estimate the population density according to the methodology detailed in Chapters 3 and 4. The conversion matrix was computed, as well as its eigenvalue decomposition. Due to the noise level and the assumed octahedral shape, and according to the procedure described in chapter 4, we use $m' = 70$. This principal component analysis was then used to estimate $\boldsymbol{n}_1$ from the FBRM raw data and $\Delta \boldsymbol{N}$ was estimated through Equation (51).

The evolution of the normalized population density, $\boldsymbol{n}_1$, is shown in Figure 29 for a typical run. Nucleation occurred at $t = 188$ min, and here Figure 29 shows the length-weighted population at different times after nucleation. As time increases, the crystals are growing, the peak shifts toward higher sizes, and the distribution becomes broader. As Mydlarz and Briedis (1992) showed in their work, the slight tails of the distributions noticed in Figure 29 can be caused by growth-rate dispersion. This effect is minimal and so as to keep the model fairly simple, the growth kinetics will be assumed to be size-independent and without growth rate dispersion.

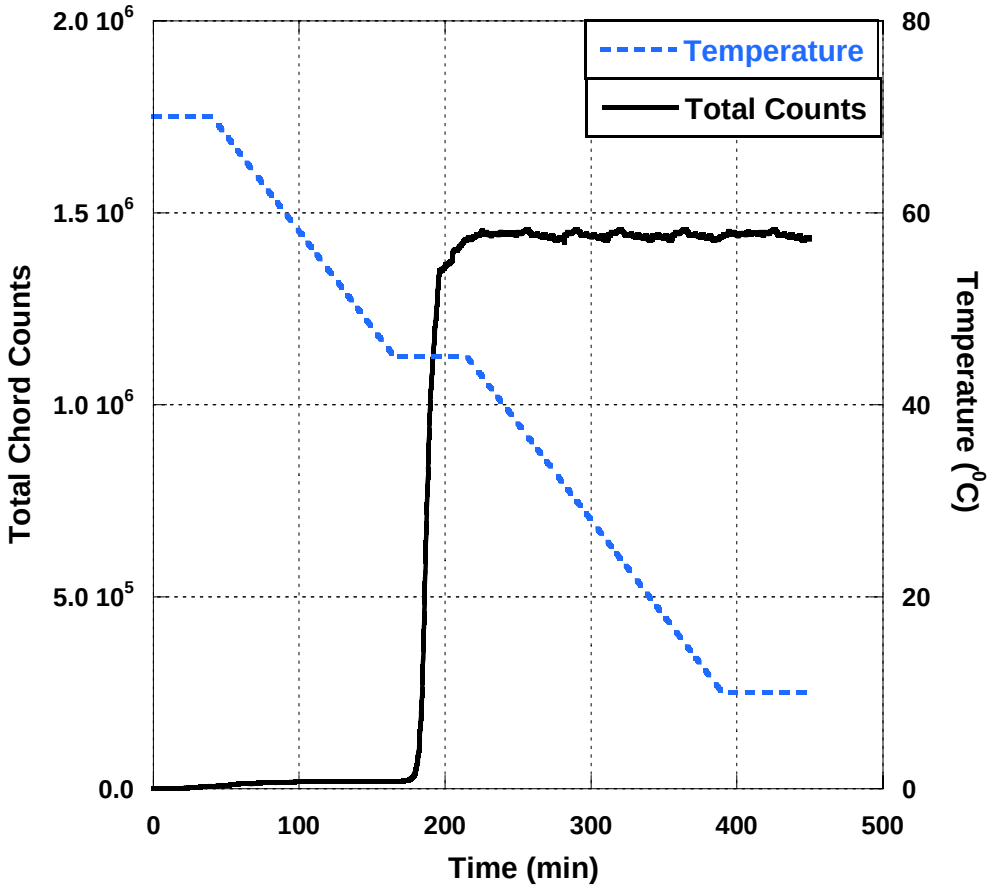

Figure 28. Evolution of temperature and total chord counts

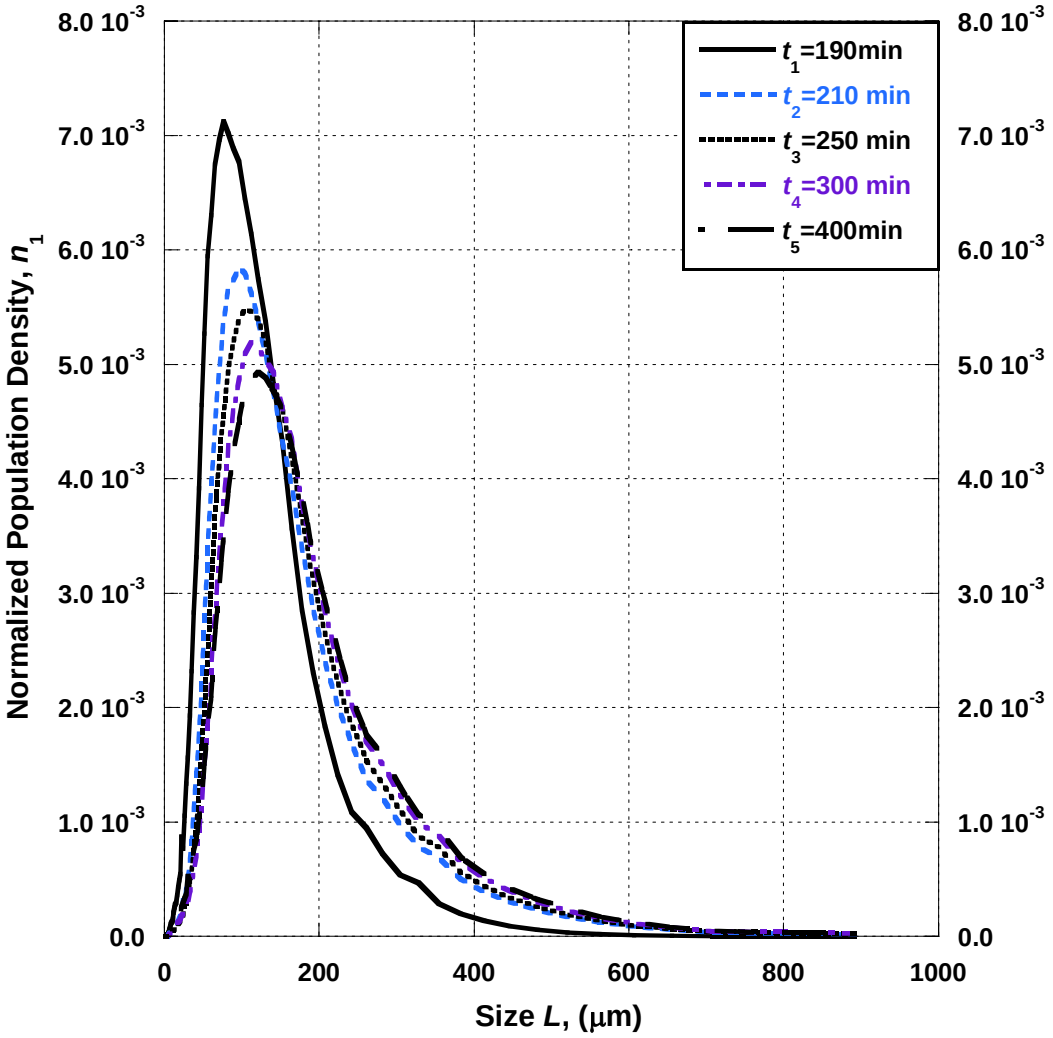

Figure 29. Estimated n_1 at different times

Having estimated $\boldsymbol{n}_1$ and N_T, we were then able to compute the total surface area and the total volume of the crystals as a function of time. The evolution of the concentration, C, throughout the run was then estimated using Equation (61). As shown in Figure 30, the evolution of the concentration and the mass crystallized had opposite trends. As the system was cooled to the nucleation point, the solute concentration remained constant and there was no mass crystallized. As nucleation occurred, C decreased while $m_{c,crystallized}$ increased until a plateau was reached, which is indicative of a steady state. At this point, cooling was resumed and the crystals grew. As the concentration decreases, once again the mass of crystals increases until the steady state is reached. The system is then at equilibrium, the crystals are no longer growing. The model predicts an averaged total $m_{c,crystallized}$ of 0.061 kg, while the averaged mass collected at the end of the run was 0.059 kg. This difference (5.3 % maximum error) may be partly attributed to the fact that some solid is lost or accumulated on the wall of the vessel during the recovery process.

Two sets of three runs were realized leading to similar results (Table 5). The first cooling rate on the first cooling step was set to be − 0.20 º C/min for both runs while the cooling rate on the second cooling step was different (Run 1: − 0.20 ºC/min and Run 2: − 0.35 ºC/min). Similar nucleation events were noticed. The supersaturation was generated at a higher rate during Run 2 leading to steady state faster than in Run 1.

Table 5. Prediction of $m_{c,crystallized}$ vs. experimental results (in kg)

		$m_{c,crystallized}$	$m_{c,recovered}$
Run 1	Experiment 1	0.059	0.056
	Experiment 2	0.058	0.056
	Experiment 3	0.068	0.065
Run 2	Experiment 1	0.064	0.061
	Experiment 2	0.057	0.055
	Experiment 3	0.062	0.059

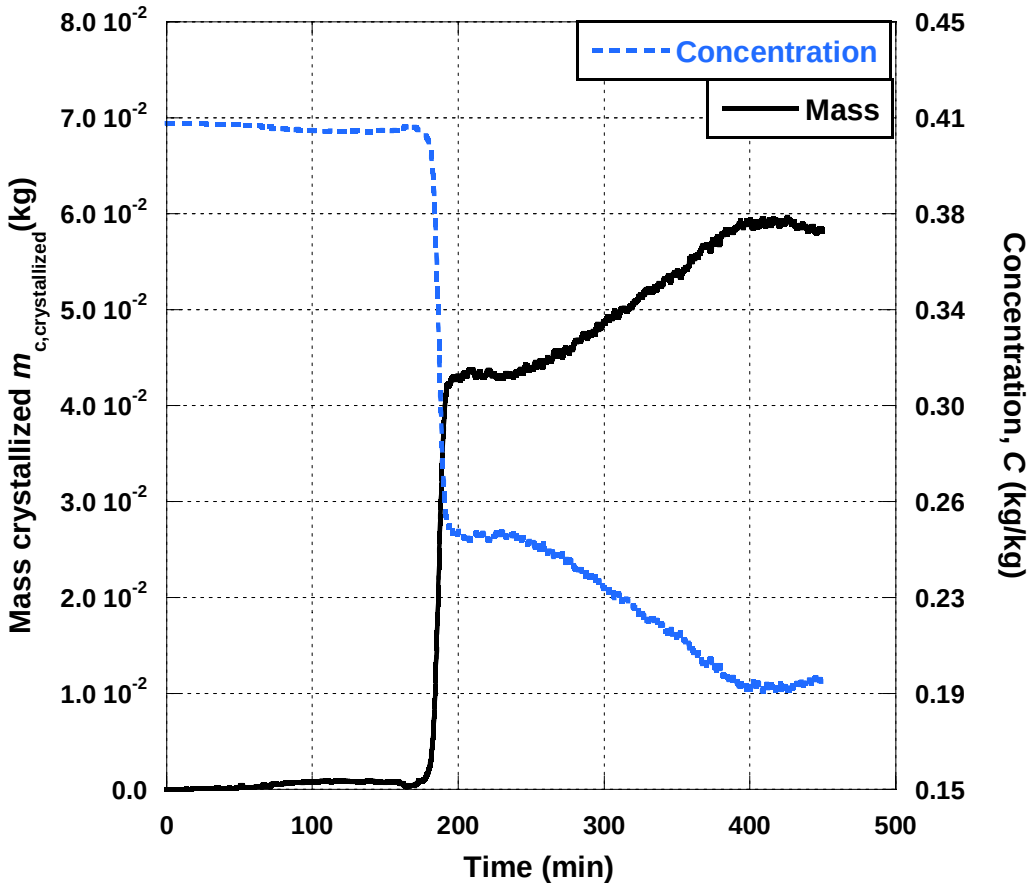

Figure 30. Evolution of the concentration and the mass crystallized (Run 1- Experiment 1)

5.3.2 Estimation of growth kinetics

We now focus on the data from the second cooling step, which corresponds to the growth-only regime. This assumption is verified by observing that N_T was constant during the second cooling step, as shown in Figure 28. Equation (68) was then used to obtain the growth kinetics of the system. The highest variations of the data from the general correlation are observed for low ΔC, which corresponds to the end of the run. This discrepancy can be explained by the fact that the system is close to equilibrium, denoted by a small variation of ΔC and low temperature, the growth of the crystal is therefore small. Our model assumes a temperature-independent k_g, hence the slower growth of the crystal at low temperature was not taken into account leading to divergence in between the actual behavior and the modeled one.

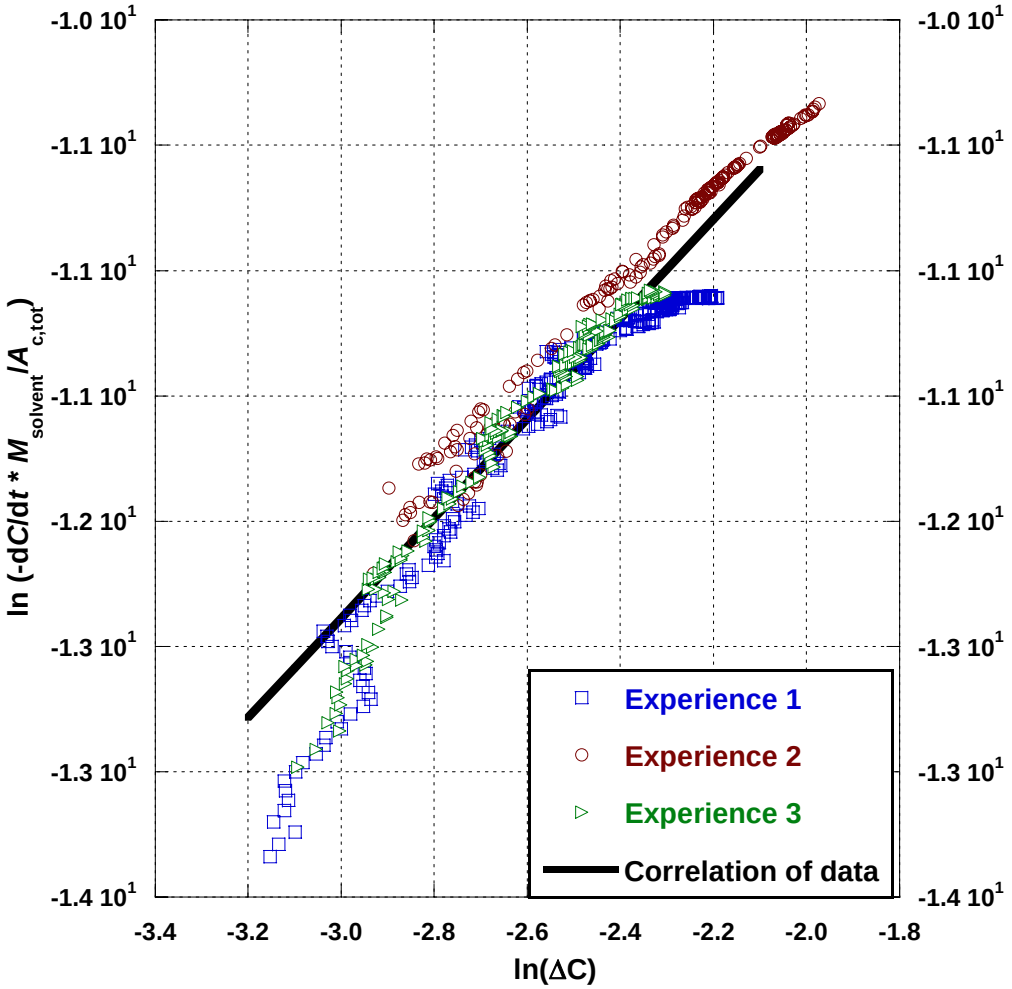

Figure 31. Computation of the growth kinetics, Run 1

The procedure highlighted in Section 5.1.3 was applied to two sets of three repetitive experiments with different cooling rates during the second cooling step (Run 1: − 0.20 ºC/min and Run 2: − 0.35 ºC/min). The results for Run 1 are shown in Figure 31. The results of Run 2 are similar and in a concern of graph clarity were not added to the graph. Fitting the data with Equation (68), over our considered range of temperature (10 – 48 ºC), gave $k_g = 1.71 \times 10^{-4}$ kg·m^{-2}·s^{-1} (kg / kg solvent)$^{-g}$ with a 95% confidence interval of $\pm 4.41 \times 10^{-5}$ kg·m^{-2}·s^{-1} (kg / kg solvent)$^{-g}$ and $g = 1.98$ with a 95 % confidence interval of ±0.04. The correlation is illustrated in Figure 31 as a solid line. Notice that all the experimental points are grouped around this general correlation. The results from each experiment are shown below in Table 6. The variation between each run is not significant for g and slight for k_g as shown in Table 7. The modification of the cooling rate influences more k_g which is a function of the temperature than g. The only difference between the two run is the cooling rate, which does not influence k_g. The time needed to reach steady state is lower in Run 2, hence reducing the number of points used to obtain the correlation of data. This can be a source of slight variation observed in k_g in between the runs. As shown in Table 7, the standard deviation within one run is comparable to the overall standard deviation for k_g and for g.

Table 6. Results for growth kinetics (k_g is in kg·m^{-2}·s^{-1} (kg / kg solvent)$^{-g}$)

		k_g	g
Run1	Exp1	1.71×10^{-4}	2.02
	Exp2	1.38×10^{-4}	1.90
	Exp3	2.61×10^{-4}	2.05
Run2	Exp1	2.01×10^{-4}	1.91
	Exp2	1.74×10^{-4}	1.98
	Exp3	0.81×10^{-4}	2.01

Table 7. Analysis of the results

	Mean		Standard deviation	
	k_g	g	k_g	g
Run 1	1.90×10^{-4}	1.99	6.37×10^{-5}	0.08
Run 2	1.52×10^{-4}	1.97	6.30×10^{-5}	0.05
Overall	1.71×10^{-4}	1.98	6.03×10^{-5}	0.06

A limited amount of work has been published on the growth rate of paracetamol in various solvents. To provide some insight on the evolution of the growth kinetics with different solvent the results of those studies is presented here. Granberg et al. (1999) established the growth kinetics of paracetamol in acetone-water mixtures at 16 ºC, and found a g varying from 1.7 to 1.2 and k_g from 6×10^{-5} to 25×10^{-5} kg·m^{-2}·s^{-1} (kg / kg solvent)$^{-g}$ depending upon the composition of the solvent. They used electrosensing zone measurement, sieving and microscopic observations (Granberg 1999). Granberg and co-workers later extended their study to water – acetone – toluene mixtures. They obtained a value of $g \sim 1.7$ and $k_g \sim 0.35\times10^{-5}$ kg·m^{-2}·s^{-1} (kg / kg solvent)$^{-g}$ for a solvent of 3 mass% water, 92.15 mass% acetone and 4.85 mass% toluene at a temperature of 16 ºC (Granberg 2005). Additional studies were also performed by Mazzotti and co-workers who obtained a value of $g = 1.9$ and $k_g = 21.0\ \exp(-4.16\times10^{7}/\mathrm{R}T)$ m·s^{-1}(m^3·kmol^{-1})^g for paracetamol growth in ethanolic solutions studied through ATR-FTIR and densitometry techniques (Worlitchek 2004). This work was used to extract the activation energy, and we utilize this value later in this chapter.

Other groups focused on the face growth kinetics of paracetamol in different solvents. Shekunov et al. (1996, 1997) studied the face growth kinetics of paracetamol in ethanolic solutions using interferometric techniques at two temperatures 3 ºC and 47 ºC. They focused on the growth mechanism of the different crystal faces. It was concluded that the crystal growth, as well as its quality, were strongly dependant on the temperature; growth rates ranged from $G = 10^{-7}$ to 10^{-8} kg·m^{-2}·s^{-1}. Finnie et al. (1996, 1999) studied the face growth rate in aqueous solutions at 30 ºC through optical microscopy and X-Ray topography techniques. Their work investigates how the crystal growth conditions can be exploited in order to modify the physical properties of the crystal.

From the cited studies, it can be expected to find a value of $g > 1$. The results obtained here are not far from those reported in those previous studies. We now introduce we introduce the temperature dependence of k_g in the expression of the growth kinetic. The value obtained experimentally will be attributed to the average temperature over the considered range. Hence k_g (29 ºC) = 1.71 $\times 10^{-4}$ kg·m^{-2}·s^{-1} (kg / kg solvent)$^{-g}$. An Arrhenius law is then used, the activation energy E_a = 41.6 kJ/mol (Worlitchek 2004) and $k_{g,0} = 2.68 \times 10^{3}$ kg·m^{-2}·s^{-1} (kg / kg solvent)$^{-g}$. The evolution of k_g with the temperature is shown in Figure 32. The growth kinetics are thus expressed:

$$G = k_{g,0} \exp\left(-\frac{E_a}{RT}\right) \Delta C^g \tag{71}$$

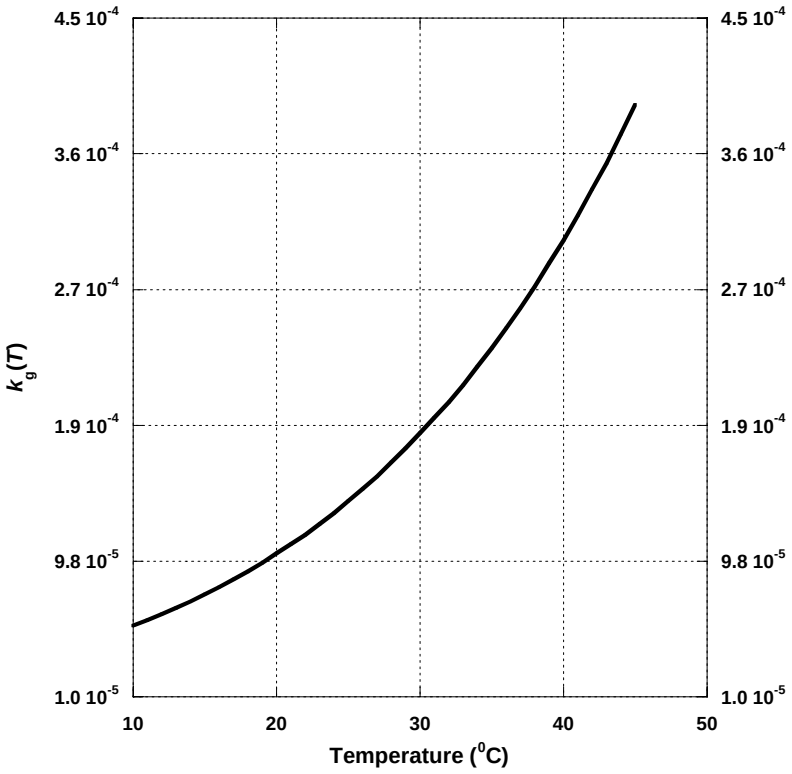

Figure 32. Evolution of k_g with the temperature

When using this expression to verify the fit in the results for Experience 1 Run 1, we obtain the results in Figure 33. We can see that the incorporation of the temperature dependence in k_g provide a better correlation towards higher ΔC. The difference noticed for smaller ΔC is still present when using $k_g(T)$. The results for Experiences 2 and 3 are similar.

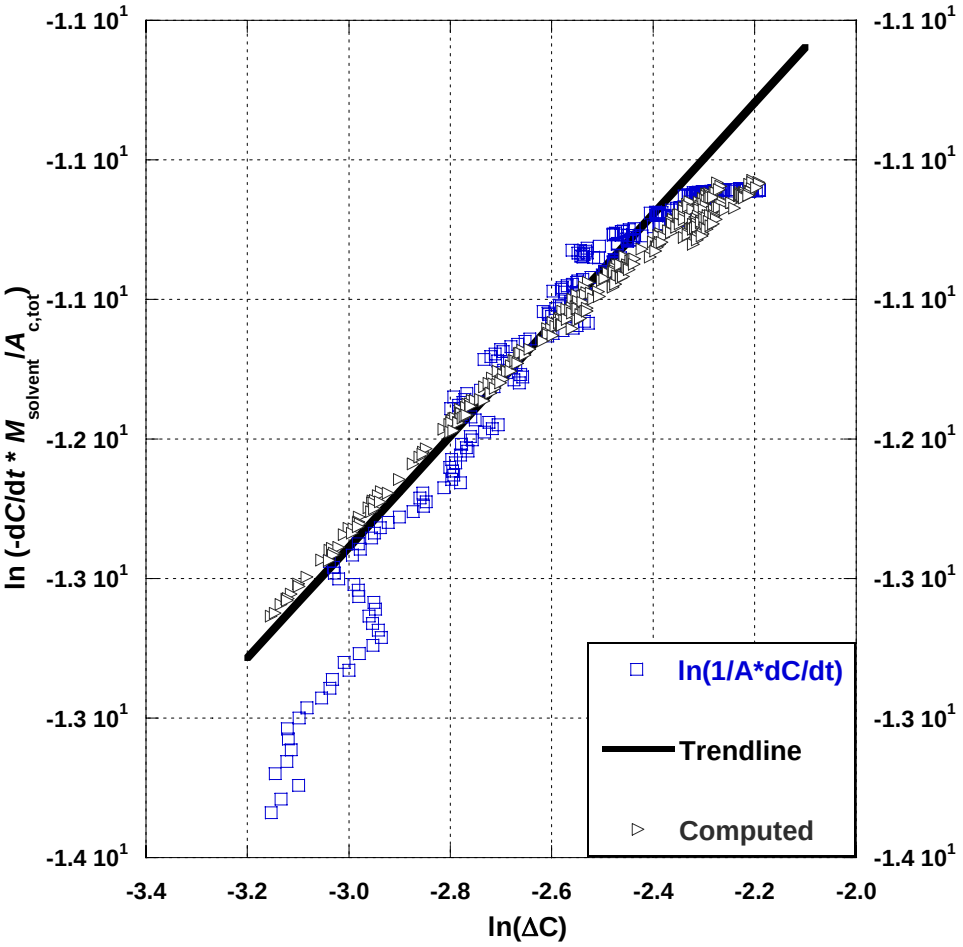

Figure 33. Temperature dependant growth kinetic (Run 1- Experience 1)

5.3.3 Estimation of nucleation kinetics

In order to establish the nucleation kinetics, we now apply the previously detailed methodology from Section 5.1. In Figure 34, the experimental nucleation rate R_b, is calculated from Equation (62) and compared to the fitted results from equation (69). We can see the nucleation event clearly identified by a sharp peak at t = 188 min. Through experimental fitting with Equation (69) and assuming no growth, we estimate k_b = 3.39 $\times 10^{10}$ kg·s^{-1} with a 95 % confidence interval of ± 3.42$\times 10^{9}$ kg·s^{-1}. The interfacial tension, γ, was also computed through Mersmann formula (Equation (70)) and ranged from 53 to 56 mJ·m^{-2} over the considered range of temperature. Overall the experimental data are accurately represented by the model. The nucleation event is clearly indicated by a sharp peak. Note that there is no secondary nucleation and that the supersaturation is exclusively dissipated through growth phenomenon once the nucleation event is over.

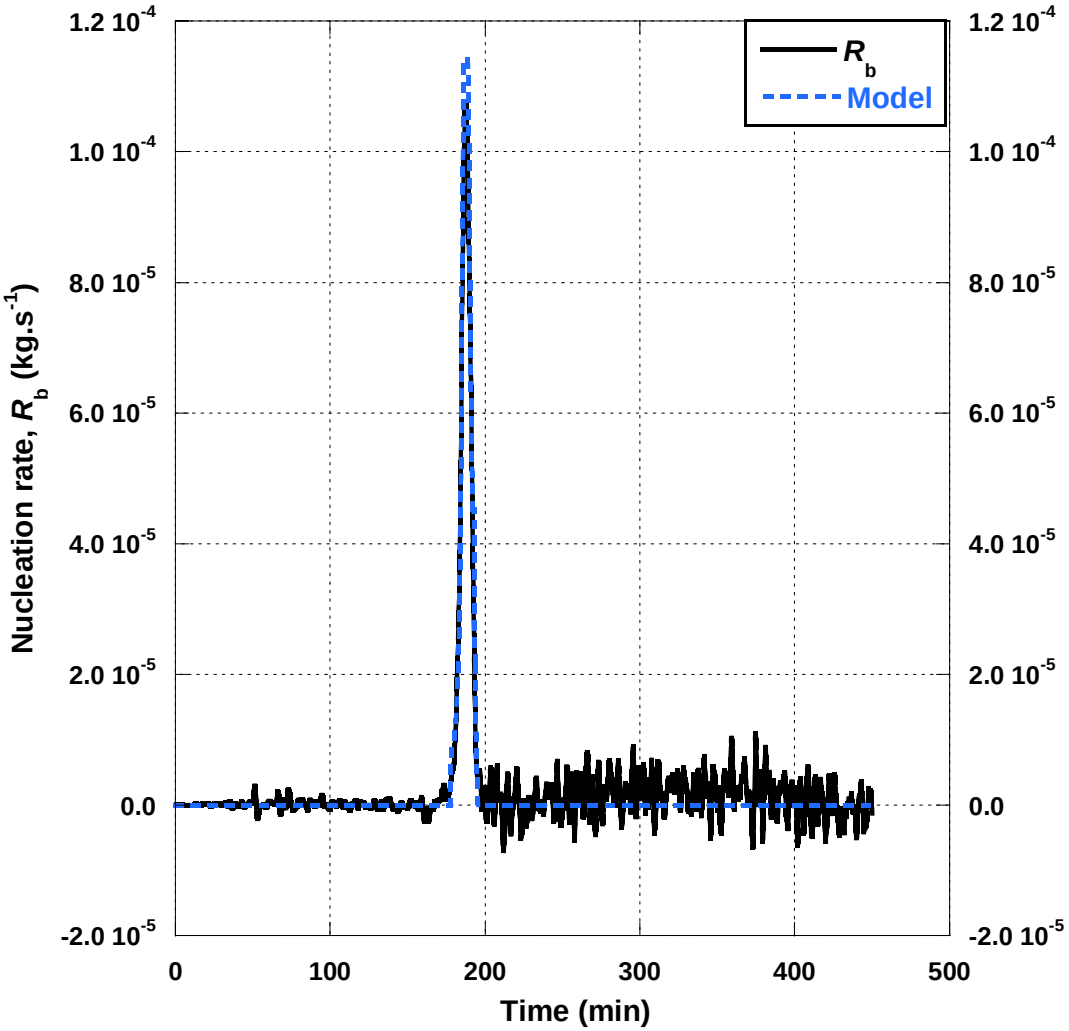

Figure 34. Evolution of the nucleation rate

The same procedure was applied to two sets of three experiments; the results are shown below in Table 8. The average and the standard deviation do not vary significantly between the two runs as shown in Table 5, the results are reproducible.

Table 8. Results for nucleation kinetics (k_b is in kg·s^{-1})

		k_b
Run 1	Exp 1	3.37×10^{10}
	Exp 2	4.00×10^{10}
	Exp 3	2.98×10^{10}
Run 2	Exp 1	2.78×10^{10}
	Exp 2	3.41×10^{10}
	Exp 3	3.82×10^{10}

Table 9. Analysis of the results

	Mean	Standard Deviation
	k_b	k_b
Run 1	3.45×10^{10}	5.15×10^{9}
Run 2	3.34×10^{10}	5.24×10^{9}
Overall	3.39×10^{10}	4.69×10^{9}

Earlier, we made the assumption of no nucleation on the second cooling step. This will now be verified. To do so, we computed the growth and the nucleation at two different times, t_1 = 188 min and t_2 = 300 min. We estimate at nucleation: $R_b(t_1) = 1.14 \times 10^{-4}$ kg·s^{-1} and $A_{c,tot}G(t_1) = 2.41 \times 10^{-9}$ kg·s^{-1} and during the second cooling step: $R_b(t_2) = 1.10 \times 10^{-10}$ kg·s^{-1} and $A_{c,tot}G(t_2) = 1.16 \times 10^{-7}$ kg·s^{-1}. Hence we have, at nucleation $R_b >> A_{c,tot}G$ and during the second cooling step $A_{c,tot}G >> R_b$. The assumption made

during the second cooling step is justified, nucleation is negligible. This corroborates the assumption made from the evolution of N_T.

Little work has been published on the nucleation kinetics of paracetamol, none providing trustworthy numerical data. Nagy et al. (Nagy 2008) from Braatz's group used metastable zone width experiments combined with three possible methodologies to determine the kinetics of nucleation of paracetamol in water. Their work reached the conclusion that important errors were introduced due to the assumptions made and the model used. As a result, the precision and values found for the nucleation kinetics varied greatly with the method employed. Granberg and co-workers (2001) studied the primary nucleation of paracetamol in acetone-water mixture through the study of the induction times and focused their work on the interfacial energy, an increase in solubility, decreased percentage of water in the solvent, leads to a decreasing interfacial energy, and increased nucleation. Mullin provides a general order of magnitude for the nucleation kinetic coefficient of 10^3 to 10^5 $cm^{-3} \cdot s^{-1}$ for heterogeneous crystallization and 10^{25} to 10^{30} $cm^{-3} \cdot s^{-1}$ for homogeneous nucleation (Mullin 2001). In this work we have 3.96×10^{18} $cm^{-3} \cdot s^{-1}$, this tends to indicate homogeneous nucleation.

5.3.4. Comparison of the model to experimental data

In order to verify the accuracy of the model describing the growth and nucleation kinetics, the evolution of the concentration, C, was computed using Equation (62). We use the value of $A_{c,tot}$ obtained experimentally through Equation (66) and the values for the kinetics obtained in the previous sections. The mass crystallized, $m_{c,crystallized}$, is also deduced from the concentration through Equation (55). The evolution versus time of both

is plotted in Figure 35. It can be noticed that the value of the concentration is slightly overestimated while as a consequence the mass crystallized is underestimated but the general trend is well predicted. The average error on the concentration is 4.07 % with a maximum at 8.64 % while the average error on the mass crystallized is 3.22 % with a maximum at 7.42 %. The data fitting process used to estimate the kinetics, as described in the previous section, does not lead to a loss in information.

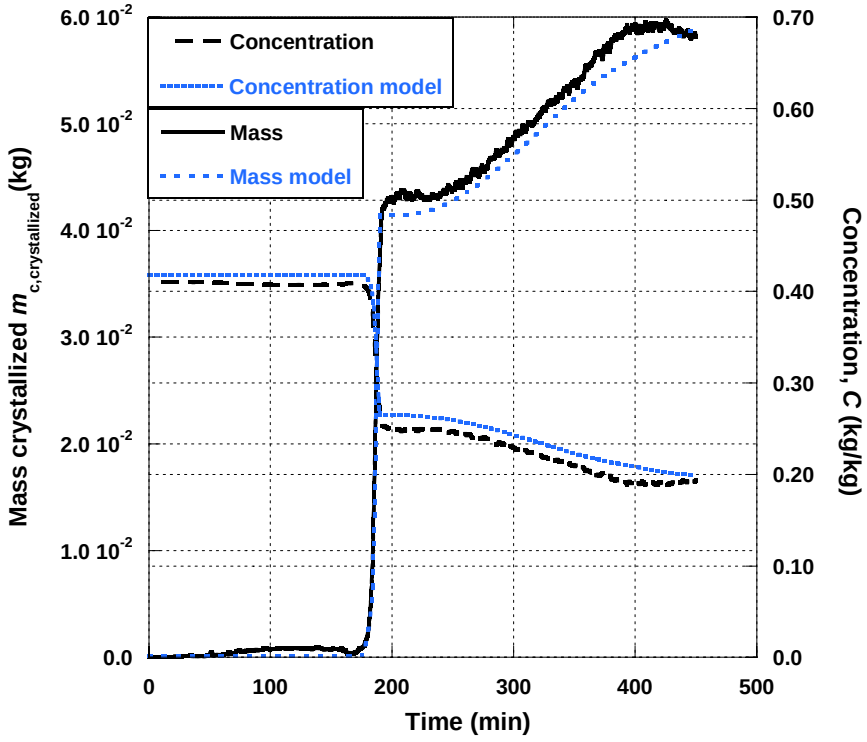

Figure 35. Modeled vs. experimental evolution of *C* and $m_{c,crystallized}$

To summarize, the FBRM technology allows on-line monitoring of the chord-length density which leads to an estimation of the evolution of n_1, which was then used to

estimate the number population density $\Delta \boldsymbol{N}$. The supersaturation, ΔC, was then estimated and used to calculate growth and primary nucleation kinetics for the considered system.

The results from the experiments in the present chapter show how a seeded crystallization can be implemented in order to extract the growth kinetics of the system. Knowledge of the growth and primary nucleation kinetics is essential to solve the population balance, which can lead to a better control of the process. Those results can be used to enable the resolution of the population balance so as to establish a predictive model based on growth and nucleation rates of the studied system.

Usually, several costly instruments are needed to regroup the data necessary to estimate the kinetics of a system, specifically supersaturation. The FBRM provides the advantage of computing the supersaturation of a solution using only one instrument, while also providing on-line, in-situ measurements of the evolution of the population.

CHAPTER 6

POPULATION BALANCE

Population balances have been used to model the evolution of particle populations in a wide range of processes, including crystallization. Since they cannot always be solved analytically, several groups have investigated numerical methodologies to solve the equations. For example, Ramkrishna and co-workers (1996, 1997, 2000 and 2002) used a refined Galerkin method on finite elements to obtain the solution of population balance equations for precipitation processes. Gunawan et al. (2004) proposed to adapt the high-resolution finite-volume methods developed for compressible gas dynamics to solve multidimensional population balance models. Other groups, such as Qamar and co-workers (2007, 2008) and Lim and co-workers (2002), based their approach on combining a high resolution spatial discretization method and a modified method of characteristics to evaluate the solution. In the present work, we will compare a finite-difference method to the moment transformation method.

Once the system kinetics are established (see Chapter 5), fully modeling the system can be done by solving the population balance. A population balance begins with the general statement:

$$\text{Accumulation} = \text{Input} - \text{Output} + \text{Net Generation} \tag{72}$$

Assuming the active volume of a well-mixed crystallizer is constant, the population balance can be written explicitly as (Randolph and Larson 1971, Mullin 2001):

$$\frac{\partial n}{\partial t}+\frac{\partial (Gn)}{\partial L}+D_{\mathrm{p}}-B_{\mathrm{p}}=-\sum_{k}\frac{n_k Q_k}{V} \tag{73}$$

where G is the growth rate, $\left(\frac{dL}{dt}\right)$, D_{p} is a particle death function, B_{p} is a particle birth function, n_k is the volume-weighted population density for the k^{th} stream, Q_k is the volumetric flow rate for the k^{th} stream, and V is the active crystallizer volume. Equation (73) can be further simplified. For the simple case examined here, i.e. batch cooling crystallization with no fines removal, $Q_k = 0$. Breakage and agglomeration will be neglected so that the possibility of particles appearing (birth function B_{p}) or disappearing (death function D_{p}) in the suspension due to those phenomena is assume negligible: $B_{\mathrm{p}} = 0$ and $D_{\mathrm{p}} = 0$. Equation (73) becomes:

$$\frac{\partial n}{\partial t}+G\frac{\partial n}{\partial L}=0 \tag{74}$$

with the initial condition:

- $n(0,L) = 0$ which means that at time $t = 0$, the solution is clear
- $n(t,0) = n^0 = R_{\mathrm{b}} / G$ where n^0 is the population density of nuclei, i.e. crystals at $L = 0$.

The growth and nucleation kinetics are dependent upon the supersaturation. Therefore solving the population balance shown in Equation (74) requires solving a coupled system of partial differential equations describing the population balance and solute mass. The kinetics determined in the previous chapter are used here but in another

system of units. R_b is in number·m^{-3}·s^{-1} and G is in m·s^{-1}. R_b was previously established in both unit system, the relationship between the mass growth rate and the linear one is as follows:

$$G\left[\mathrm{m}\cdot\mathrm{s}^{-1}\right]=\frac{k_a}{3k_v\rho}G\left[\mathrm{kg}\cdot\mathrm{m}^{-2}\cdot\mathrm{s}^{-1}\right] \tag{75}$$

Where k_a is the surface shape factor, k_v the volumetric shape factor and ρ the density.

6.1 Methodology

The differential equations describing the evolution of the concentration, C, and the population density, n, are coupled and, therefore, need to be solved simultaneously (Randolph and Larson 1971).

$$\frac{\partial n}{\partial t}+G\frac{\partial n}{\partial L}=0 \tag{74}$$

$$\frac{dC}{dt}=-\frac{1}{2}\frac{\rho}{M}k_aG\int_0^\infty nL^2dL \tag{76}$$

where k_a is the surface area shape factor which serves as a proportionality constant between particle size and surface area (Lachman, 1986). For the paracetamol crystals considered here, k_a is given by:

$$\mathrm{Area}_{\mathrm{octahedron}}=k_aL^2=\sqrt{3}\left(\sqrt[3]{\pi}L\right)^2 \tag{77}$$

where L is the equivalent diameter. Hence, $k_a=\sqrt{3}\left(\sqrt[3]{\pi}\right)^2$. The initial and boundary conditions are:

- $n(0,L) = 0$
- $n(t,0) = n^0 = R_b / G$

- $C(t=0) = C_0$

The growth and nucleation kinetics are defined in Chapter 5:

- $G = k_{g,0} \exp\left(-\frac{E_a}{RT}\right) \Delta C^g$

- $R_b = k_b \, exp\left(\frac{-16\pi\gamma^3 \left(M/\rho\right)^2}{3k^3T^3 \, ln^2\left(C/C^*\right)}\right)$

where k_g, g and k_b are kinetic parameters as defined in Chapter 5, M is the molecular mass (for paracetamol, M = 151.16 g/mol), γ is the surface tension (see Chapter 5), ρ is the density, T is temperature in K, k is the Boltzman constant, C is solute concentration, and C^* is the solute solubility.

There are many ways to solve this system of differential equations. Here, we will first implement a finite-difference approximation of the equation, and secondly we will use the moments methodology described by Randolph and Larson (1971). Finally, the accuracy of both methods are compared to one another and to the data collected through the FBRM.

6.1.1 Finite-difference resolution

When discretized, Equations (74) and (76) can be written

$$\begin{cases} \dfrac{\boldsymbol{n}\left(\bar{L}_j, t_{i+1}\right) - \boldsymbol{n}\left(\bar{L}_j, t_i\right)}{\Delta t} + G\left(t_i\right) \dfrac{\boldsymbol{n}\left(\bar{L}_j, t_i\right) - \boldsymbol{n}\left(\bar{L}_{j-1}, t_i\right)}{\Delta L_j} = 0 & (78) \\ \dfrac{C\left(t_{i+1}\right) - C\left(t_i\right)}{\Delta t} = -\dfrac{1}{2}\dfrac{\rho}{M} k_a G\left(t_i\right) \sum_{j=1}^{\infty} \boldsymbol{n}\left(L_j, t_i\right) L_j^2 \Delta L & (79) \end{cases}$$

where Δt and ΔL_j the step size relative to time and size. The system of equations can be rewritten to obtain $\boldsymbol{n}(\bar{L}_j, t_{i+1})$ and $C(t_{i+1})$ explicitly.

$$\begin{cases} \boldsymbol{n}\left(\bar{L}_j, t_{i+1}\right) = \boldsymbol{n}\left(\bar{L}_j, t_i\right) - \Delta t\left(k_{\mathrm{g}}\left(C\left(t_i\right) - C^*\left(t_i\right)\right)^g \dfrac{\boldsymbol{n}\left(\bar{L}_j, t_i\right) - \boldsymbol{n}\left(\bar{L}_{j-1}, t_i\right)}{\Delta L_j} \right) & (80) \\ C\left(t_{i+1}\right) = C\left(t_i\right) + \Delta t\left(-\dfrac{1}{2}\dfrac{\rho}{M} k_{\mathrm{a}} k_{\mathrm{g}}\left(C\left(t_i\right) - C^*\left(t_i\right)\right)^g \sum_{j=1}^{\infty} \boldsymbol{n}\left(L_j, t_i\right) L_j^2 \Delta L \right) & (81) \end{cases}$$

The initial and boundary conditions are then defined by (Lim 2002, Costa 2007)

- $\boldsymbol{n}(t_1, L_{\mathrm{j}}) = 0$
- $\boldsymbol{n}(t_{\mathrm{i}}, L_1) = \boldsymbol{n}^0 = R_{\mathrm{b}}(t_{\mathrm{i}}) / (G(t_{\mathrm{i}}) / \Delta L_1)$
- $C(t_1) = C_0$

The main difficulty in this Runge-Kutta method of order 1 is to find a sufficiently small step size. We use Δt = 10 s and ΔL = 0.1 μm in obtaining the results discussed in Section 6.2. Those step sizes were determined through trial and error. It is essential for the step size to be small enough so it doesn't influence the results of the simulation but still high enough so the computation time is reasonable.

6.1.2 Moments transformation

Randolph and Larson (1971) and Hulburt and Kartz (1964) were among the first to investigate the applications of population balance models to crystallization. Randolph and Larson (1971) proposed using the moments of the distribution in solving the population balance. Moments were defined as:

$$m_j = \int_0^{\infty} n L^j dL \tag{82}$$

where m_j is the j^{th} moment of the population density function. Since we are assuming that the growth rate G is independent of size, Equation (74) leads to:

$$\int_0^{\infty} L^j \left[\frac{\partial n}{\partial t} + G \frac{\partial n}{\partial L} \right] dL = 0 \tag{83}$$

$$\int_0^\infty L^j \frac{\partial n}{\partial t} dL + \int_0^\infty L^j G \frac{\partial n}{\partial L} dL = \frac{dm_j}{dt} + \int_0^\infty L^j G \frac{\partial n}{\partial L} dL = 0 \tag{84}$$

$\int_0^\infty L^j G \frac{\partial n}{\partial L} dL$ can be integrated by parts (Randolph and Larson, 1971) to give

$$\int_0^\infty L^j G \frac{\partial n}{\partial L} dL = -0^j \bullet R_b - jGm_{j-1} \tag{85}$$

$$\frac{dm_j}{dt} = 0^j \bullet R_b + jGm_{j\text{-}1}\ , \qquad j = 0 \ldots j_n \tag{86}$$

where R_b is the nucleation rate (number flux generated at L=0). Thus resolving the system described by Equations (74) and (76) is equivalent to solving the following ODE system:

$$\frac{dm_j}{dt} = 0^j \bullet R_b + jGm_{j\text{-}1} \qquad \text{for } j = 0 \ldots j_n \tag{86}$$

$$\frac{dC}{dt} = -\frac{1}{2}\frac{\rho}{M} k_a k_g \left(C - C^*\right)^g m_2 \tag{76}$$

The initial and boundary conditions are:

- $m_j(0) = 0$, the initial solution is clear
- $C(0) = C_0$

The population density is restored according to the principle given by Hulburt and Kartz (1964):

$$n(t,L) = \frac{\left(\lambda_a / a\right)\left(\lambda_a L / a\right)^{\lambda_a - 1} \exp\left(-\lambda_a L / a\right)}{\left(\lambda_a - 1\right)!}\left[m_0 + \sum_{n=3}^{j_n} c_n l_n^{(\lambda)}\left(\frac{\lambda_a L}{a}\right)\right] \tag{87}$$

where the parameters λ_a and a are functions of the moments (up to m_2) and are equal to:

$a = \frac{m_1}{m_0}$, and $\lambda_a = \frac{a^2}{\left[\left(m_2 / m_0\right) - a^2\right]}$, the n^{th} order Laguerre polynomial $l_n^{(\lambda)}$ and the n^{th} coefficient c_n are expressed by:

$$l_n^{(\lambda_a)}(p)=\sum_{j=0}^{n}(-1)^j\frac{n!(n+\lambda_a+1)!}{j!(n-j)!(n+\lambda_a-1-j)!}p^{n-j} \tag{88}$$

$$c_n=\sum_{j=0}^{n}(-1)^j\frac{(\lambda_a-1)!\left(\lambda_a/a\right)^{n-j}}{j!(n+\lambda_a-1-j)!(n-j)!}m_{n-j} \tag{89}$$

λ_a is not an integer, therefore the factorial of the non integer terms $(n+\lambda_a-1-j)!$ and $(\lambda_a-1)!$ are defined to be the factorial of the closest integer. The term (n+λ_a-1-j) was rounded to the closest integer before its factorial product was considered.

The main difficulty in using this methodology is to define the number of moments j_n, that are needed efficiently to restore the population density. It is interesting to note that when a Gamma distribution is considered, the leading terms in Equation (87) offer an exact answer, therefore only a and λ_a needs to be determined and $j_n = 2$. But as you need to implement higher order corrections through the Laguerre polynomial coefficient, oscillations are introduced, worsening the approximation, and thus the delicacy of the restoration process. The results are shown in Section 6.2.

6.2 Results

The experimental apparatus is similar to the one described in Chapter 5, operated with a linear cooling profile. The kinetics relationship developed in Chapter 5 are used to model the system, and the methodologies described in Section 5.1 were used to compute the evolution of the concentration versus time. The concentrations simulated by finite difference and by the method of moments were compared to values estimated according to the procedure described in Chapter 5.

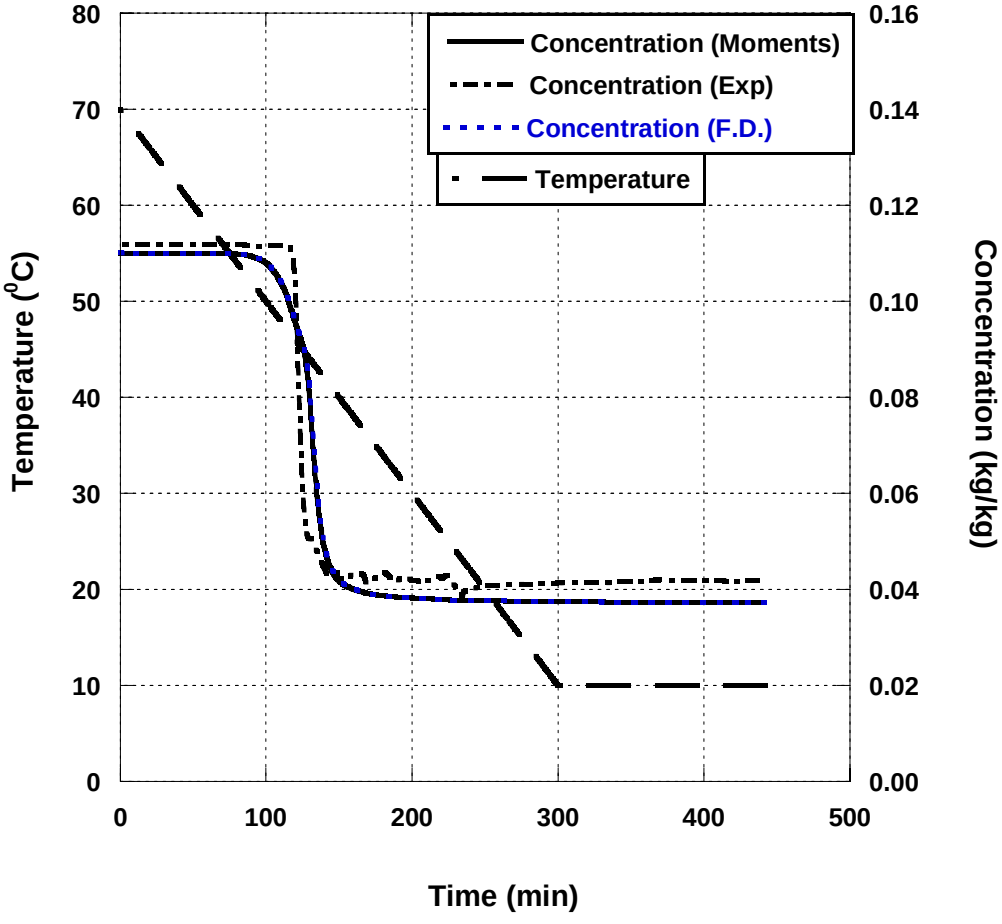

Figure 36. Experimental concentration vs. simulated one.

The results are shown in Figure 36, for a cooling batch crystallization of paracetamol from 70 ºC to 10 ºC at a rate of − 0.20 ºC/min. The simulated concentrations compare favorably to that estimated from FBRM data (i.e. using the method of Chapter 5). However, with an average error of 8.5 %, the calculations lacks precision.. The values predicted by the moments model (j_n = 8) and the finite difference method are in agreement (with a maximum error of 1.25%).

The same procedure computes the evolution of $\boldsymbol{n}(L,t)$ in parallel, and the results are shown in Figure 37. The step sizes for the calculations were 10 s and 0.1 μm, and 8 moments were used to reconstruct $\boldsymbol{n}(L,t)$ and $C(t)$. The results obtained with the two methods (finite difference and moments transformation) show similarities. Their estimation of $C(t)$ and $\boldsymbol{n}(L,t)$ present less than 2.5% difference. It was noticed that using higher order moments (larger j_n) led to higher error as oscillations were seen and worsened as j_n increased to a point where the approximation becomes useless. Nonetheless, through trials and error, it was found that using up to 8 moments led to a reasonable approximation of the population density. For the finite difference method, the time step size was chosen to be 10 s. The length step size was chosen as small as possible so as to provide a reasonable approximation of the population density but high enough to limit the computation time, ΔL = 0.1 μm. Similar results were obtained for time step sizes ranging from 5 s - 30 s for time and from 0.1 - 1 μm for length.

In Figure 37, the first peak represents a sudden increase in the small sizes of the population density as nucleation occurs. As time increases, those crystals grow, hence generating the population density to broaden and shift towards higher size ranges. A small time-lag is noticed in between the two methods, this is due to the fact that we chose

to plot the population density every 20 minutes in order to gain clarity in the graph. If plotted at smaller interval (Figure 38), both methods are in agreement. The time-lag, ε, noted in Figure 37 is due to the fact that we plot $\boldsymbol{n}(L,t)$ for the moment transformation method and $\boldsymbol{n}(L,t+\varepsilon)$ for the finite difference method. By plotting it every 20 min, we have a clearer graph but the maximum $\boldsymbol{n}(L,t)$ reached seems underestimated in the finite difference method when compared to the moments methods. Figure 38 shows a plot every 2 minutes of $\boldsymbol{n}(L,t)$, as we can see the maximum reached is within 0.15 % for the two methods. The results obtained through both methods are close, and it is interesting to note that the time interval in between two plotted representations of $\boldsymbol{n}(L,t)$ has a large influence on what is being seen.

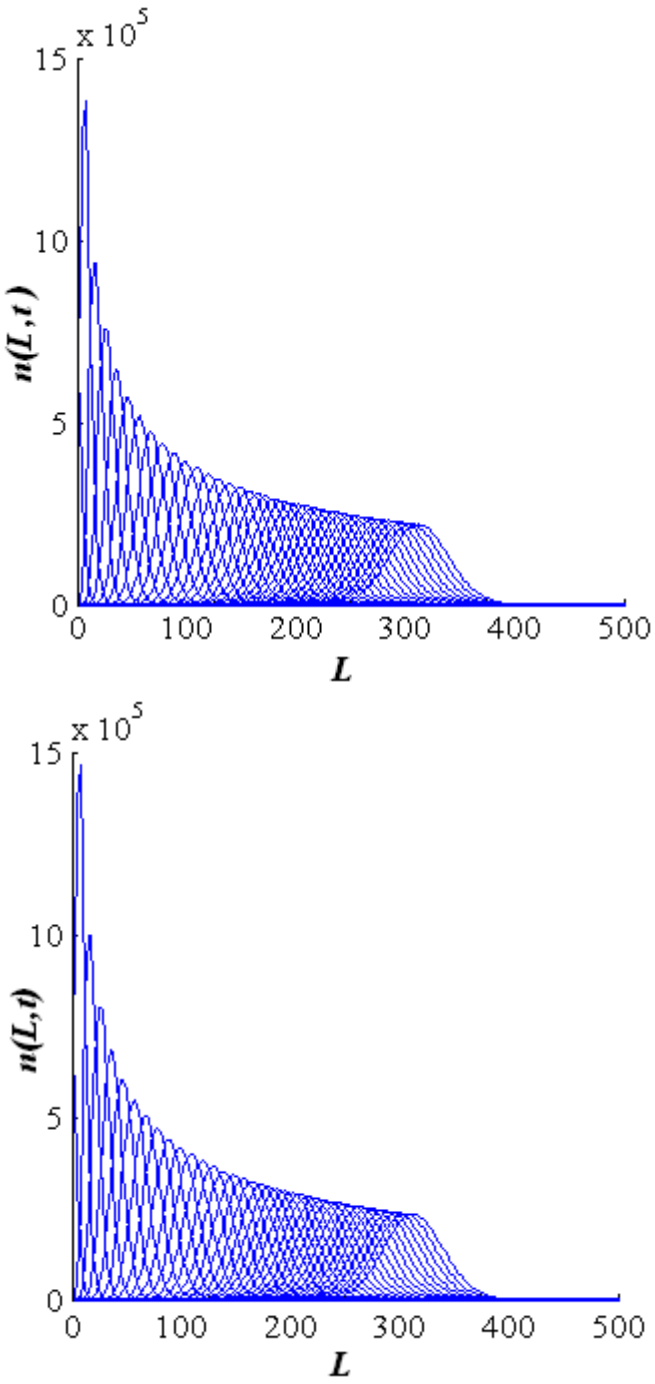

Figure 37. Simulation of the evolution of $n(L,t)$ shown every 20 min (top graph: moments method; bottom graph: finite-difference(F.D.))

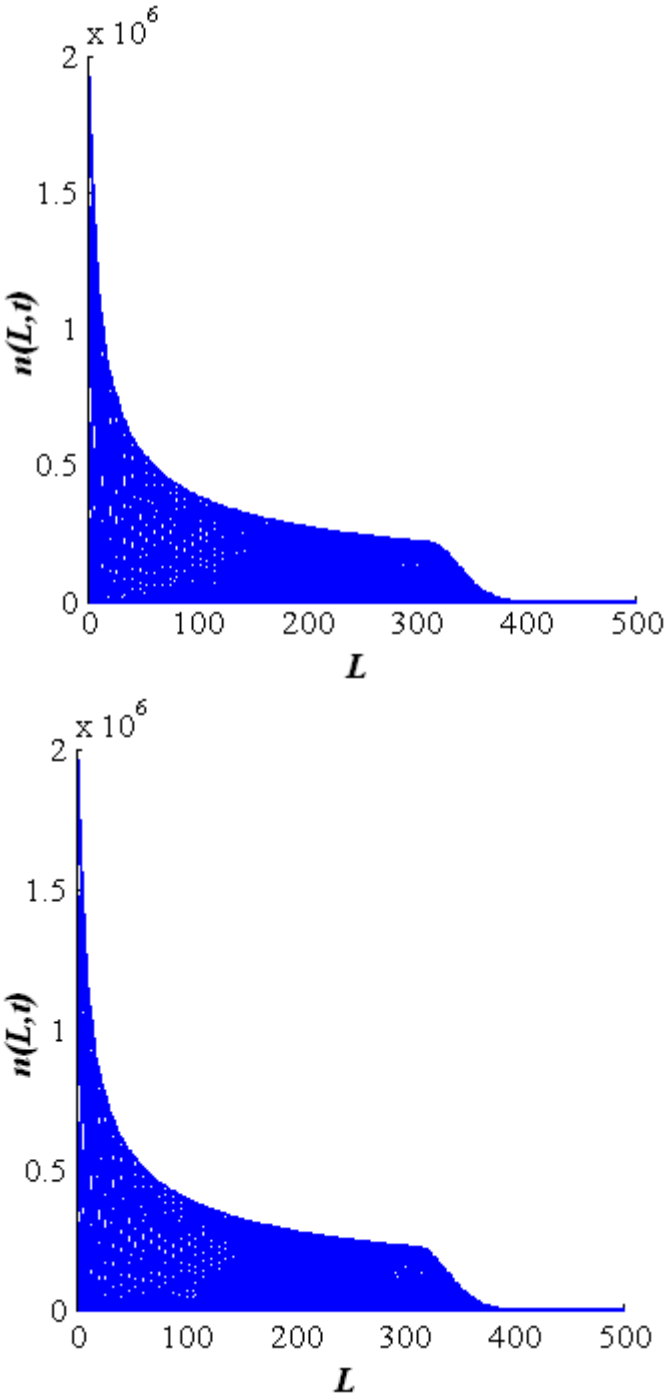

Figure 38. Simulation of the evolution of $n(L,t)$ shown every 2 min (top graph: moments method; bottom graph: finite-difference)

The same behavior, in other words, nucleation then growth, is observed in the actual experiments. In Figure 39, the population density was extracted from experiments using the FBRM (cooling rate of − 0.20 ºC/min), and was compared to the one predicted by the model. Considering that both methodologies give the same results, we here decide to use the moments method. t_0 is defined as the nucleation time, three different times after nucleation were considered: t_1 = 20 min, t_2 = 100 min and t_3 = 200 min. A parallel evolution in between model and simulation is observed, nonetheless the population density, even though close, do not agree. This is due to the assumptions made in establishing the model and the kinetics. As a reminder, G was assumed to be size-independent; we assumed no secondary nucleation, no agglomeration and no breakage. The results predicted provide a good guideline as to the evolution of the process through $\boldsymbol{n}(L,t)$ and the evolution of the concentration, C, in the slurry. Initially, the width of the distribution is narrower in the model than in the experimental results while later on it becomes comparable. We also note that for the model, the growth is constant and the peak evolves towards higher sizes. For the experiment we can see that it seems to follow the trend of the model but a slight difference is observed. This can be explained by the hypothesis we made regarding the modeling of the kinetics. We neglected possible breakage or agglomeration of the crystals. The combination of these hypotheses contributes to the differences seen in between predicted and actual evolution of the density.

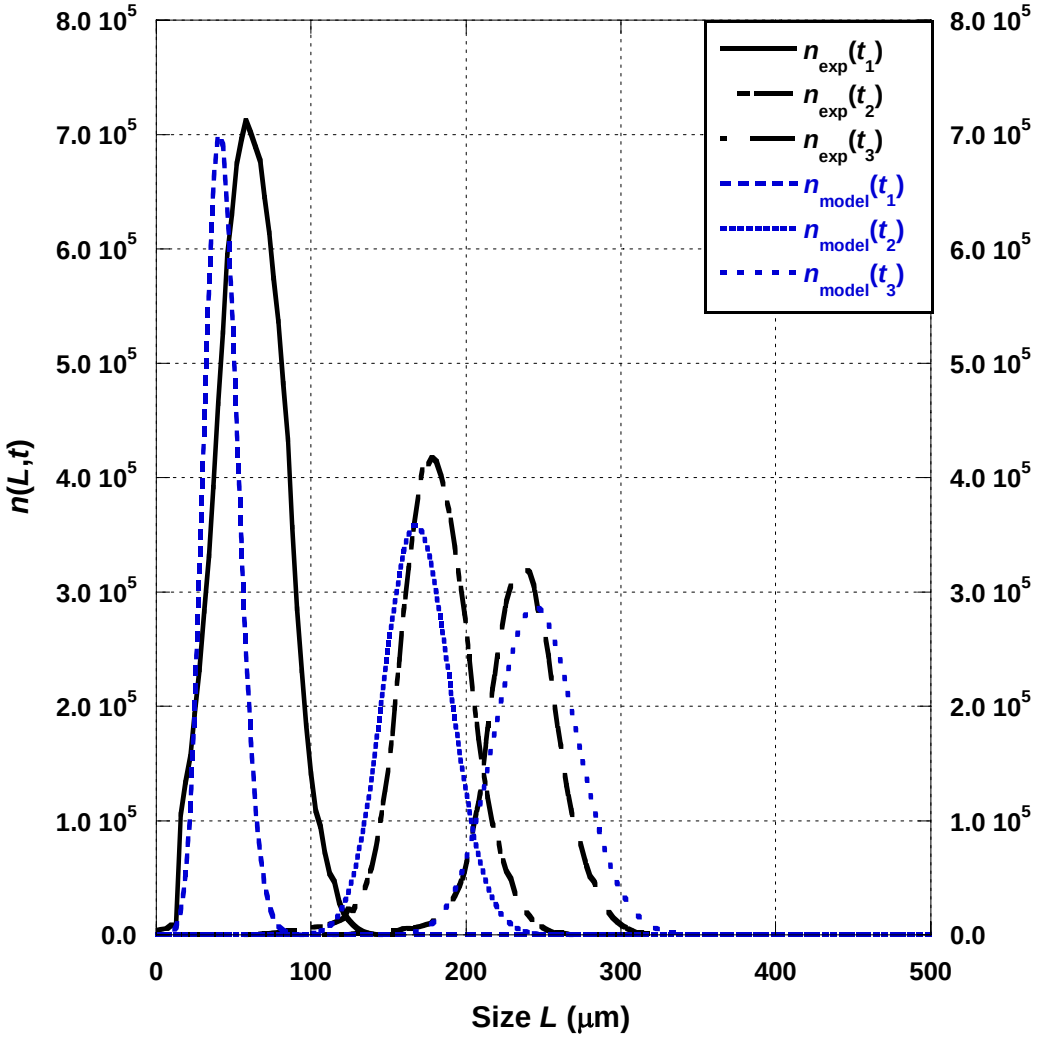

Figure 39. Comparison simulated vs. experimental $n(L,t)$ (t_1=20min, t_2=100 min and t_3= 200min)

An additional simulation of the run described in Chapter 5 is provided in Appendix D. The results are similar to the one described in this chapter.

Solving the population balance leads to the computation of the evolution of the population density versus time and the development of a predictive model. The predicted evolution was compared to the actual one, the model provides an accurate trend but with still some imprecision in the numbers. This error is due partly to the hypothesis made to

establish the growth and nucleation kinetics, to the fact that we neglected secondary mechanism and finally the error is also due to the method used to solve the population balance model such as the step size chosen in the finite difference method and the number of moments used in the methodology using the moments. Solving the population model provides the user with a predictive model on the evolution of $n(L,t)$. Such a model can lead to a better control of the process. Depending on the process, it might be essential to add a breakage and/or an agglomeration term in the population balance to provide better estimation of the process.

CHAPTER 7

OBSERVATION OF POLYMORPHIC TRANSITION

As polymorphic transformation has a large impact on pharmaceutical processes, monitoring this phenomenon constitute an essential complement to the investigation of the growth and nucleation phenomenon when it comes to fully understanding the crystallization process of a given system. In the present chapter, batch cooling crystallization of paracetamol from ethanol solutions is used as a model system for exploring the utility of Focused Beam Reflectance Measurement (FBRM) data in detection of the formation and transformations of polymorphs in-situ.

Polymorphism leads to significant variations in the physical properties of such crystals, as seen in Chapter 2. A slight modification in the crystallization process can produce a different polymorph, therefore, proficient control of such processes is necessary to ensure the quality and conformity of the end product. Consequently, being able to detect a polymorphic transformation in-situ would have great value (O'Sullivan et al. 2003, 2005).

Besides direct visual or microscopic observation, there is no technique to observe crystal shape. Since identification of polymorphism can be a challenge, even with off-line measurement techniques involving XRD, IR and Raman spectroscopy, NMR, and thermal analysis, it is no surprise that direct in-process observation of polymorphic transitions has been elusive. However, since a polymorphic transformation often is accompanied by a modification in crystal habit or shape, (Brittain 1999) use of this variable as an indicator of polymorphism may be feasible. In such instances visual or

microscopic observations, using a technique like Particle Vision Measurement (PVM) (Lasentec®), may hold promise, but these lack quantitative rigor. This chapter investigate the possibility to utilize the FBRM beyond its intended purpose, which is on-line monitoring of the evolution of a crystalline population, by extracting information about crystal shape and polymorphic transitions. FBRM measurements are highly dependant on the shape of the crystal, which means that it is reasonable to assume that a change in crystal shape can be monitored.

The FBRM has been used in coordination with PVM and Raman spectroscopy to investigate the polymorphic transformation of D-Mannitol (O'Sullivan et al. 2003). Similar studies have also been run on the transformation of L-glutamic acid with additional information on the concentrations profile provided by attenuated total reflection Fourier transform infrared spectroscopy (ATR-FTIR) (Schöll et al. 2006). Based on these studies, the structurally sensitive information given by the Raman spectroscopy appears to be necessary and the FBRM was simply used to monitor the evolution of the total chord counts. In contrast, the present study illustrates how the FBRM, combined with a model, can be used to gain insight on the polymorphic transition and track a change in crystal shape without relying on additional instruments. This provides the advantages of less complex experimental protocol and the use of fewer expensive instruments.

The present work used batch cooling crystallization of paracetamol from ethanol solutions as a model system for exploring the utility of FBRM data in detection of the polymorphic transition. As a reminder, paracetamol (acetaminophen) is known to exist in three polymorphic forms (Beyer 2001). Note that, the shape of paracetamol crystals

change with transition from Form II (needles) to Form I (octahedral), and therefore fulfills the proposed requirement to use FBRM to detect a polymorphic transition.

As Form II crystals undergo plastic deformation during compression, they are easily compressed into tablets, and there have been efforts to synthesize and retain this particular polymorph (DiMartino et al. 1996, Sun and Grant 2001, Nichols and Frampton 1998). It has been shown that under certain experimental conditions, Form II can be produced at a lab scale, but the crystals have to be harvested relatively early after nucleation to prevent solvent-mediated transformation, thus strongly limiting their growth (Al-Zoubi et al. 2002, DiMartino et al. 1996, Nichols and Frampton 1998). A better understanding of this transition, enabled by in-situ FBRM measurements, could aid in developing a more efficient process for making Form II paracetamol.

7.1 Influence of crystal shape

As seen in Chapter 3, the relationship between the length-weighted population density $\boldsymbol{n_1}$ and the chord-length density $\boldsymbol{q}$ is defined by

$$\boldsymbol{q} = \boldsymbol{\Psi} \boldsymbol{n}_1, \tag{90}$$

where $\boldsymbol{\Psi}$ is a conversion matrix relating the two vectors, $\boldsymbol{n}_1$ and $\boldsymbol{q}$, which describe the densities. With the determined matrix $\boldsymbol{\Psi}$, which is a function of the shape of the crystals, the CLD corresponding to a specific crystal population density can be estimated.

The two polymorphic forms of paracetamol considered here have different crystal shapes: Form I crystals are octahedral and Form II crystals are needle-like. Accordingly, it is anticipated that two identical population densities, each comprised of one of the polymorphs, would lead to greatly different chord-length densities, and FBRM

measurements of the chord-length densities should have significantly different characteristics. This outcome would provide a tool for observing a transition from one form to another with the FBRM.

Three crystal populations, one from each considered shape, were analyzed to show more clearly the effect of shape on chord-length distribution. To make the outcomes comparable, all particles were specified to have the same volume and the dimensions for each category were defined in terms of a single variable: the edge of an octahedron and the short edge of a slab and of a needle. A chord-length distribution was calculated for each shape assuming a single crystal size. The volume of the crystal was kept constant, 3.456×10^{-11} m^3, in going from one shape to another and the dimensions of the crystals were derived after first defining the aspect ratio for a slab as 5:1 and for a needle as 20:1. Therefore, for an octahedron, the edge was 418.53 μm; for a slab, the base edge was 190.49 μm; for a needle, the base edge was 120 μm.

The chord-length density $\boldsymbol{q}$ for each of the crystal shapes was calculated as previously described, and the results are shown in Figures 2 through 4. Clearly, $\boldsymbol{q}$ has a functional dependence on shape, and the difference between octahedrons and needles is significant. Two important changes in the distribution are the standard deviation, which is a measure of spread, and the skewness, which is an indication of a lack of symmetry; in going from octahedral to slab to needle, the standard deviation decreases and the skewness increases as shown in Table 1. We use the definition

$$\text{Skewness} = \frac{\mu_3}{\sigma^3} \tag{91}$$

where μ_3 is the third standardized moment, and σ is the standard deviation of the distribution $\boldsymbol{q}$.

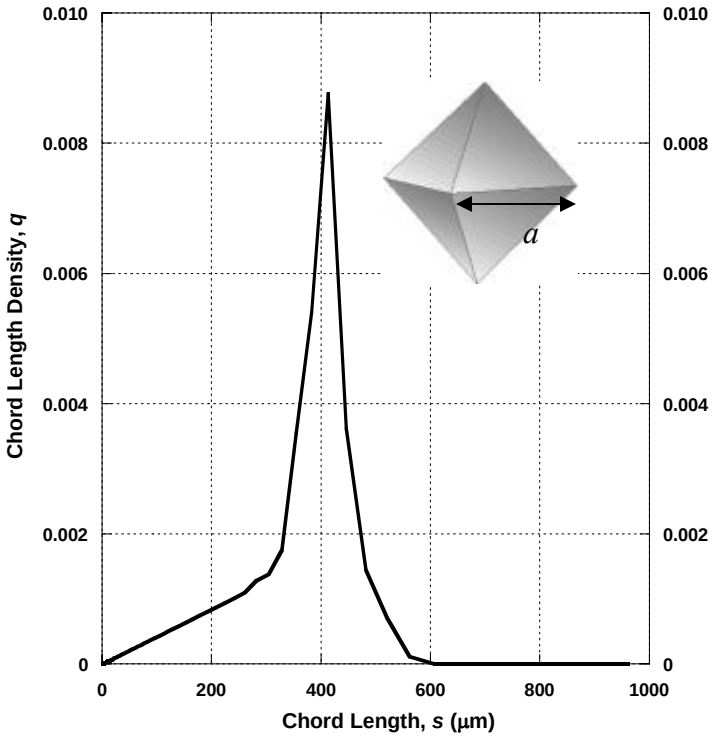

Figure 40. Calculated normalized chord length density for octahedrons (a = 418.5 μm)

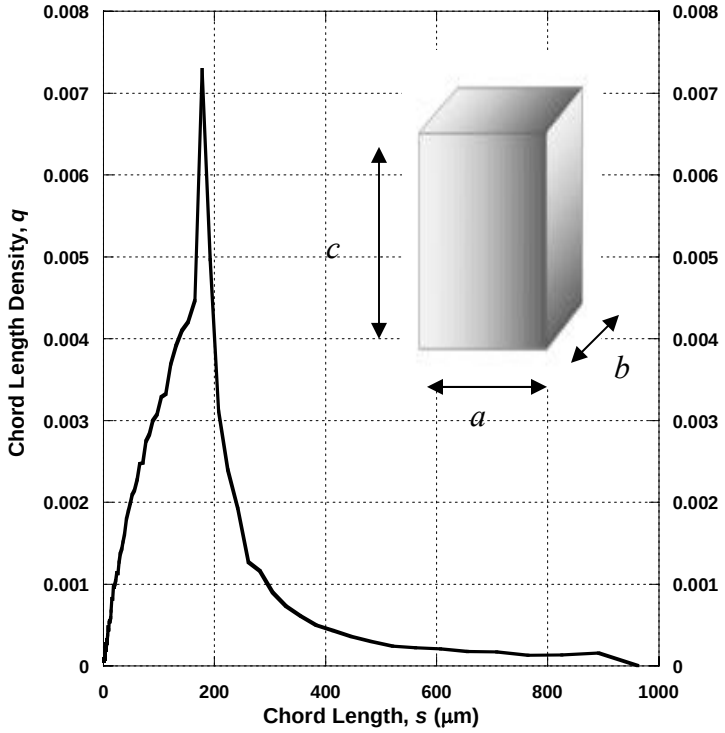

Figure 41. Calculated normalized chord length density for slabs (a = b = 190.5 μm and c = 5a)

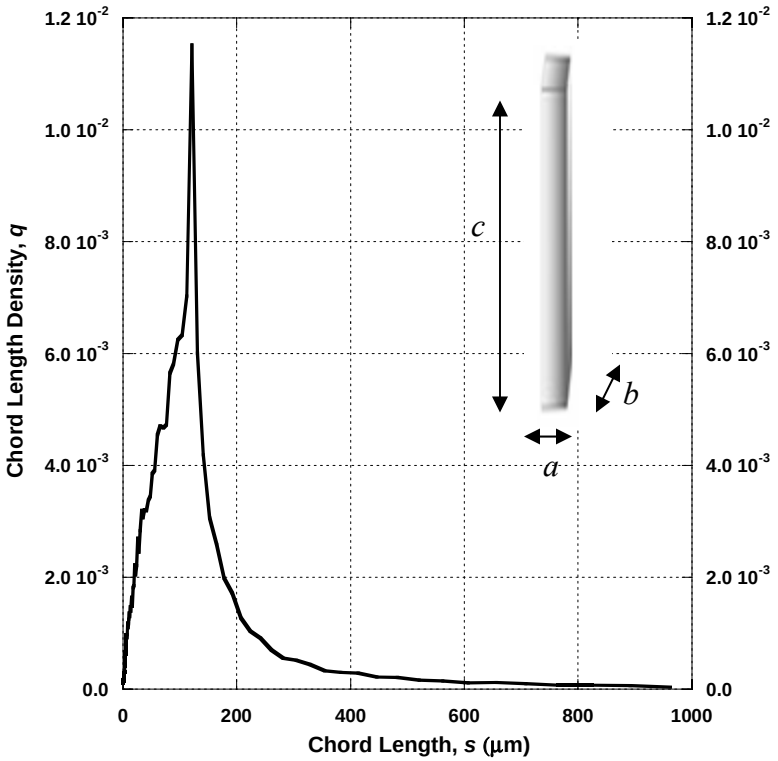

Figure 42. Calculated, normalized chord length density for needle-like crystals (a = b = 120 μm and c = 20 a)

Table 10. Characteristics of the chord-length densities

	Octahedron	Slab	Needle
L mean	368.3	216.8	158.7
σ^2	9247.7	28236.7	22009.3
Skewness	-1.22	2.04	2.74

These results show that a change in crystal shape, while holding crystal volume constant, leads to significantly different chord-length densities. The calculated density functions were different in form as well as in the location of characteristic maxima. It may therefore be expected that the polymorphic transition from a population of slabs to a population of octahedrons would be marked by a change in the overall observed chord-length density. This was examined by estimating chord-length densities for each of three

different crystal shapes (octahedrons, slabs, and needles) comprising the crystals in a fixed population density, which in this case was defined as following a gamma distribution. The gamma distribution chosen as an example is defined by:

$$\boldsymbol{n}_1\left(\bar{L}_i\right) = \gamma\, \bar{L}_i^{\beta\text{-}1} \frac{e^{-\bar{L}_i/\theta}}{\Gamma(\beta)\theta^{\beta}} \tag{92}$$

$$\Gamma(\beta) = (\beta - 1)! \tag{93}$$

where β is a shape factor, θ a scale parameter and γ a normalizing coefficient. In the present work, the parameters were selected so that L_{mode} = 400 μm (β = 9, θ = 0.5 and γ = 0.01). L is the characteristic size of the crystal, here, it is the equivalent diameter.

The resulting $\boldsymbol{q}$ for the three shapes are shown in Figure 43. The evolution of the standard deviation and the skewness show important changes in the distribution; in going from octahedral to slab to needle, the standard deviation decreases by a factor of 2.5 and the skewness increases by a factor of 10.

Like the results with a single crystal size, these outcomes are a further indication of promise in using FBRM measurements to observe transitions from one crystal shape to another. That promise is especially significant when the change in shape is from octahedral to needle, and therefore the transition of paracetamol from Form I to Form II is a good test case.

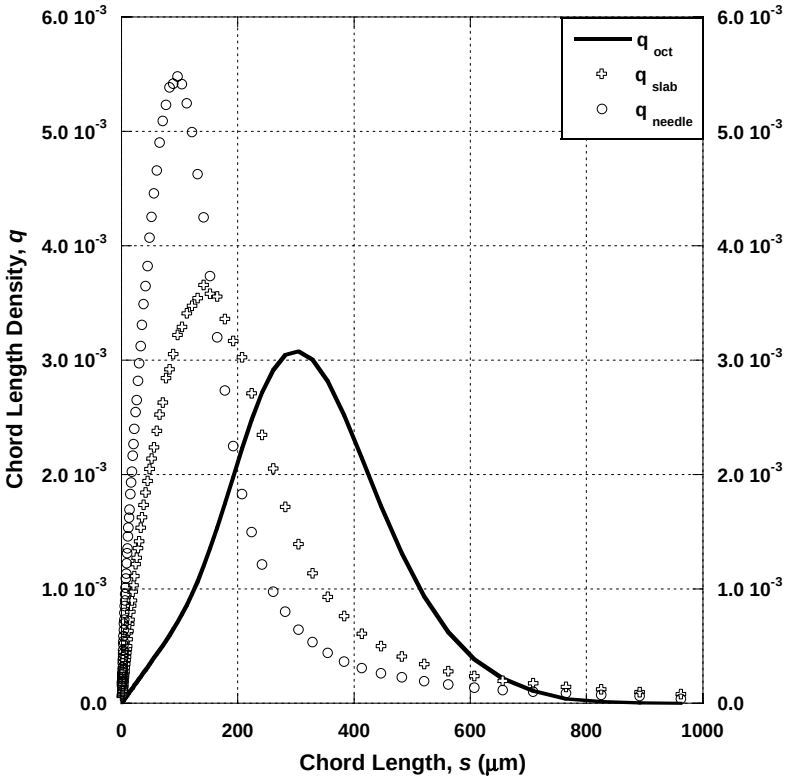

Figure 43. Overall chord length densities for the same population density (gamma distribution) but for different crystals shapes

Table 11. Characteristics of the chord-length densities

	Octahedron	Slab	Needle
L_{mean}	326.6	234.0	168.2
σ^2	18081.5	31281.1	23631.1
Skewness	0.39	1.71	2.41

7.2 Experimental protocol

The primary unit was the same as the one described in Chapter 5. In a typical run, the solute and solvent (~34 wt % paracetamol, ~66 wt % solvent) were added to the crystallizer and the resulting solution was heated to 70 ºC, which insured complete dissolution of the crystals. Different solvents were used in the experiments and these will

be described later in this chapter, under the experimental results section. The data acquisition was started and the crystallizer contents were cooled at a pre-determined linear rate from 70 ºC to 5 ºC. The system was held at 5 ºC until equilibrium between the solution and the generated crystals was reached. Six runs were done at each set of conditions, which demonstrated that the results were reproducible. Three of them were used to monitor the evolution of the chord counts and were reproducible within 7 %, while the other three were used for sampling so the evolution of the chord counts was not disturbed by the sampling process.

To determine which polymorphic form was in the system, samples of the crystals were taken at representative times after nucleation, which was identified by a sudden increase in the chord counts detected by the FBRM as seen in Figure 44. Samples were taken until steady state was achieved. The collected crystals were deposited immediately onto a thin microscope slide and examined with an optical microscope.

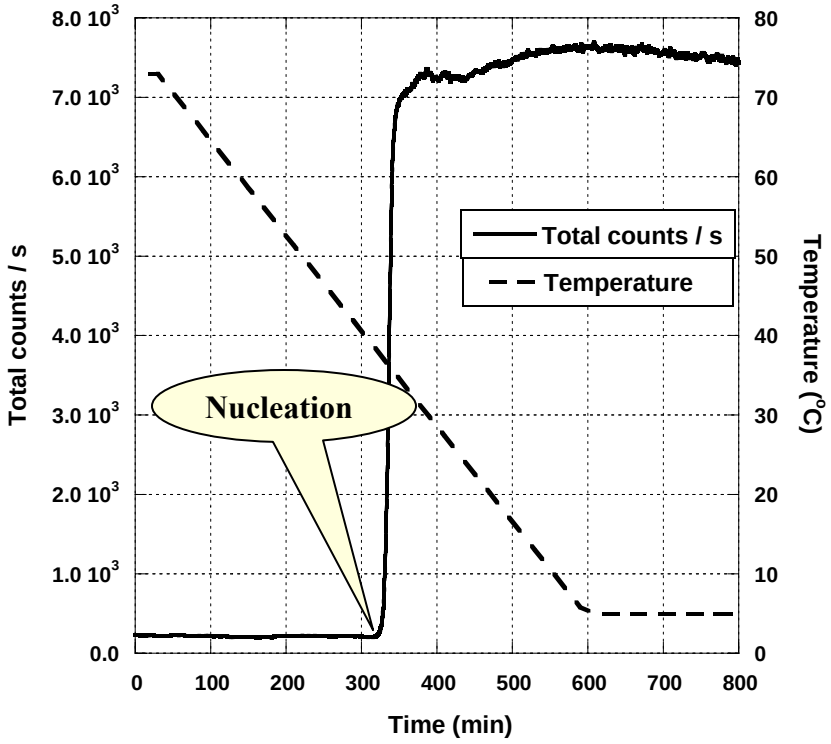

Figure 44. Evolution of the total number of chord counts and temperature vs. time for crystallization of paracetamol from ethanol at a cooling rate of – 0.10 °C/min.

7.3 Experimental results

Initial experiments were performed using pure ethanol as a solvent. Cooling was at a rate of – 0.10 ºC/min, and the general procedure followed was as described above. Figure 45 shows the evolution of chord counts in several size ranges for a run in which samples were taken at the indicated times. Nucleation was identified through a rapid increase in chord counts, and steady state was defined to have been reached when the chord counts became constant. Photomicrographs of the crystal samples, shown in Figure 46, were taken during three stages: (b) at nucleation, (c) during growth of the crystals and (d) when steady state was reached. None of these show evidence of a polymorphic transition; only the octahedral shape of Form I was seen from the point of nucleation

through steady state. Another photomicrograph (a) was taken before nucleation to verify the absence of crystals.

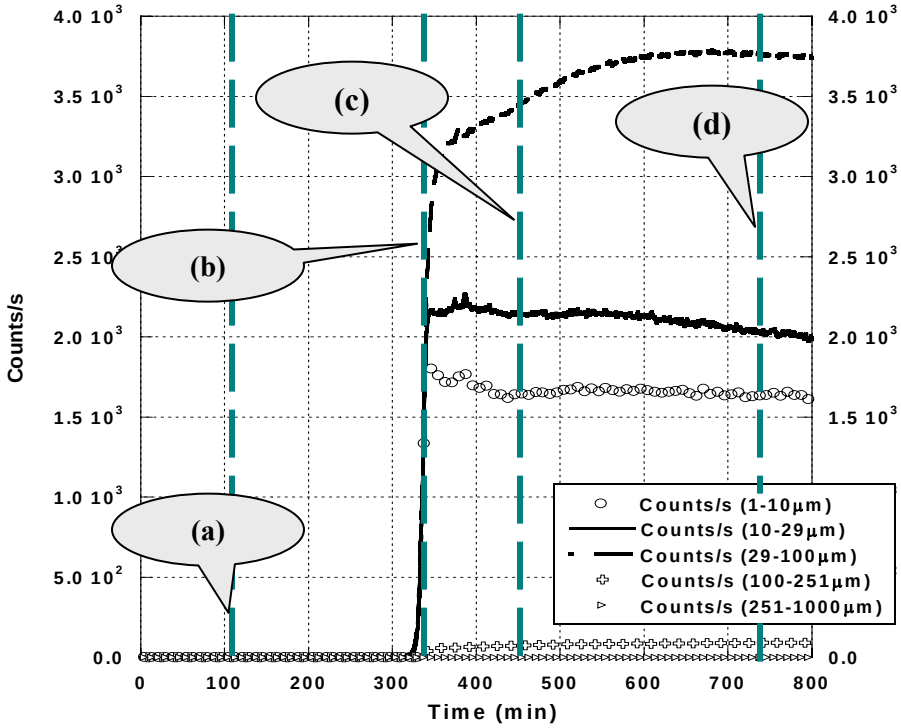

Figure 45. Evolution of the chord counts vs. time for crystallization of paracetamol from ethanol at a cooling rate of – 0.10 °C/min.

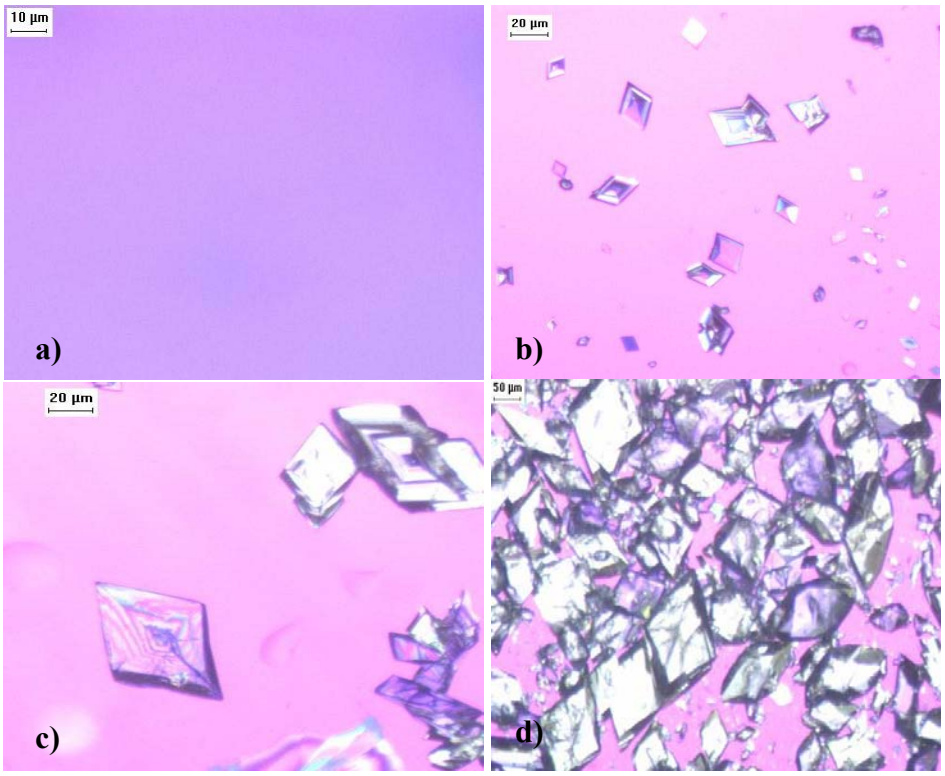

Figure 46. Photomicrographs of octahedral crystal samples taken at times indicated in Figure 45.

Further experiments established, that both Forms I and II were nucleated upon batch cooling of a paracetamol-ethanol solution at a cooling rate – 0.50 ºC/min. This was established through observation of the corresponding micrographs. Form II disappeared shortly after nucleation as it underwent what is thought to have been a solution-mediated transformation, as identified by Al-Zoubi and co-workers (Al-Zoubi, 2002), and left an end-product that was uniformly Form I.

In order to facilitate observation of a clear polymorphic transition, the experimental conditions were slightly altered to favor the formation of the kinetic product (Form II). This was done, as suggested by Nichols and Frampton (1998), by modification of the solvent (ethanol + 5 % methanol instead of pure ethanol) and higher cooling rate (– 1.0 ºC/min). Methanol was added to increase the solubility of the paracetamol-solvent

system, to favor the nucleation of Form II. The goal was to nucleate mainly Form II, which should provide a clearer view of the transition from Form II to Form I. Chord counts were tracked for such a run and are shown in Figure 47. Also shown on the figure are the times at which samples were taken for microscopic examination. Again, the onset of nucleation is shown clearly, but unlike the previous experiments, the chord counts in the smaller bins drops significantly shortly after nucleation, before finally increasing again and then becoming constant. The evidence to be presented indicates that this behavior reflects a transition in the crystal morphology as it goes from Form II (manifested in needle-like crystals) to Form I (octahedral crystals).

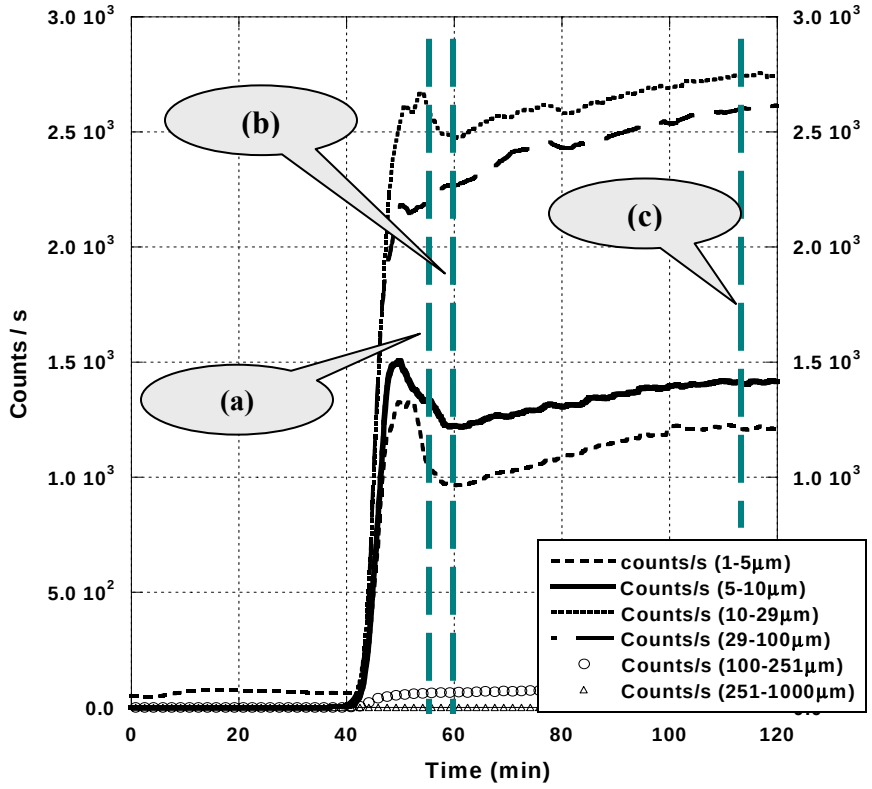

Figure 47. Evolution of the chord counts vs. time for a cooling rate of –1.0 °C/min, solvent: ethanol + 5 % methanol

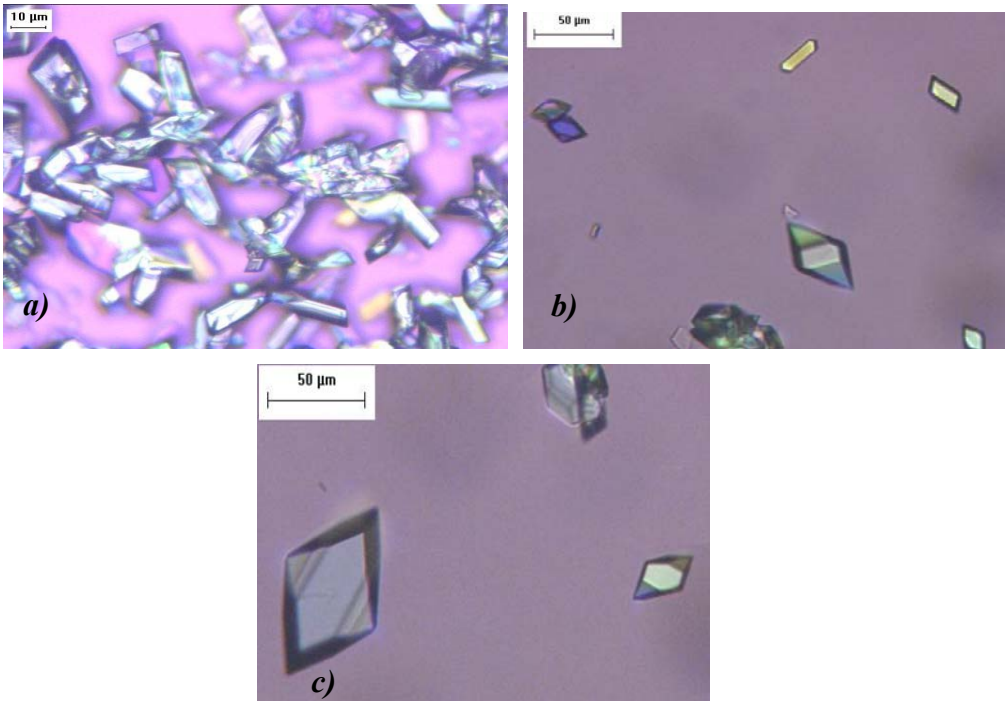

Figure 48. Photomicrographs of paracetamol crystals in samples taken as indicated in Figure 47.

Photomicrographs of samples of the crystal population at various times are shown Figure 48. Figure 48(a) was taken shortly after nucleation; the crystals are seen to be of a needle-like shape, indicating the nucleation of Form II crystals. Several minutes later, as shown in Figure 48(b), octahedral and needle-like crystals are observed, indicating the partial transition from Form II (orthorhombic, needle-like crystals) to Form I (monoclinic, octahedral crystals). In 10(c), which is of a sample taken at equilibrium, only octahedral crystals are visible, indicating that Form II crystals have disappeared completely and the final product is uniformly Form I. As noted in Figure 47, the polymorphic transformation was accompanied by a decrease in counts of smaller chords, and it is postulated that the change in crystal habit caused this decrease. By going from needles to octahedrons there were a reduced number of small chords detected; this feature was attributed to the change in crystal habit.

Figures 11 and 12 show chord-length density plots for the two runs described above: that is, without and with polymorphic transition. Differences in the shape of the distribution as well as in the evolution with time are clear. Consider first the chord-length densities soon after nucleation in the two systems. In Figure 11 only Form I is nucleated and the shape of the plot is smooth; on the other hand, the plot in Figure 12, which is from a run in which Form II nucleation dominated, has a considerably different shape. It seems highly likely that the irregularities in the latter instance are due to existence of multiple shapes in the system. Also note how the chord-length densities evolve in the two cases. In the first, the progression is rational as the original population simply matures (grows) during the run. In the second, however, more seems to be happening; it is likely

that the observation is reflective of at least two phenomena: one, the growth of crystals and, two, a transformation from a population dominated by needle-like crystals to one having the characteristics of octahedral crystals show in Figure 49.

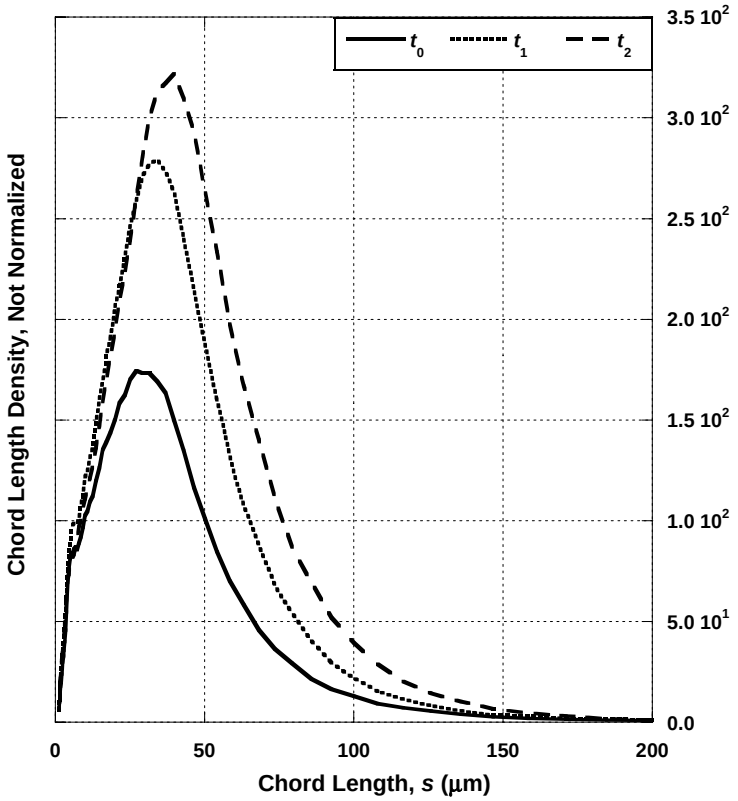

Figure 49. Evolution of the chord length density for crystallization of paracetamol from ethanol at a cooling rate of –0.10 °C/min.(t_0 = nucleation, t_1 = nucleation + 100 min, t_2 = steady state). Note that the CLD has not been normalized.

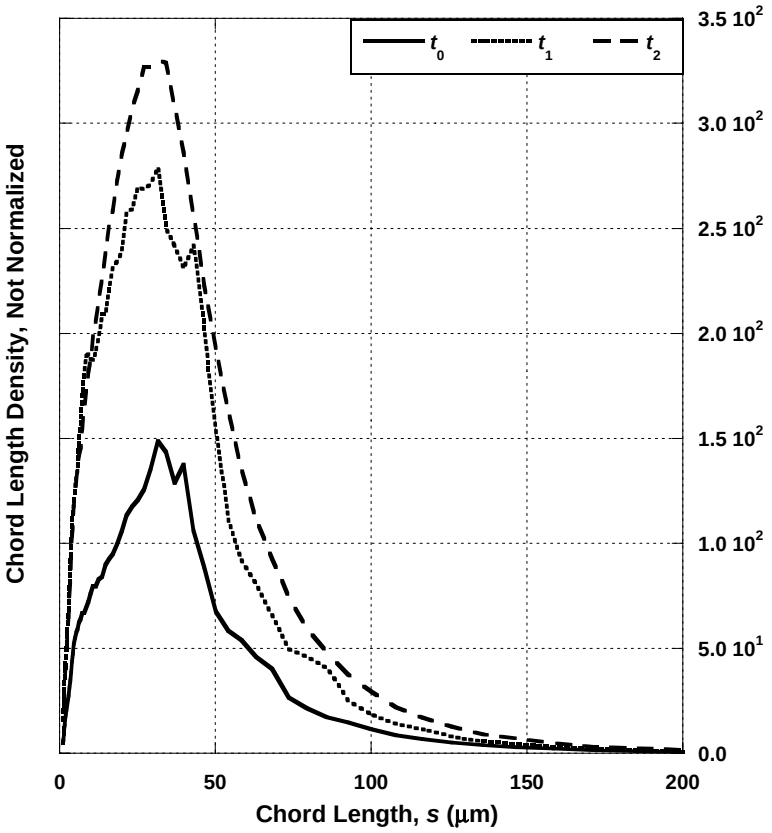

Figure 50. Evolution of the chord-length density for crystallization of paracetamol from a solution in ethanol and 5 % methanol at a cooling rate of – 1.0 °C/min. (t_0 = nucleation, $t_1 = t_0 + 10$ min, t_2 = steady state). Note that the CLD here has not been normalized.

7.4 Conclusion

The qualitative and quantitative characteristics of chord-length density functions have been evaluated for octahedral, slab-like, and needle-like crystals. These characteristics differ measurably among the shapes investigated for a single crystal and for a population of such crystals. Such variations have been used to characterize hypothetical unknown distributions, thereby ascertaining crystal shape. In cases where different polymorphs result in different shapes, these outcomes can be used to determine the occurrence of a polymorphic transition; i.e., the evolution from one crystalline population to another can be followed through the evolution of the shape of the overall chord-length density function, making the polymorphic transition observable through FBRM measurements.

Batch cooling crystallization of paracetamol from ethanol and methanol-ethanol solutions was used as a model system for exploring the utility of FBRM data in detection of the formation and transformations of polymorphs. Our experiments found that both Forms I and II were nucleated upon batch cooling of a paracetamol-ethanol solution. However, Form II disappeared shortly after nucleation as it underwent a solution-mediated transformation and left an end-product that was uniformly Form I. By varying the crystallization conditions, it was possible to induce nearly exclusive nucleation of Form II. Tracking the chord-length distribution of the resulting crystal population made it possible to monitor the transition from Form II to Form I. As the two forms have significantly different crystal habits, the generated chord-length densities, which are a function of the shape, are dissimilar and allowed the detection of the transition from one

form to the other. The transition was confirmed by following its progress through image analysis of samples removed from the generated crystal population.

In short, we have shown that tracking the chord-length density of a crystal population makes it possible to monitor polymorphic transitions when they are accompanied by a change in crystal habit. The FBRM provides in-situ and real-time information on the system evolution and can efficiently track qualitative changes in particle population. Nonetheless, a model taking into account the possibility of coexistence of several shapes is essential to link the chord length density to the population density and to fully model the polymorphic transformation.

CHAPTER 8

CONCLUSION AND RECOMMENDATIONS

8.1 Conclusions

The purpose of this research was to develop a new methodology that would provide real-time information on the evolution of the crystallization process based on on-line FBRM measurements. This work showed how information on kinetics, solubility, supersaturation, population density and polymorphism could be extracted from FBRM measurements.

First, a mathematical model was developed to quantify the relationship between chord length and population densities. This study focused on octahedral crystals as the model system was chosen to be paracetamol in ethanol solutions, the general methodology developed here can be applied to a wide variety of crystals shapes. The restoration of the population density from the chord length density required the estimation of a conversion matrix which was specific to the geometry of the considered crystals. Once this relationship was fully defined, we focused on investigating the degree of confidence that could be given to the restoration process and which aspects of the population density could accurately be estimated. To complete this work, the sensitivity of the method to noise in data, to inherent confounding measurements, or to shape variations was also investigated. It was shown that the developed methodology offered an accurate and constraint-free restoration of the population density from FBRM measurements.

It was established that the spectral method used here could be efficiently applied to a wide range of non-spherical particle shapes, as well as to multimodal and sharp population density functions. Note that, the accuracy of the proposed method is strongly limited by the geometry of the considered population, for example, as needles get thinner, the restoration of the population density for the lower size ranges becomes more challenging. It is interesting to notice that the small size range features are more difficult to estimate because all crystal sizes contribute to small chord counts while only larger ones generate large chord counts. This study showed that extreme oscillations could occur in the smaller size ranges during the restoration process and also that those size ranges were more sensitive to noise, thus making it harder to effectively estimate those specific populations. A solution to this issue was proposed through the application of a limited smoothing of the restored density when needed.

The estimation of the population density n was also limited by the presence of noise in the chord-length density measurements. It was established that increasing the data acquisition time frame had the consequence of powerfully reducing the noise level. The data presented in this work showed that when dealing with octahedral shaped crystal, increasing the data acquisition time frame to 30 s was enough to reach acceptable noise level. It was established that, the precision of the restoration was a function of the crystals shape; as a consequence, when dealing with other shapes, the chosen data acquisition time frame has to be adapted. The method developed here, provided an alternative way to estimate population density from FBRM measurements, but it also provided us with tools for the analysis; specifically, the analysis can help tailor the FBRM settings of number of bins, size distribution of bins, and integration time, for the particular crystal

shape and distribution function appropriate to a particular process. Furthermore, the presented methodology has great potential to be the basis for a control scheme that manipulates the population density produced from FBRM raw data.

The next step was to use this model to investigate the kinetics of the system. It was established that the FBRM technology allows on-line monitoring of the chord length density which leads to an estimation of the evolution of $\boldsymbol{n}_1$. The population density is related to the number population density, hence once $\boldsymbol{n}_1$ is known the estimation of $\Delta \boldsymbol{N}$ is straight forward. This work showed how being able to estimate the evolution of the number population density versus time led to the estimation of the mass crystallized and the supersaturation, ΔC. Considering that ΔC is the driving force behind growth and nucleation phenomena, both kinetics were related to the supersaturation and quantified through a data fit of the model derived from FBRM data. This research led to the development of tools allowing the estimation of growth and primary nucleation kinetics for the considered system. It also provided an alternative way to monitor the evolution of the supersaturation.

The model system being paracetamol in ethanolic solution, the growth and nucleation kinetics of this system were established through a model fit of the data. The comparison between literature data, experimental evolution, and modeled prediction of the kinetics and the supersaturation led to the conclusion that the method provided an accurate estimation of the evolution of the system. This method can be applied to other systems providing the knowledge of the shape of the crystals, as well as some general information on the solute and solvent such as density for example.

The results from the experiments aiming at determining the kinetics of the system showed how a seeded crystallization was implemented and how nucleation and growth kinetics of the system were extracted from chord length measurements.

The growth and primary nucleation kinetics were then used to fully define the population balance model. This set of coupled differential equation involving the concentration, C, and the population density, n, was solved using two different methodologies: finite difference method and moment transformation method. The resolution of the population balance model led to the computation of the evolution of the population density versus time, $n(L,t)$, and the concentration, $C(t)$. This set the basis for the development of a predictive model. The predicted evolution of both n and C was compared to the actual one. It was shown that both resolution methods led to similar results and that the model provided an accurate trend, nonetheless, some imprecision in the numbers was noticed. This difference was attributed to the hypothesis made. The error source is especially due to the fact that we assumed a temperature independent growth kinetic constant, due to the use of the formula given by Mersmann (1990) to estimate the interfacial tension in the nucleation kinetic term and also, we neglected agglomeration, breakage and secondary nucleation. Such a model can presently be used to estimate the evolution of n but could be expected to lead to a better control of the process through higher accuracy of the estimation of the process parameter.

As polymorphism is a large aspect in the crystallization of organic compounds, some attention was given as to how the FBRM can be used to track such a transition. The characteristics of chord-length density functions were estimated for octahedral, slab-like, and needle-like crystals. It was shown that these characteristics differed significantly

among the various shapes investigated, and those differences could be used to characterize unknown distributions. When polymorphic transition is accompanied by a change in crystals shape, it was established how the distribution characteristics could be used to follow polymorphic transition. In other words, by monitoring the evolution of the overall chord-length density function, it was proven possible to monitor the evolution from one crystalline population to another, hence making the polymorphic transition readily observable through FBRM measurements.

Batch cooling crystallization of paracetamol from ethanol and methanol-ethanol solutions was used as a model system. It was found that both Forms I and II of paracetamol crystals were, under given experimental conditions, nucleated upon batch cooling of a paracetamol-ethanol solution. However, the metastable Form II was found to disappear shortly after nucleation leading, through a solution-mediated transformation, to an end-product that was uniformly the stable Form I. It was also found that by varying slightly the experimental conditions such as solvent composition, we could induce nearly exclusive nucleation of Form II. It was then shown how the transition from Form II to Form I could be tracked through the monitoring of the chord-length distribution. The transition was visually confirmed through image analysis of the crystals formed, a transition from needle like crystals (Form II) to octahedral crystals (Form I) was observed.

The FBRM provided in-situ and real-time information on the system evolution such as, population density, kinetics and supersaturation and can also efficiently track shape changes in the crystalline population. The FBRM measured chord length densities can be related to phenomenon such as growth and nucleation, through the appropriate

models. The proposed methodology can be used as a basis for the development of efficient control tool applicable to the crystallization process.

8.2 Recommendations

The development of a predictive model is important as it can be a strong tool in the control of the crystallization process. The research presented here shows the possibility of developing such a tool by showing how the necessary components, such as growth kinetics for example, can be obtained from FBRM data. Nonetheless it would be interesting to complete this study by investigating phenomenon such as agglomeration or breakage into the population balance model. Even though considered negligible in this study, those assumptions cannot always be made and in the aim to generalize the model including those phenomena in the population balance model would lead to more accurate and universal control scheme.

The methodology can also benefit from investigating the temperature dependence of the growth rate and by validating the results obtained by the models through experimental techniques such as the direct measurement of the concentration. This would also provide interesting data on the sensitivity of the proposed methodology.

Another aspect of this work referred to polymorphism. It has been shown that the FBRM can be a useful tool when detecting polymorphic transitions. It is interesting to note that, there is limited literature regarding the modeling and monitoring of this transition, hence developing a model taking into account the possibility of coexistence of several shapes in the slurry would be an interesting follow up to this research. It would

then enable the user to fully model the polymorphic transformation and it would also make possible the application of the proposed methodologies to multi-component and multi-shaped systems.

Finally, the determination of the general applicability of this research would call for further validation. This would be realized through a similar study of other systems which present different crystal shapes. Those complementary studies could lead to a successful application of the proposed tools for control and monitoring purposes to a wide range of systems.

APPENDIX A

SENSITIVITY OF THE MODEL
- ADDITIONAL GRAPHS -

Gamma Distribution - Slab like crystals (Aspect ratio 1:1:5): m′ = 54

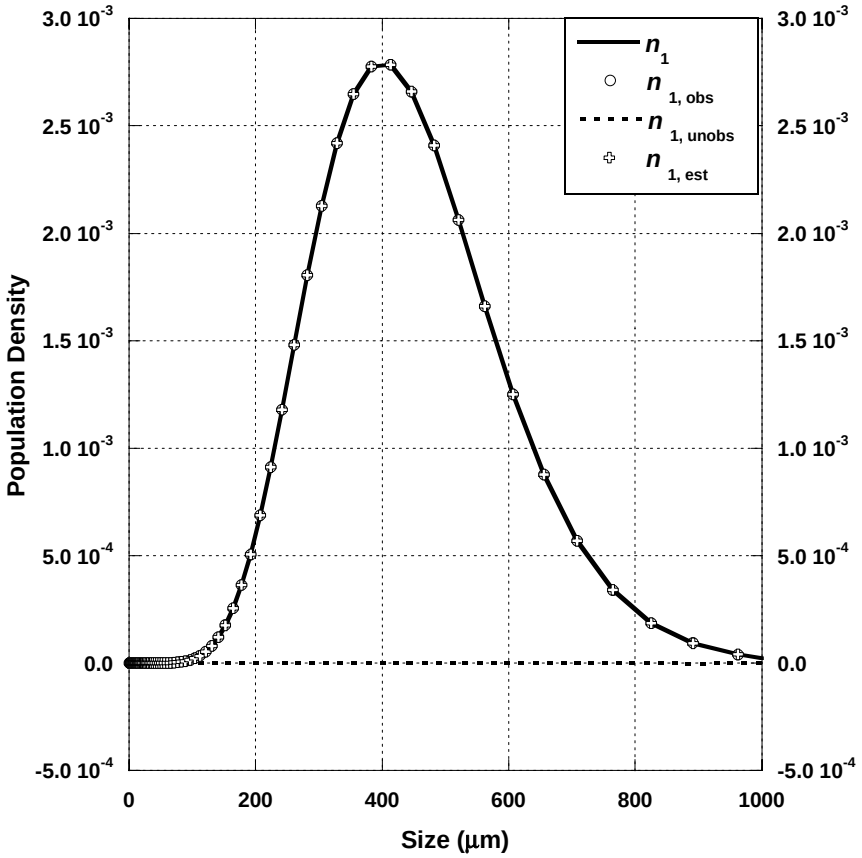

Figure 51. Projection of n_1 onto observable and unobservable subspaces and recovered population density through the spectral method for a slab shape

Gamma Distribution - Needle-like crystals (Aspect ratio 1:1:20): m′ = 37

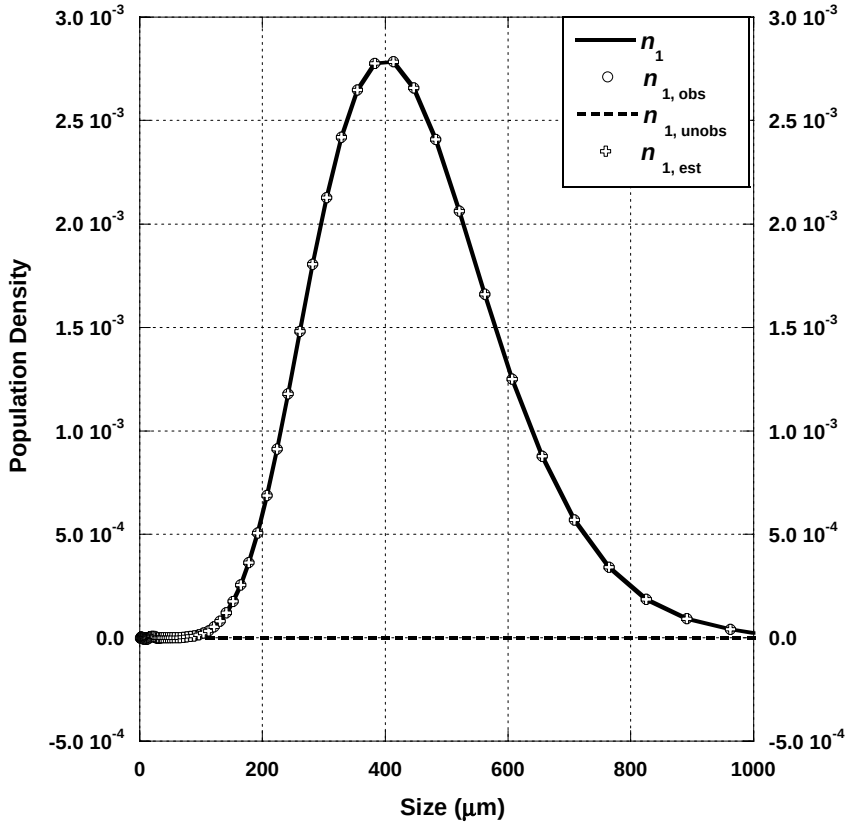

Figure 52. Projection of n_1 onto observable and unobservable subspaces and recovered population density through the spectral method for a needle shape.

Bimodal distribution- Slab like crystals (Aspect ratio 1:1:5): m′ = 21

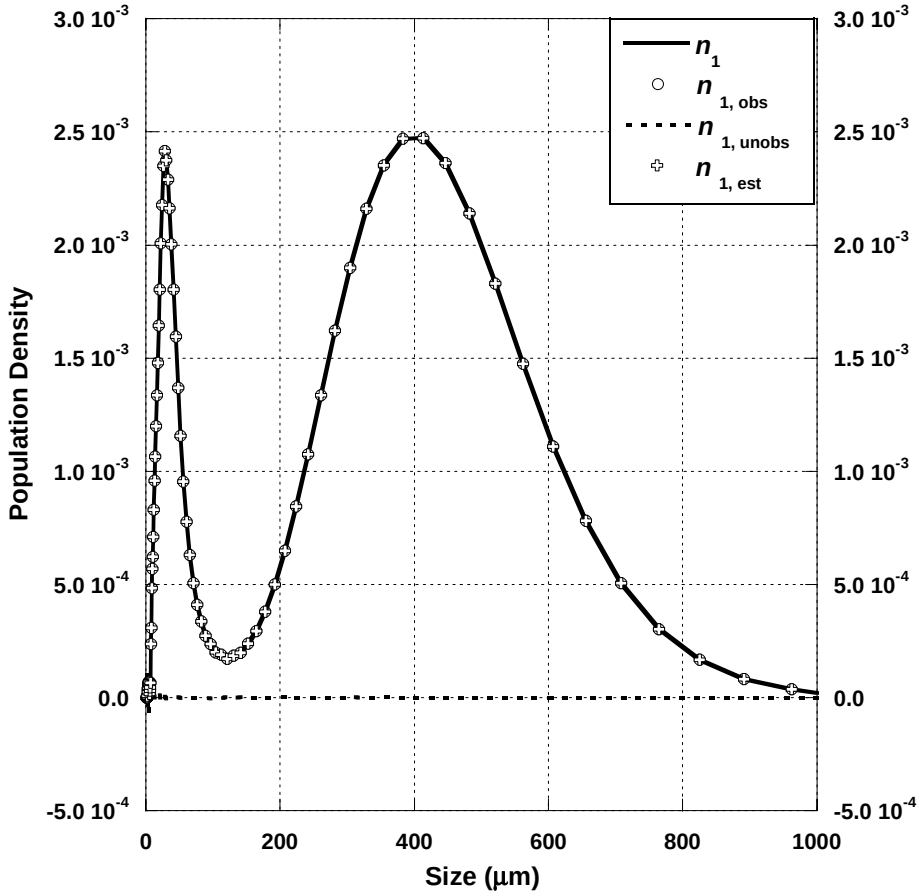

Figure 53. Projection of n_1 onto observable and unobservable subspaces and recovered population density through the spectral method for a slab shape

Bimodal distribution - Needle like crystals (Aspect ratio 1:1:20): m′ = 18

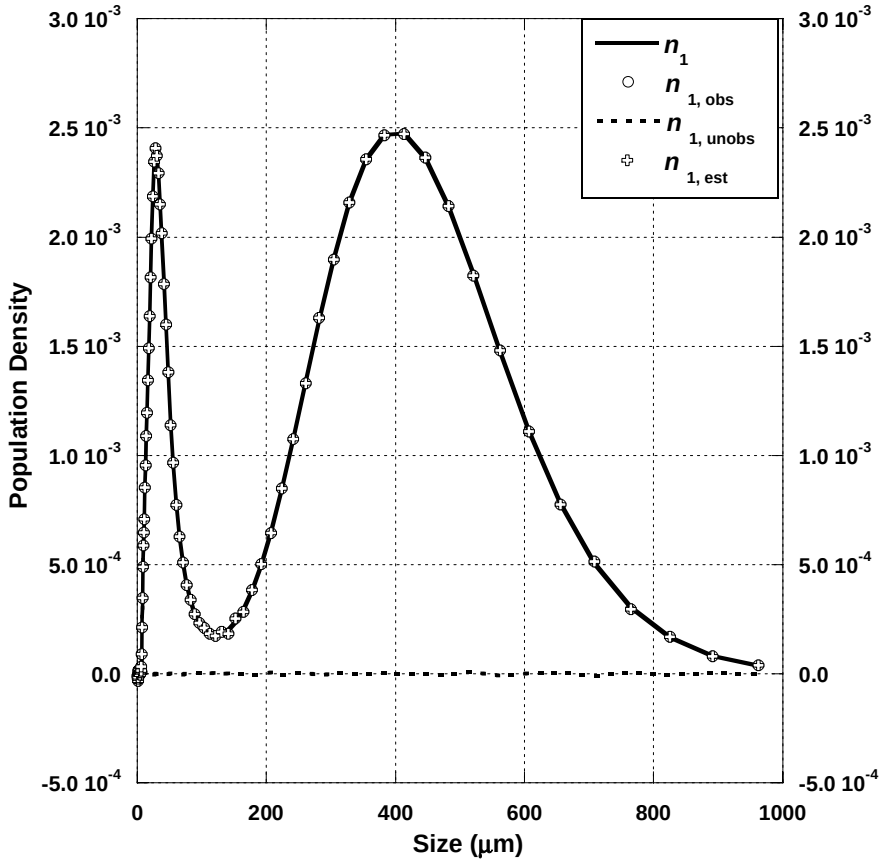

Figure 54. Projection of n_1 onto observable and unobservable subspaces and recovered population density through the spectral method for a slab shape.

Bimodal distribution- Noisy distribution - Octahedral crystals: m′ = 58

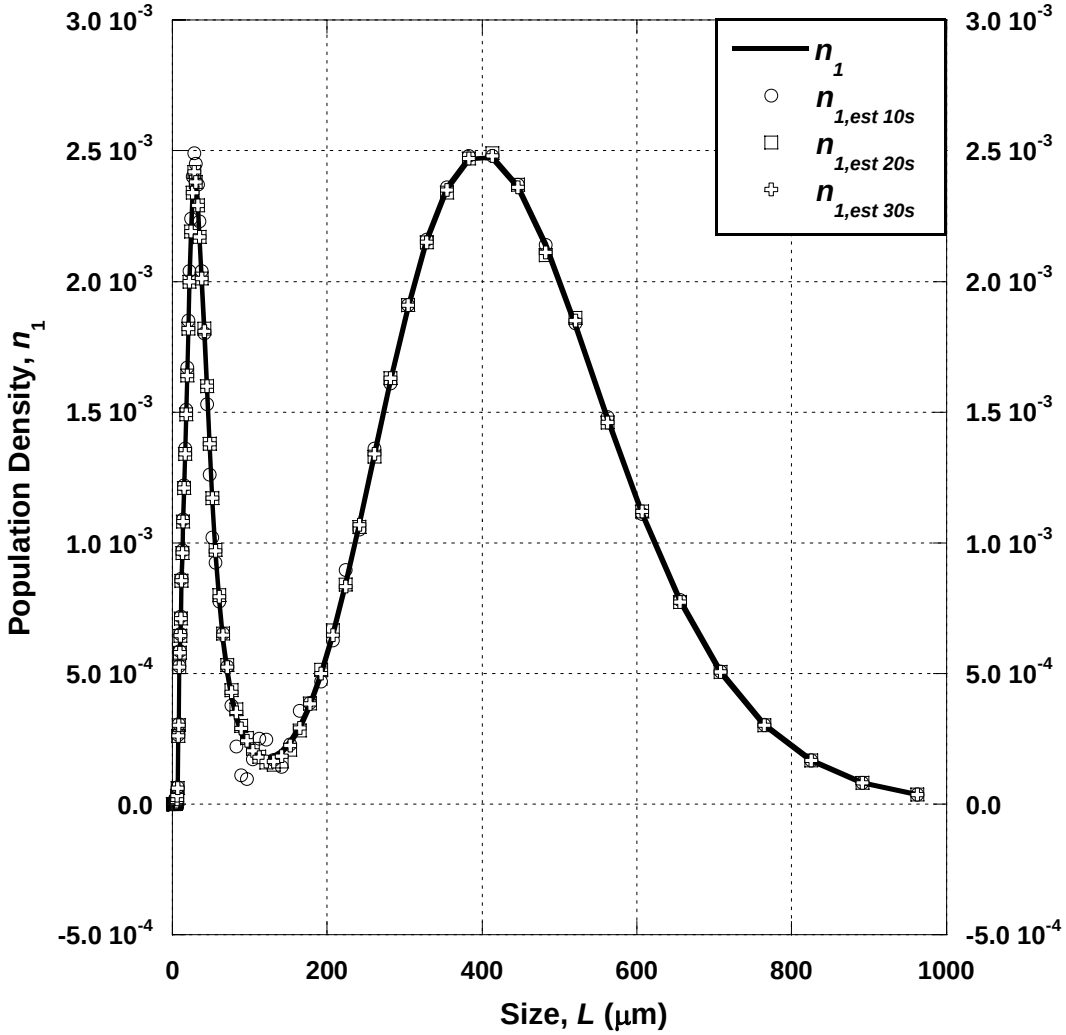

Figure 55. Restoration of the bimodal population density from a noisy chord-length density, using *m′* = 58.

APPENDIX B

MATLAB PROGRAM –SPECTRAL METHOD

```
function [U,D,n1] = basisdecomp (n,mprime)

format long;

%call matrices
load L;
load Moct;

%compute eigenvalues and vectors
m = 90;cutoff=mprime;
TMoct=Moct';
for i = 1:m
     for j = 1:m
        A(i,j) = TMoct (i,:)*Moct (:,j);
     end
end

[U,D]=eig(A);
for i = 1:m
    lambda1(i,1)=D(i,i);
end

%compute actual cld and bth
for i = 1:90
    cld(i,1)=Moct (i,:)*n(:,1);
end

for i = 1:90
    bth(i,1)=TMoct (i,:)*cld(:,1);
end

%calcul coef alpha
for i = 1:m
    for j = 1:m
        eigenvector(j,1)=U(j,i);
    end
    alpha(i,1)=dot(n,eigenvector);
    cldcoef(i,1)=dot(cld,eigenvector);
end

for i = 1:m
    for j = 1:m
        teta1(j,i)=alpha(i,1)*U(j,i);
        coefq(j,i)=cldcoef(i,1)*U(j,i);
    end
end

%compute projection cld
```

```
for i = 1:m
    a=0;
    for j = (cutoff+1):90
        a=a+coefq(i,j);
    end
    qobs (i,1)=a;
    qba=0;
    for j = 1:cutoff
       qba=qba+coefq(i,j);
    end
    qunobs(i,1)=qba;
end

%compute n1
for i = 1:m
    a=0;
    for j = (cutoff+1):90
        a=a+teta1(i,j);
    end
    n1obs(i,1)=a;
end

%compute n1 on the unobservable
for i = 1:m
    a=0;
    for j = 1:cutoff
        a=a+teta1(i,j);
    end
    n1unobs (i,1)=a;
end

%calcul coef beta
for i = 1:90
    beta(i,1)=alpha(i,1)*lambda1(i,1);
end
for i = 1:m
    for j = 1:m
        teta2(j,i)=beta(i,1)*U(j,i);
    end
end

%calcul b=phiq observable vectors
for i = 1:m
    a=0;
    for j = (cutoff+1):90
        a=a+teta2(i,j);
    end
    phiqobs (i,1)=a;
end

% b=phiq on the unobservable
for i = 1:m
    a=0;
    for j = 1:cutoff
        a=a+teta2(i,j);
    end
```

```
    phiqunobs (i,1)=a;
end
cld;
qobs;
qunobs;
lambda1;
n1obs;
n1unobs;

%%%%%%%%%%%%%%%%%%%%%%%%%%%%%%%%%%%%%%%%%%%%%%%%%%
%restauration pop density
%%%%%%%%%%%%%%%%%%%%%%%%%%%%%%%%%%%%%%%%%%%%%%%%%%
%calcul TMoct*q=b
%calcul b
for i = 1:m
        bb(i,1) = TMoct (i,:)*cld(:,1);
end

%compute alpha, ui*b on last 35 vectors
for i = 1:m
    for j = 1:m
        eigenvector(j)=U(j,i);
    end
    beta2(i)=dot(eigenvector,bb);
    alpha2(i)=beta2(i)/lambda1(i);
end
for i = 1:m
    for j = 1:m
        teta2(j,i)=alpha2(i)*U(j,i);
    end
end

%compute n1 on observables vectors
for i = 1:m
    a=0;
    for j = (cutoff+1):m
        a=a+teta2(i,j);
    end
    nrecov(i,1)=a;
end
%compute n1 on unobservable
for i = 1:m
    a=0;
    for j = 1:cutoff
        a=a+teta2(i,j);
    end
    nrecovunobs(i,1)=a;
end

%normalization nrecov
aa=nrecov(1)*(1.08-1);
for i = 2:90
    tot(i)= nrecov(i,1)*(L(i)-L(i-1));
    aa=tot(i)+aa;
end
```

```
for i = 1:90
    nrecov(i,1)=nrecov(i,1)/aa;
end

% check if nrecov give right q + norm
for i = 1:90
    qq(i,1)=Moct (i,:)*nrecov(:,1);
end

%multiply by TMoct to get b
for i = 1:m
        bbq(i,1) = TMoct (i,:)*qq(:,1);
end

nrecov;
qq;
bbq;

%compute error
error=0;
totn=0;
for i = 1:m
        error = error+(n1(i,1)- nrecov(i,1))^2
        totn = totn+(n1(i,1))^2
end
errortotal = sqrt(error/totn);
```

APPENDIX C

MATLAB PROGRAM –F.D. METHOD

```
function [n,C]=popfinitediff(B)
format long

%definition stepsize t sec, L m
deltaL=.1e-6;Lmax=4000;%up to 750um
deltat=10/60;%tmax=5000;

%definition vecteurs
L=zeros(Lmax,1);
for j=1:Lmax
    L(j,1)=0+j*deltaL;
end
lengtht=2701;%tmax=deltat*lengtht;
time=zeros(lengtht,1);
for i=1:lengtht
    time(i,1)=i*deltat;
end

%define temperature
TT=zeros(lengtht,1);
for i=1:250
TT(i,1)=70+273-(0.20)*i*deltat;
end
for i=251:350
    TT(i,1)=273+45;
end
for i=351:lengtht
    TT(i,1)=45+273-(0.20)*i*deltat;
if (Temp>=283)
    TT(i,1)=Temp;
else
    TT(i,1)=283;
end
end

%definition initial and boundary conditions
n=zeros(lengtht,Lmax);C=zeros(lengtht,1);
for j=1:Lmax
    n(1,j)=0;
end
C(1,1)=0.11/151.16/(.11/1293+.263/789);
for i=1:lengtht
CS(i,1)=2.955e-4*exp(2.179e-2*TT(i,1))/151.16/((2.955e-4*exp(2.179e-
2*TT(i,1)))/1293+1/789);
Gamma1(i)=0.414*1.38e-23*TT(i,1)*(1293/0.15116*6.02e23)^(2/3)
*log(1293/0.15116/CS(i,1));
end
CS;
```

```
B(1,1)=3.96e18*exp(-16*3.1416*(Gamma1(1))^3*(0.15116/1293)^2)*
/(3*TT(1,1)^3*(1.38e-23)^3*(log(C(1,1)/CS(1,1)))^2);
G(1,1)= (3.71/3*0.866*1293)*2.68e3* exp(-4.16e4/(8.314*TT(i,1)))*
(C(1,1)-CS(1,1))^2;
n(1,1)=B(1,1)*1e10/G(1,1); deltaC(1,1)=C(1,1)-CS(1,1);
Actot(1,1)=L(1,1)^2*n(1,1)*deltaL;
%compute n
for i=1:lengtht-1
%surface area Actot = sum L^2*n*DL
C(i+1,1)=C(i,1)-deltat*(sqrt(3)*3.14^(2/3)*G(i,1)*Actot(i,1);
B(i+1,1)=3.96e18*exp(-16*3.1416*(Gamma1(i+1))^3*(0.15116/1293)^2)*
/(3*TT(i+1,1)^3*(1.38e-23)^3*(log(C(i+1,1)/CS(i+1,1)))^2);
G(i+1,1)=(3.71/3*0.866*1293)*2.68e3*exp(-4.16e4/(8.314*TT(i+1,1)))
*(C(i+1,1)-CS(i+1,1))^2;
n(i+1,1)=B(i+1,1)/(G(i+1,1)/deltaL);
deltaC(i+1,1)=C(i+1,1)-CS(i+1,1);

    for j=2:Lmax
    n(i+1,j)=n(i,j)-(deltat*G(i,1)*(n(i,j)-n(i,j-1))/deltaL);
    end
end
atot=0;
for j=1:Lmax
atot= atot + L(i+1)^2*n(i+1,j)*deltaL;
end
Actot(i+1,1)=atot;

save pop n;
subplot(3,1,1); plot(G)
subplot(3,1,2); plot(B)
subplot(3,1,3); plot(C)
mesh(n);
```

APPENDIX D

POPULATION BALANCE ADDITIONAL SIMULATION

So as to complete the information presented in Chapter 7, we here use the population balance model to predict the evolution of the run described in Chapter 6. The temperature profile is as shown in Figure 56. The step sizes are the same for the finite difference method, for time Δt = 10 s and for the length step size ΔL = 0.1 μm. We use j_n = 8 for the moment transformation. As was shown in Chapter 7, both the finite difference (F.D.) and the moments transformation are in agreement but are slightly different then the experimental results. The general evolution of the concentration is well predicted.

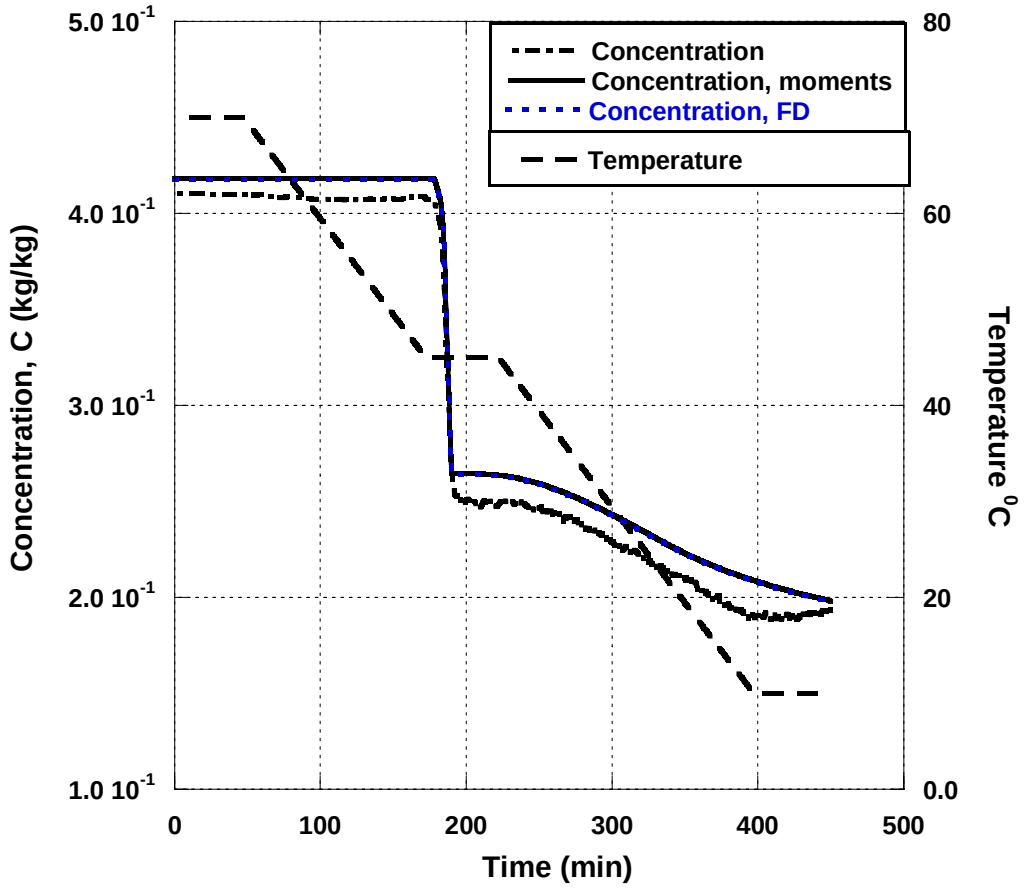

Figure 56. Experimental Concentration vs. simulated one.

The evolution of the population density $\boldsymbol{n}(L,t)$ is shown in Figure 37. We clearly see the nucleation event followed by the growth of the crystals. $\boldsymbol{n}(L,t)$ is here plotted every 20 minutes, it is once again noticed that both methods are in agreement.

In Figure 57, we look at three specific times to compare the simulated and restored population density. t_0 is defined as the nucleation time, three different times were here considered: t_1 = 20 min, t_2 = 100 min and t_3 = 200 min. A parallel evolution in between model and simulation is observed, nonetheless the population density, even though close, do not agree. This is due to the assumptions made while estimating the kinetics and solving the population balance equations.

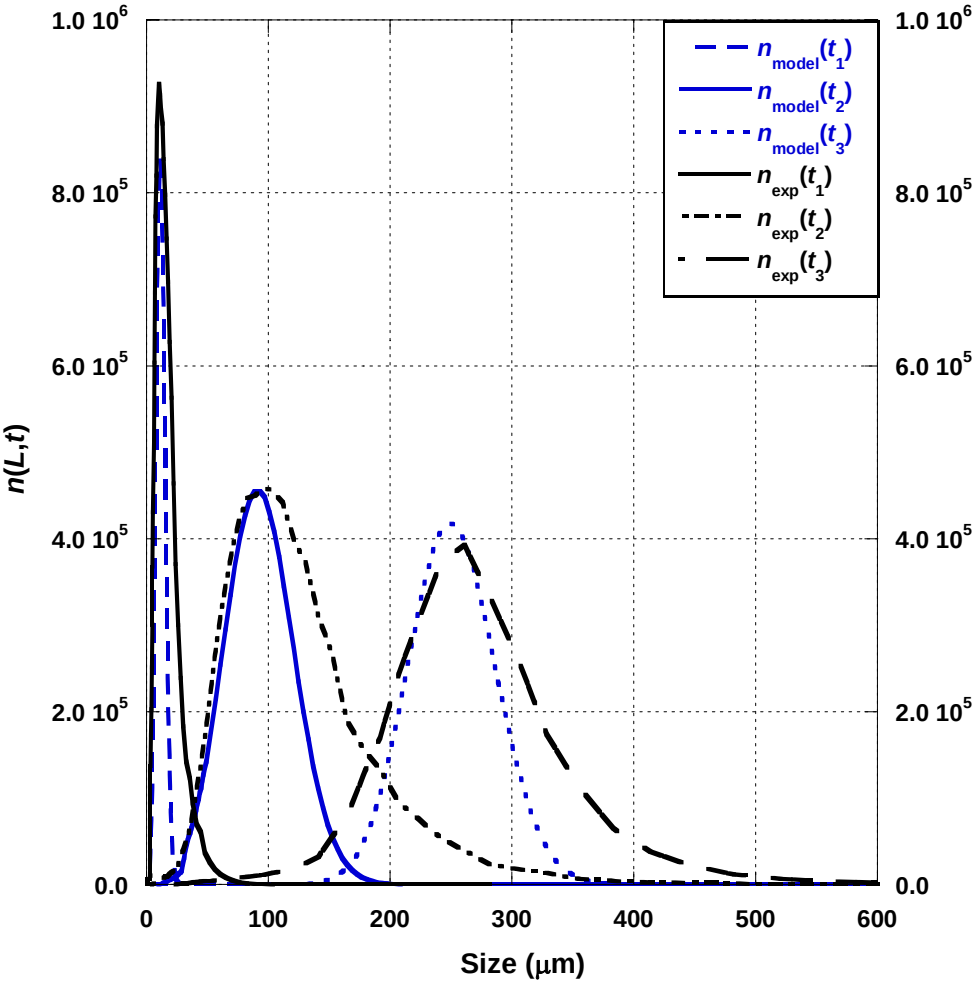

Figure 57. Comparison simulated vs. experimental $n(L,t)$ (t_1= 2 min, t_2=150 min and t_3= 300 min)

As shown in Figure 57, there is growth dispersion experimentally. This is not rendered in the model. The assumptions made to solve the population balance do not take into account the possibility of size dependent growth rate. The growth rate dispersion explains the tail seen in the experimentally obtained population density. The model provides a fairly good estimation of the trend of the evolution of the population density but with still some imprecision in the numbers.

REFERENCES

1. Allen T., Particle size measurement. Powder sampling and particle size measurement, vol 15, Chapman & Hall, London, **1997.**

2. Al-Zoubi N., Kachrismanis K., Malamataris S., "Effects of harvesting and cooling on crystallization and transformation of orthorhombic paracetamol in ethanolic solution", *European J. of Pharma. Sci.,* **2002,** 17, (1-2), 13-21.

3. Al-Zoubi N., Nikolakakis I., Malamataris S., "Crystallization conditions and formation of orthorhombic paracetamol from ethanolic solution", *J. Pharm. Pharmaco*., **2002,** 54, 325-333.

4. Barrett P., Glennon B. and O'Sullivan B., "Solubility curve and metastable zone width using Lasentec FBRM & PVM", Lasentec Users Forum, Charleston, SC, **2002.**

5. Barthe S., Gallivan, M., Rousseau, RW., "Principal Component Analysis for the restoration of population density from measurements of chord-length density", *AIChE J.*, submitted march **2008.**

6. Barthe S.; Rousseau, R.W., "Utilization of FBRM in the control of CSD in a batch cooled crystallizer", *Chem. Eng. Tech.*, **2006**, 29, (2), 206-211.

7. Beers K. Numerical methods for chemical engineering. Cambridge University Press, **2007**.

8. Beyer, T.; Day, G.; Price, S., "The prediction, morphology, and mechanical properties of the polymorphs of paracetamol", *Journal of the American Chemical Society*, **2001**, 123, (21), 5086-5094.

9. Brittain H. G., "Polymorphism in Pharmaceutical Solids", Drugs and the Pharmaceutical Sciences*, V. 95,* New York Marcel Dekker, Inc., **1999**.

10. Brown W., Dynamic Light Scattering: The Method and Some Applications, Oxford University Press, **1993.**

11. Chemburkar, S.R.; Bauer, J.; Deming, K. et al., "Dealing with the impact of ritonavir polymorphs on the late stages of bulk drug process development", *Organic Process Research & Development* **2000,** 4, (5), 413-417.

12. Costa C., Maciel M. and Filho R., "Considerations on the crystallization modeling: Population balance solution", *Computers & Chemical Engineering*, 31, (3), **2007**, 206-218.

13. David L. Ma, Danesh K. Tafti and Richard D. Braatz , "Optimal control and simulation of multidimensional crystallization processes", *Computers & Chemical Engineering*, **2002,** 26, (7-8), 1103-1116.

14. DiMartino, P.; Guyot-Hermann, A.M.; Conflant, P.; Drache, M.; Guyot, J.C., "A new pure paracetamol for direct compression: The orthorhombic form", *Journal of the American Chemical Society*, **1996**, 128, (1-2), 1-8.

15. Fachaux, J.M.; Guyot-Hermann, A.M.; Guyot, J.C.; Conflant, P.; Drache, M.; Veesler, S.; Boistelle R., "Pure paracetamol for direct compression - Part I. Development of sintered-like crystals of paracetamol", *Powder technology*, **1995**, 82, 123-128.

16. Fachaux, J.M.; Guyot-Hermann, A.M.; Guyot, J.C.; Conflant, P.; Drache, M.; Veesler, S.; Boistelle R., "Pure paracetamol for direct compression - Part II. Study of the physicochemical and mechanical properties of sintered-like crystals of paracetamol", *Powder technology*, **1995**, 82, 129-133.

17. Finnie S, Ristic RI, Sherwood JN, et al., "Characterization of growth behaviour of small paracetamol crystals growth from pure solution", *Chem. Eng. Research & Design*, **1996**, 74, (A7), 835-838.

18. Finnie SD, Ristic RI, Sherwood JN, et al., "Morphological and growth rate distributions of small self-nucleated paracetamol crystals grown from pure aqueous solutions", *J. of Crystal Growth*, **1999**, 207, (4), 308-318.

19. Gracin, S. and Åke C. Rasmuson, "Solubility of Phenylacetic Acid, *p*-Hydroxyphenylacetic Acid, *p*-Aminophenylacetic Acid, *p*-Hydroxybenzoic Acid, and Ibuprofen in Pure Solvents", *J. Chem. Eng. Data*, **2002**, 47, 1379-1383.

20. Granberg R., Bloch D., Rasmuson, Å., "Crystallization of paracetamol in acetone - water mixtures", *J. of Crystal Growth*, **1999,** 198/199, 1287-1293.

21. Granberg R., Ducreux C., Gracin S., Rasmuson A., "Primary nucleation of paracetamol in acetone-water mixtures", *Chem. Eng. Sci.*, **2001**, 56, 2305-2313.

22. Granberg R.., Rasmuson Å., "Crystal growth rates of paracetamol in mixtures of water + acetone + toluene", *AIChE Journal*, **2005**, 51, (9), 2441-2456.

23. Greenberg, E. F., "FDA wants more 'current' good manufacturing practices.", *Packaging Digest*, **2002,** 39, (10), 28-29.

24. Guillori J., "Generation of polymorphs hydrates, solvates, and amorphous solids", In *Polymorphism in Pharmaceutical Solids*, Brittain H.G. ed. Marcel Drekker Inc, NY, **1999.**

25. Gunawan R, Fusman I, Braatz RD "High resolution algorithms for multidimensional population balance equations", *AIChE Journal*, **2004**, 50, (11), 2738-2749.

26. Hulburt H.M., Katz S., "Some problems in particle technology", *Chem. Eng. Sci.* , **1964**, 19, 555-574.

27. Kashchiev D, van Rosmalen GM "Review: Nucleation in solutions revisited", *Crystal Research & Technology*, **2003**, 38, (7-8), 555-574.

28. Kaye B.H., Alliet D., Switer L., Turbitt-Daout C., "The effect of shape on intermethod correlation of techniques for characterizing the size distribution of powder. Part1: correlating the size distribution as measured by sieving, image analysis and diffractometer methods", *Part. part. syst. Charact*., **1997,** 14, (5), 219-224.

29. Kaye B.H., Alliet D., Switer L., Turbitt-Daout C., "The effect of shape on intermethod correlation of techniques for characterizing the size distribution of powder. Part2: correlating the size distribution as measured by diffractometer methods, TSI-Amherst aerosol spectromer and coulter counter", *Part. part. syst. Charact.,* **1999,** 16, (6), 266-272.

30. Kumar S, Ramkrishna D "On the solution of population balance equations by discretization - III. Nucleation, growth and aggregation of particles", *Chem. Eng. Sci.*, 52, (24), 4659-4679, 1997.

31. Kumar S, Ramkrishna D, "On the solution of population balance equations by discretization .1. A fixed pivot technique", *Chem. Eng. Sci.*, **1996**, 51, (8), 1311-1332.

32. Lachman, L. Lieberman, H. A. and Kanig, J. L., Theory and Practice of Industrial Pharmacy, 3rd Edition Lea & Febiger., Philadelphia, **1986.**

33. Lasentec website www.mt.com/lasentec (last accessed May 2008)

34. Li M, Wilkinson D, Patchigolla K. "Determination of non-spherical particle size distribution from chord length measurements. Part II: Experimental validation", *Chem. Eng. Sci.,***2005**; 60:4992-5003.

35. Li M, Wilkinson D. "Determination of non-spherical particle size distribution from chord length measurements. Part I: Theoretical analysis", *Chem. Eng. Sci.,* **2005**; 60:3251-3265.

36. Lim Y.I.; Le Lann J.-M.; Meyer X.M.; Joulia X.; Lee G.; Yoon E.S., "On the solution of population balance equations (PBE) with accurate front tracking methods in practical crystallization processes" , *Chemical Engineering Science*, 57, (17), **2002** , 3715-3732.

37. Liu, Y., Wang, J., Wei, H., "Determination of crystallization kinetics in solution", *J. of Crystal Growth*, **2004**, 271, 238-244.

38. Lyons R., *Understanding Digital Signal Processing*, 2nd Ed., Prentice Hall PTR, **2004.**

39. Mahoney AW, Ramkrishna D "Efficient solution of population balance equations with discontinuities by finite elements" *Chem. Eng. Sci.,* **2000**, 57, (7), 1107-1119.

40. Malkin A.J., McPherson A., " Light-scattering investigations of nucleation processes and kinetics of crystallization in macromolecular systems", *Acta Crystallographica Section D -Biological Crystallography*, **1994**, 50, (4), 385-395.

41. Margenau, H. and Murphy, G. M. *The Mathematics of Physics and Chemistry, 2 vols.* Princeton, NJ: Van Nostrand, **1956-64**.

42. Mendez del Rio J., Rousseau R.W., "Batch and tubular batch crystallization of Paracetamol: crystal size distribution and polymorph formation", *Crystal Growth & Design*, **2006,** 6, (6), 1407-1414.

43. Mersmann A., "Calculation of Interfacial Tensions", *J. of Crystal Growth*, **1990**, 102, (4), 841-847.

44. Morris K., " Structural aspects of hydrates and solvates", Polymorphism in Pharmaceutical Solids, Brittain H.G. ed. Marcel Drekker Inc, NY, **1999.**

45. Moynihan H., O'Hare I., "Spectroscopic characterization of the monoclinic and orthorhombic forms of paracetamol", *International Journal of Pharmaceutics*, **2002**, 247, 179-185.

46. Mullin, J.W., "Crystallization", 4th ed., Butterworth-Heinemann: Oxford; Boston **2001.**

47. Mydlarz J., Briedis D., "Growth rate dispersion vs size-dependent growth rate for MSMPR crystallizer data", *Computers & Chemical Engineering*, **1992**, 16, (9), 917-922.

48. Nagy Z., Fujiwara M., Woo X., Braatz R., " Determination of the kinetic parameters for the crystallization of paracetamol from water using metastable zone width experiments", *Ind. Eng. Chem. Res.*, **2008**, 47, 1245-1252.

49. Nichols, G.; Frampton, C.S., "Physicochemical characterization of the orthorhombic polymorph of paracetamol crystallized from solution", *Journal of Pharmaceutical Science*, **1998**, 87, (6), 684-693.

50. O'Sullivan B. & Glennon B., "Application of in Situ FBRM and ATR-FTIR to the Monitoring of the Polymorphic Transformation of D-Mannitol", *Organic Process Research & Development*, **2005**, 9, 884-889.

51. O'Sullivan, B.; Barrett, P.; Hsiao, G.; Carr, A.; Glennon, B., "In Situ Monitoring of Polymorphic Transitions", *Organic Process Research & Development*, **2003**, 7, 977-982.

52. Pons M.N., Vivier H., "Crystal characterization by quantitative image analysis", *Powder technology*, **1990**, 87, (284), 88-95.

53. Qamar S, Ashfaq A, Angelov I, et al., "Numerical solutions of population balance models in preferential crystallization", *Chem. Eng. Sci.* , **2008**, 63, (5), 1342-1352.

54. Qamar S, Ashfaq A, Warnecke G, et al., "Adaptive high-resolution schemes for multidimensional population balances in crystallization processes", *Computers & Chemical Engineering*, **2007**, 31, (10), 1296-1311.

55. Qamar S, Warnecke G, "Numerical solution of population balance equations for nucleation, growth and aggregation processes", *Computers & Chemical Engineering*, **2007**, 31, (12), 1576-1589.

56. Randolph A.D., Larson M.A., "Theory of particulate processes", Academic Press, NY, **1971.**

57. Reutzel - Edens, S., "Achieving polymorph selectivity in the crystallization of pharmaceutical solids: Basic considerations and recent advances ", *Current Opinion in Drug Discovery & Development*, **2006**, 9, (6), 806-815.

58. Rodriguez-Hornedo, N., Murphy, D., "Significance of controlling crystallization mechanisms and kinetics in pharmaceutical systems", *J. Pharm. Sci.*, **1999**, 88, (7), 651-660.

59. Ruf A, Worlitschek J., Mazzotti M., "Modeling and experimental analysis of PSD measurement through FBRM", *Particle & Particle Syst. Charac.*, **2000**,17, (4), 167-179.

60. Russ J.C., "Computer-Assisted Microscopy: The Measurement and Analysis of Images", Plenum Press, **1990.**

61. Schöll, J.; Bonalumi, D.; Vicum, L.; Mazzotti, M., "In Situ Monitoring and Modeling of the Solvent-Mediated Polymorphic Transformation of L-Glutamic Acid", *Crystal Growth & Design*, **2006**, 6, (4), 881-891.

62. Schrof W., Kingler J., Rozouvan S., Horn D., "Raman correlation spectroscopy: a method for studying chemical composition and dynamics of disperse systems", *Phys. Rev. E57*, **1998**, R2523-R2526.

63. Shekunov B., Grant D., "In situ optical interferometric studies of the growth and dissolution behavior of paracetamol 1. Growth kinetics", *J. Phys. Chem*., **1997,** 101, (20), 3973-3979.

64. Shekunov B.Y., Chattopadhyay P., Tong H., Chow A., "Particle size analysis in Pharmaceutics: principles, methods and applications", *Pharm. Res.*, **2007,** 24, (2), 203-227.

65. Shekunov B.Y., York P., "Crystallization processes in pharmaceutical technology and drug delivery design", *J. of Crystal Growth*, **2000**, 211, 122-136.

66. Shekunov BY, Aulton ME, Adama-Acquah RW, and Grant, D., "Effect of temperature on crystal growth and crystal properties of paracetamol", *J. Chem. Soc., Faraday Trans.*, **1996**, 92, (3), 439-444 .

67. Shi D, El-Farra NH, Li MH, Mhaskar P, Christofides PD, Predictive control of particle size distribution in particulate processes, *Chem. Eng. Sci.,* **2006**, 61, (1), 268-281.

68. Sun C., Grant D., "Influence of crystal structure on the tableting properties of sulfamerazine polymorphs", *Pharmaceutical Research*, **2001,** 18, (3), 274-280.

69. Togkalidou T., Fujiwara M., Patel S., and Braatz R.D., "Solute concentration prediction using chemometrics and ATR-FTIR spectroscopy", *J. of Crystal Growth*, **2001**, 231, (4), 534-543 .

70. Van Antwerpen F., Van Krevelen D. W., "Light-scattering method for investigation of the kinetics of crystallization of spherulites", *J. of Polymer Sci.: Polymer Physics Edition*, **1993**, 10, (12), 2409 – 2421.

71. Vanderhallen, F.; Deriemaeker, L.; Manderick, B.; Finsy, R., "Shape and size determination by laser diffraction: parametric density estimation by neural networks", *part. part. Syst. charact.,* **2002**, 19, 65-72 .

72. Wood-Kaczmar K., "The use of FBRM in mixed suspension mixed product removal (MSMPR) continuous crystallization for the on-line measurement of growth kinetics", Lasentec Users Forum, Charleston, SC, **2002.**

73. Worlitschek J., Hocker T., Mazzotti M., "Restoration of PSD from chord length distribution data using the method of projections onto convex sets", *Part. Part. Syst. Charact*., **2005,** 22, 81-98.

74. Worlitschek J., Mazzotti M., "Model-based optimization of particle size distribution in batch cooling crystallization of paracetamol", *Crystal Growth & Design*, **2004**, 4, (5), 891-903.

75. Wynn, E. J. W., "Relationship between particle-size and chord-length distributions in focused beam reflectance measurement: stability of direct inversion and weighting", *Powder Technology*, **2003**, 133, (1-3), 125-133.

76. Young Il Lim, Jean-Marc Le Lann, Xuan Mi Meyer, Xavier Joulia, Gibaek Lee and En Sup Yoon , "On the solution of population balance equations (PBE) with accurate front tracking methods in practical crystallization processes", *Chem. Eng. Sci.*, **2002,** 57, (17), 3715-3732.

77. Yu L., Lionberger R., Raw A., D'Costa R., Wu H., Hussain A., "applications of process analytical technology to crystallization processes", *Ad. Drug Deliv. Rev.,* **2004,** 56, 349-369.